

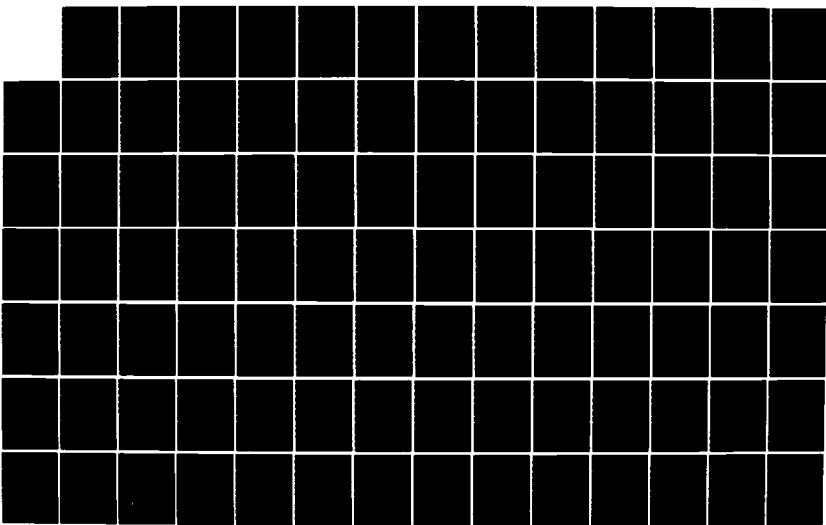
AD-A154 326 SOIL-AIR INTERACTIONS DURING AIRBLAST-INDUCED GROUND
MOTIONS(U) CALIFORNIA RESEARCH AND TECHNOLOGY INC
CHATSWORTH M ROSENBLATT ET AL. 01 JAN 82 CRT-3470F

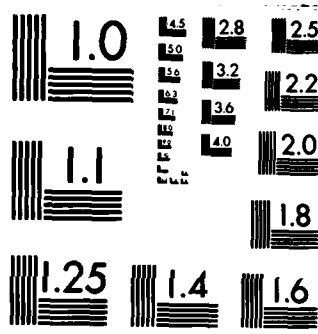
UNCLASSIFIED DNA-TR-81-103 DNA001-81-C-0247

F/G 8/7

1/2

NL





MICROCOPY RESOLUTION TEST CHART
NATIONAL BUREAU OF STANDARDS-1963-A

AD-A 154 326

100-1683
②

DNA-TR-81-103

SOIL-AIR INTERACTIONS DURING AIRBLAST-INDUCED GROUND MOTIONS

Martin Rosenblatt
Paul J. Hassig
Dennis L. Orphal
California Research & Technology, Inc.
20943 Devonshire Street
Chatsworth, CA 91311-2376

1 January 1982

Technical Report

CONTRACT No. DNA 001-81-C-0247

APPROVED FOR PUBLIC RELEASE;
DISTRIBUTION UNLIMITED.

THIS WORK WAS SPONSORED BY THE DEFENSE NUCLEAR AGENCY
UNDER RDT&E RMSS CODE B344081466 Y99QAXSG00006 H2590D.

Prepared for

Director

DEFENSE NUCLEAR AGENCY

Washington, DC 20305

DTIC
ELECTE
MAY 31 1985
S D
B

DTIC FILE COPY

85 03 29 009

Destroy this report when it is no longer
needed. Do not return to sender.

PLEASE NOTIFY THE DEFENSE NUCLEAR AGENCY,
ATTN: STTI, WASHINGTON, D.C. 20305, IF
YOUR ADDRESS IS INCORRECT, IF YOU WISH TO
BE DELETED FROM THE DISTRIBUTION LIST, OR
IF THE ADDRESSEE IS NO LONGER EMPLOYED BY
YOUR ORGANIZATION.



UNCLASSIFIED
SECURITY CLASSIFICATION OF THIS PAGE

REPORT DOCUMENTATION PAGE

| | | | |
|--|--|--|---|
| 1a REPORT SECURITY CLASSIFICATION UNCLASSIFIED | | 1b. RESTRICTIVE MARKINGS | |
| 2a SECURITY CLASSIFICATION AUTHORITY N/A | | 3. DISTRIBUTION/AVAILABILITY OF REPORT Approved for public release; distribution is unlimited. | |
| 2b DECLASSIFICATION/DOWNGRADING SCHEDULE N/A since UNCLASSIFIED | | | |
| 4. PERFORMING ORGANIZATION REPORT NUMBER(S) CRT3470F | | 5. MONITORING ORGANIZATION REPORT NUMBER(S) DNA-TR-81-103 | |
| 6a NAME OF PERFORMING ORGANIZATION California Research & Technology, Inc. | 6b OFFICE SYMBOL (If applicable) | 7a. NAME OF MONITORING ORGANIZATION Director, Defense Nuclear Agency | |
| 6c ADDRESS (City, State, and ZIP Code) 20943 Devonshire Street Chatsworth, California 91311-2376 | | 7b. ADDRESS (City, State, and ZIP Code) Washington, DC 20305 | |
| 8a. NAME OF FUNDING/SPONSORING ORGANIZATION | 8b OFFICE SYMBOL (If applicable) | 9. PROCUREMENT INSTRUMENT IDENTIFICATION NUMBER DNA 001-81-C-0247 | |
| 9c. ADDRESS (City, State, and ZIP Code) | | 10. SOURCE OF FUNDING NUMBERS | |
| | | PROGRAM ELEMENT NO 62715H | PROJECT NO Y99QAXS |
| | | TASK NO G | WORK UNIT ACCESSION NO DH000006 |
| 11. TITLE (Include Security Classification) SOIL-AIR INTERACTIONS DURING AIRBLAST-INDUCED GROUND MOTIONS | | | |
| 12. PERSONAL AUTHOR(S) Martin Rosenblatt Paul Joseph Hassig | | Dennis Lee Orphal | |
| 13a. TYPE OF REPORT Technical Report | 13b. TIME COVERED FROM 81 Jul TO 82 Jan | 14. DATE OF REPORT (Year, Month, Day) 1982, January 1 | 15. PAGE COUNT 160 |
| 16. SUPPLEMENTARY NOTATION This work sponsored by the Defense Nuclear Agency under RDT&E RMSS Code B344081466 Y99QAXSG00006 H2590D. | | | |
| 17. COSATI CODES | | 18. SUBJECT TERMS (Continue on reverse if necessary and identify by block number) Ground Motion Multiphase Flow MISERS BLUFF Airblast Two-Phase Flow Pore-Air Fluidization | |
| 19. ABSTRACT (Continue on reverse if necessary and identify by block number) <p>Some ground motion records in HE field tests, e.g., MISERS BLUFF II-2 and PRE-MINE THROW IV-6, exhibit an enhanced upward velocity immediately following the initial airblast-induced downward motion. Also, laboratory experiments show the development of upward soil motions during positive air overpressure loadings; the motion in the laboratory tests was shown to be related to the flow of the air through the soil pores.</p> <p>In this report, the effects of pore-air* on ground motions in dry porous soils are analyzed using five numerical simulations in one space dimension and time. Also,</p> | | | |
| 20. DISTRIBUTION/AVAILABILITY OF ABSTRACT <input type="checkbox"/> UNCLASSIFIED/UNLIMITED <input checked="" type="checkbox"/> SAME AS RPT. <input type="checkbox"/> DTIC USERS | | 21. ABSTRACT SECURITY CLASSIFICATION Unclassified | |
| 22a. NAME OF RESPONSIBLE INDIVIDUAL Betty L. Fox | | 22b. TELEPHONE (Include Area Code) 202-325-7042 | 22c. OFFICE SYMBOL DNA/STTI |

UNCLASSIFIED

SECURITY CLASSIFICATION OF THIS PAGE

19. ABSTRACT (Continued)

experimentally observed ground motions involving enhanced vertical velocities are explained using two-phase (soil and air) physics, including (a) the flow of air through the soil pores, and (b) soil fluidization. Fluidization of the soil occurs when the soil particles lose contact with each other and the total pressure is entirely supported by the pore-air.

The primary conclusions are:

1. Large sustained upward velocities can develop in near-surface soils subjected to airblast loading due to soil fluidization caused by pore-air phenomena.
2. In the laboratory experiments involving relatively high soil permeabilities, the 100 psi peak overpressure airblast caused air to flow through the soil pores, thereby increasing pore-air pressures which resulted in soil fluidization during the positive overpressure phase. Peak pore-air flow speeds of ~15 m/s are predicted, and the soil "fluidization front" propagates at ~4 m/s (Case 1).
3. In the MISERS BLUFF II-2 field experiment involving low soil permeabilities and almost no pore-air flow, soil fluidization and sustained upward velocities occurred during the negative overpressure phase as the pore-air in the soil expanded to reach pressure equilibrium with the low airblast pressure.
4. The DICE code numerical simulations (Cases 1 to 5) reproduced the phenomenology observed in the laboratory and field experiments. The relatively simple models used for soil permeability and internal interaction forces (drag) were adequate for quantitatively reproducing the experimental data; however, the in-situ soil permeability is a sensitive physical parameter and careful measurements and model calibrations will be necessary before quantitative predictions and associated uncertainties of ground motions can be made concerning strategic/tactical sites of interest.

UNCLASSIFIED

SECURITY CLASSIFICATION OF THIS PAGE

PREFACE

Dr. George Ullrich (DNA/SPSS) was the technical monitor for this work and his helpful suggestions are gratefully acknowledged.

| | |
|--------------------|---------|
| Accession For | |
| NAME | Level |
| DATA | DATE |
| Characterized | |
| JULY 1981 | |
| SAC | |
| INSTITUTION/ | |
| AVAILABILITY CODES | |
| Avail and/or | |
| DATA | Special |
| A-1 | |



CONVERSION FACTORS

| Physical Quantity | To convert from units in report | To metric (SI) units | Multiply by |
|-------------------|---------------------------------|---|---|
| Mass | pound ton kton | kilogram (kg) kilogram (kg) kilogram (kg) | .454 10^3 10^6 |
| Energy | ton kton Mton | joules (J) joules (J) joules (J) | 4.2×10^9 4.2×10^{12} 4.2×10^{15} |
| Pressure | bar* psi* | pascal (Pa) pascal (Pa) | 10^5 6895. |
| Density | gm/cm | kg/m | 10^3 |
| Length | foot | meter (m) | .3048 |

*1 bar = 14.5 psi
 1 psi = .06895 bar

TABLE OF CONTENTS

| <u>Section</u> | <u>Page</u> |
|---|-------------|
| PREFACE. | 1 |
| CONVERSION FACTORS | 2 |
| LIST OF ILLUSTRATIONS. | 4 |
| 1 INTRODUCTION AND SUMMARY | 13 |
| 1.1 BACKGROUND. | 13 |
| 1.2 OBJECTIVES AND APPROACH | 14 |
| 1.3 SUMMARY OF RESULTS. | 17 |
| 1.4 CONCLUSIONS AND RECOMMENDATIONS | 26 |
| 2 MULTIPHASE THEORY. | 29 |
| 2.1 GOVERNING PHYSICAL EQUATIONS - GENERAL FORMULATION | 29 |
| 2.2 STRESS PARTITIONING IN A SOIL-AIR MEDIA | 35 |
| 2.3 INTERNAL INTERACTION (OR DRAG) FORCE. | 37 |
| 2.4 TWO-PHASE FLOW TEST CASE. | 41 |
| 2.5 AIR ONLY TEST CASE FOR WEAK SHOCK ($\Delta P = 0.1$ bar). | 48 |
| 3 PORE-AIR PHENOMENA IN A SHOCK TUBE | 55 |
| 3.1 LABORATORY EXPERIMENTS. | 55 |
| 3.2 NUMERICAL SIMULATIONS | 62 |
| 3.2.1 Case 1 ($D_p^p = 0.1$ cm, $g = 980$ cm/s ²). | 66 |
| 3.2.2 Case 2 ($D_p^p = 0.05$ cm, $g = 980$ cm/s ²) | 79 |
| 3.2.3 Case 3 ($D_p^p = 0.05$ cm, $g = 0$) | 89 |
| 3.2.4 Case 4 ($D_p^p = 0.142$ cm, $g = 0$). | 100 |
| 3.3 COMPARISON OF NUMERICAL SIMULATIONS WITH EXPERIMENTS | 111 |
| 4 MISERS BLUFF II-2. | 128 |
| 4.1 EXPERIMENTAL RESULTS. | 128 |
| 4.2 NUMERICAL SIMULATION. | 133 |
| REFERENCES | 151 |

LIST OF ILLUSTRATIONS

| <u>Figure</u> | | <u>Page</u> |
|---------------|--|-------------|
| 1.1 | Main Surface Displacement Versus Time Observed in Experiments (Zernow <i>et al.</i> , 1973) and Calculated by DICE (Cases 1 and 2) | 18 |
| 1.2 | Pressure and Velocity Profiles Versus Depth at $t = .200$ Seconds for Cases 1 and 2 | 21 |
| 1.3 | (a) Pore-Air Overpressure and (b) Soil Velocity Versus Time at Various Station Depths for Case 1 ($D_p = 0.1$ cm) | 22 |
| 1.4 | (a) Time of Fluidization Versus Depth for Cases 1 to 4 and (b) Comparison of Calculated (Cases 1 to 4) and Observed (Zernow <i>et al.</i> , 1973) Time of Arrival of Peak Overpressure at Various Depths | 24 |
| 1.5 | (a) Vertical Velocity and (b) Vertical Displacement Time History Comparisons, Case 5 Versus MISERS BLUFF II-2 Experimental Data at 25 m Radius and 0.5 m Initial Depth | 27 |
| 2.1 | Normalized Permeability (k/R^2) Versus Porosity from the Carman and Brinkman Equations | 42 |
| 2.2 | Overpressure Versus Distance Profiles at $t = .096, .166$ and $.208$ Seconds for Shock Tube Test Case | 45 |
| 2.3 | Overpressure Versus Distance Profiles at $t = .279, .321, .391$ and $.448$ Seconds for Shock Tube Test Case | 46 |
| 2.4 | Shock Wave Speed Versus Time for Shock Tube Test Case | 47 |
| 2.5 | Theoretical Positions of Shock Front, Contact Discontinuity and Rarefaction Fan Versus Time for Low Overpressure Test Case | 49 |
| 2.6 | Air Overpressure Versus Position at $t = .030$ Seconds for Low Overpressure Test Case . . . | 51 |

LIST OF ILLUSTRATIONS (continued)

| <u>Figure</u> | | <u>Page</u> |
|---------------|--|-------------|
| 2.7 | Air Particle Velocity Versus Position at $t = .030$ Seconds for Low Overpressure Test Case. | 52 |
| 2.8 | Air Temperature Versus Position at $t = .030$ Seconds for Low Overpressure Test Case. | 53 |
| 2.9 | Air Density Versus Position at $t = .030$ Seconds for Low Overpressure Test Case | 54 |
| 3.1 | (a) Conceptual Design of a Shock Tube Utilizing Gas Flow Through an Orifice to Control Pressure-Time History on the Sand Surface, and (b) Schematic View of 8-Inch Vertical Shock Tube | 56 |
| 3.2 | Overpressure Load to Surface of Sand Column Versus Time Observed in Experiments (Zernow <i>et al.</i> , 1973) and Fit Exponentially (used in DICE Cases 1 to 4 Calculations). | 57 |
| 3.3 | Average Distribution (% By Weight) of Standard Sand Used in 8" Diameter Shock Tube Experiments (Zernow <i>et al.</i> , 1973). | 59 |
| 3.4 | Main Surface Displacement Versus Time for 8" Diameter Shock Tube Experiments (Zernow <i>et al.</i> , 1973). | 61 |
| 3.5 | Position of Near-Surface Marked Sand Layers Versus Time Observed in Shock Tube Experiments (Zernow <i>et al.</i> , 1973). | 63 |
| 3.6 | Pressure Loading and Soil Parameters for 1-D Shock Tube Calculations (Cases 1 to 4) | 65 |
| 3.7 | Grid Used for DICE 1-D Shock Tube Calculations, Cases 1 to 4 | 67 |
| 3.8 | Initial Soil, Air and Total Stress Versus Depth for Case 1 ($D_p = 0.1$ cm) | 68 |
| 3.9 | (a) Soil, Air and Total Stress Versus Depth, and (b) Soil and Air Velocity Versus Depth at $t = .001$ Seconds for Case 1 ($D_p = 0.1$ cm). | 69 |

LIST OF ILLUSTRATIONS (continued)

| <u>Figure</u> | | <u>Page</u> |
|---------------|---|-------------|
| 3.10 | (a) Soil, Air and Total Stress Versus Depth, and (b) Soil and Air Velocity Versus Depth at $t = .050$ Seconds for Case 1 ($D_p = 0.1$ cm). | 71 |
| 3.11 | (a) Soil, Air and Total Stress Versus Depth, and (b) Soil and Air Velocity Versus Depth at $t = .100$ Seconds for Case 1 ($D_p = 0.1$ cm). | 73 |
| 3.12 | (a) Soil, Air and Total Stress Versus Depth, and (b) Soil and Air Velocity Versus Depth at $t = .200$ Seconds for Case 1 ($D_p = 0.1$ cm). | 74 |
| 3.13 | (a) Soil, Air and Total Stress Versus Depth, and (b) Soil and Air Velocity Versus Depth at $t = .400$ Seconds for Case 1 ($D_p = 0.1$ cm). | 76 |
| 3.14 | (a) Soil, Air and Total Stress Versus Depth, and (b) Soil and Air Velocity Versus Depth at $t = .600$ Seconds for Case 1 ($D_p = 0.1$ cm). | 77 |
| 3.15 | Soil Density Versus Depth at Various Times for Case 1 ($D_p = 0.1$ cm) | 78 |
| 3.16 | Air Overpressure Versus Time at Various Station Depths for Case 1 ($D_p = 0.1$ cm) | 80 |
| 3.17 | Soil Velocity Versus Time at Various Station Depths for Case 1 ($D_p = 0.1$ cm) | 81 |
| 3.18 | (a) Soil, Air and Total Stress Versus Depth, and (b) Soil and Air Velocity Versus Depth at $t = .001$ Seconds for Case 2 ($D_p = 0.05$ cm) | 83 |
| 3.19 | (a) Soil, Air and Total Stress Versus Depth, and (b) Soil and Air Velocity Versus Depth at $t = .050$ Seconds for Case 2 ($D_p = 0.05$ cm) | 84 |
| 3.20 | (a) Soil, Air and Total Stress Versus Depth, and (b) Soil and Air Velocity Versus Depth at $t = .100$ Seconds for Case 2 ($D_p = 0.05$ cm) | 85 |

LIST OF ILLUSTRATIONS (continued)

| <u>Figure</u> | | <u>Page</u> |
|---------------|---|-------------|
| 3.21 | (a) Soil, Air and Total Stress Versus Depth, and (b) Soil and Air Velocity Versus Depth at $t = .200$ Seconds for Case 2 ($D_p = 0.05$ cm) . . . | 86 |
| 3.22 | (a) Soil, Air and Total Stress Versus Depth, and (b) Soil and Air Velocity Versus Depth at $t = .400$ Seconds for Case 2 ($D_p = 0.05$ cm) . . . | 87 |
| 3.23 | (a) Soil, Air and Total Stress Versus Depth, and (b) Soil and Air Velocity Versus Depth at $t = .600$ Seconds for Case 2 ($D_p = 0.05$ cm) . . . | 88 |
| 3.24 | Air Overpressure Versus Time at Various Station Depths for Case 2 ($D_p = 0.05$ cm) | 90 |
| 3.25 | Soil Velocity Versus Time at Various Station Depths for Case 2 ($D_p = 0.05$ cm) | 91 |
| 3.26 | (a) Soil, Air and Total Stress Versus Depth, and (b) Soil and Air Velocity Versus Depth at $t = .001$ Seconds for Case 3 ($D_p = 0.05$ cm) . . . | 92 |
| 3.27 | (a) Soil, Air and Total Stress Versus Depth, and (b) Soil and Air Velocity Versus Depth at $t = .050$ Seconds for Case 3 ($D_p = 0.05$ cm) . . . | 93 |
| 3.28 | (a) Soil, Air and Total Stress Versus Depth, and (b) Soil and Air Velocity Versus Depth at $t = .100$ Seconds for Case 3 ($D_p = 0.05$ cm) . . . | 94 |
| 3.29 | (a) Soil, Air and Total Stress Versus Depth, and (b) Soil and Air Velocity Versus Depth at $t = .200$ Seconds for Case 3 ($D_p = 0.05$ cm) . . . | 95 |
| 3.30 | (a) Soil, Air and Total Stress Versus Depth, and (b) Soil and Air Velocity Versus Depth at $t = .400$ Seconds for Case 3 ($D_p = 0.05$ cm) . . . | 96 |
| 3.31 | (a) Soil, Air and Total Stress Versus Depth, and (b) Soil and Air Velocity Versus Depth at $t = .600$ Seconds for Case 3 ($D_p = 0.05$ cm) . . . | 97 |

LIST OF ILLUSTRATIONS (continued)

| <u>Figure</u> | | <u>Page</u> |
|---------------|---|-------------|
| 3.32 | Air Overpressure Versus Time at Various Station Depths for Case 3 ($D_p = 0.05$ cm) | 99 |
| 3.33 | Soil Velocity Versus Time at Various Station Depths for Case 3 ($D_p = 0.05$ cm) | 101 |
| 3.34 | (a) Soil, Air and Total Stress Versus Depth, and (b) Soil and Air Velocity Versus Depth at $t = .001$ Seconds for Case 4 ($D_p = 0.142$ cm). . . | 102 |
| 3.35 | (a) Soil, Air and Total Stress Versus Depth, and (b) Soil and Air Velocity Versus Depth at $t = .050$ Seconds for Case 4 ($D_p = 0.142$ cm) . . | 103 |
| 3.36 | (a) Soil, Air and Total Stress Versus Depth, and (b) Soil and Air Velocity Versus Depth at $t = .100$ Seconds for Case 4 ($D_p = 0.142$ cm). . . | 104 |
| 3.37 | (a) Soil, Air and Total Stress Versus Depth, and (b) Soil and Air Velocity Versus Depth at $t = .200$ Seconds for Case 4 ($D_p = 0.142$ cm). . . | 105 |
| 3.38 | (a) Soil, Air and Total Stress Versus Depth, and (b) Soil and Air Velocity Versus Depth at $t = .300$ Seconds for Case 4 ($D_p = 0.142$ cm). . . | 106 |
| 3.39 | (a) Soil, Air and Total Stress Versus Depth, and (b) Soil and Air Velocity Versus Depth at $t = .400$ Seconds for Case 4 ($D_p = 0.142$ cm). . . | 107 |
| 3.40 | Air Overpressure Versus Time at Various Station Depths for Case 4 ($D_p = 0.142$ cm) | 109 |
| 3.41 | Soil Velocity Versus Time at Various Station Depths for Case 4 ($D_p = 0.142$ cm) | 110 |
| 3.42 | Tracer Point Positions Versus Time for DICE Case 1 ($D_p = 0.1$ cm), (a) Unadjusted and (b) Adjusted | 112 |
| 3.43 | Main Surface Displacement Versus Time for DICE Cases 1 to 4, (a) Unadjusted and (b) Adjusted. . | 114 |

LIST OF ILLUSTRATIONS (continued)

| <u>Figure</u> | <u>Page</u> |
|--|-------------|
| 3.44 Main Surface Displacement Versus Time Observed in Experiments (Zernow <i>et al.</i> , 1973) and Cal- culated by DICE (Cases 1 and 2) | 115 |
| 3.45 Comparison of Near-Surface Marked Sand Layer Positions Versus Time Observed in Experiments (Zernow <i>et al.</i> , 1973) and Adjusted Near-Surface Tracer Point Positions for DICE Case 1 ($D_p = 0.1$ cm) | 117 |
| 3.46 Adjusted Near-Surface Tracer Point Positions Versus Time for DICE Case 1 ($D_p = 0.1$ cm) and Case 2 ($D_p = 0.05$ cm) ^p | 119 |
| 3.47 Time of Fluidization Versus Depth for DICE Cases 1 to 4 | 120 |
| 3.48 Comparison of Calculated (DICE Cases 1 to 4) and Observed (Zernow <i>et al.</i> , 1973) Peak Over- pressure at Various Depths in the Sand Column. . | 122 |
| 3.49 Comparison of Calculated (DICE Cases 1 to 4) and Observed (Zernow <i>et al.</i> , 1973) Time of Arrival of Peak Overpressure at Various Depths in the Sand Column | 124 |
| 3.50 Comparison of Calculated (DICE Cases 1 to 4) and Observed (Zernow <i>et al.</i> , 1973) Time of Arrival of 10% Level of Peak Overpressure at Various Depths in the Sand Column. | 126 |
| 4.1 Location of Charges and Various Measurement Gauges in MISERS BLUFF II-2. | 129 |
| 4.2 Airblast Time Histories Measured at 25 m Radius in MISERS BLUFF II-2 | 130 |
| 4.3 Vertical Velocities Measured in MISERS BLUFF II-2 from Ground Motion Gauges Originally at 0.5 m Depth. | 131 |

LIST OF ILLUSTRATIONS (continued)

| <u>Figure</u> | | <u>Page</u> |
|---------------|---|-------------|
| 4.4 | Vertical Displacements Measured in MISERS BLUFF II-2 from Ground Motion Gauges Originally at 0.5 m Depth. | 132 |
| 4.5 | Overpressure Loading Function Versus Time Used in DICE Case 5 and Airblast Time Histories Observed in MISERS BLUFF II-2. | 134 |
| 4.6 | Calculational Profile for the 120° and 300° Radials at MISERS BLUFF II-2 (Reference 11). . . | 135 |
| 4.7 | Calculational Profile for the 270° Radial at MISERS BLUFF II-1 (Reference 11) | 136 |
| 4.8 | Grid Used for DICE 1-D MISERS BLUFF II-2 Calculation, Case 5. | 138 |
| 4.9 | (a) Soil, Air and Total Stress Versus Depth, and (b) Soil and Air Velocity Versus Depth at $t = .047$ Seconds for Case 5 (MBII-2) | 141 |
| 4.10 | (a) Soil, Air and Total Stress Versus Depth, and (b) Soil and Air Velocity Versus Depth at $t = .101$ Seconds for Case 5 (MBII-2) | 142 |
| 4.11 | (a) Soil, Air and Total Stress Versus Depth, and (b) Soil and Air Velocity Versus Depth at $t = .203$ Seconds for Case 5 (MBII-2) | 143 |
| 4.12 | (a) Soil, Air and Total Stress Versus Depth, and (b) Soil and Air Velocity Versus Depth at $t = .400$ Seconds for Case 5 (MBII-2) | 144 |
| 4.13 | (a) Soil, Air and Total Stress Versus Depth, and (b) Soil and Air Velocity Versus Depth at $t = .600$ Seconds for Case 5 (MBII-2) | 145 |
| 4.14 | Vertical Velocity Time History Comparisons, Case 5 Versus MISERS BLUFF II-2 Experimental Data at 25 m Radius and 0.5 m Initial Depth. . . | 148 |

LIST OF ILLUSTRATIONS (continued)

| <u>Figure</u> | | <u>Page</u> |
|---------------|---|-------------|
| 4.15 | Vertical Displacement Time History Comparisons, Case 5 Versus MISERS BLUFF II-2 Experimental Data at 25 m Radius and 0.5 m Initial Depth. . . | 149 |

LIST OF TABLES

Table

| | | |
|-----|---|-----|
| 1.1 | Cases Performed and Analyzed | 16 |
| 2.1 | Sound Speed for Multiphase Mixture | 43 |
| 3.1 | Summary of Overpressure Versus Time Data at Selected Depths for 8" Diameter Shock Tube Experiments (Zernow <u>et al.</u> , 1973). | 125 |
| 4.1 | MISERS BLUFF II-2 Material Properties. | 139 |

SECTION 1

INTRODUCTION AND SUMMARY

1.1 BACKGROUND

The airblast from near-surface explosions can induce motions in the ground which will damage structures near the surface. Predictive calculations of airblast-induced ground motion have generally assumed that: (1) the air/ground interface acts as an impermeable membrane and (2) any effects of air contained in the ground are incorporated in the pore crush-up portions of the constitutive equations used to model the stress-strain response of the ground material.

Observations and measurements from several field and laboratory experiments suggest that a more complex multiphase interaction between the air and soil occurs which may substantially influence near-surface ground motion wave forms. In particular, some vertical velocity records from several HE field tests, e.g., MISERS BLUFF II-2¹ and PRE-MINE THROW IV-6², exhibit an enhanced upward velocity immediately following the initial airblast-induced downward motion. Also, laboratory experiments show the development of upward soil motions during positive air overpressure loading³; this motion was shown to be related to the flow of the air through the soil pores.

Porosities of soils may be 30-40%, which means that the solid soil particles form a "lattice" or connected network which contains 30-40% pore volume filled with air and/or water. For dry soils, pore-air effects refer to phenomena related to the

soil pores being filled with air and interacting with the solid soil particles.

In this study, the effects of pore-air on ground motions in dry porous soils are numerically simulated in one space dimension and time. Also, experimentally observed ground motions involving enhanced vertical velocities are explained using two-phase (soil and air) physics including the flow of air through the soil pores, and fluidization of the soil.

1.2 OBJECTIVES AND APPROACH

The numerical simulations use the multiphase DICE code⁴ which has previously been applied to nuclear burst problems involving soil-air interactions above the ground surface.* The mixing of solid/liquid soil particles with the atmosphere and fireball generally involved dust/pebble concentrations which were comparable to the air density ($\rho \sim 10^{-3}$ gm/cm³) or lower. Thus, most of the soil-air flow/interactions were in the aerodynamic drag regime. However, the current investigation involves the near-surface soil material which has an initial soil density of ~2 gm/cm³.

The research objectives were to:

1. Develop and implement a consistent flow/interaction (i.e., generalized drag) model involving soil and pore-air constituents for all soil to air density ratios.

*The soil material was injected into the atmosphere as dust/pebble particles using analytical models for crater ejecta (in surface bursts) or surface sweep-up of soil particles (in air bursts).

2. Numerically simulate and analyze the pore-air phenomenology and induced ground motions in one space dimension at the 100 psi peak overpressure range after a 1 Mt burst on porous soils with various permeabilities.
3. Perform and analyze cases which could be compared with laboratory and field test experimental data.

A model describing the soil-air interaction and flow has been developed and implemented in the multiphase DICE code. The flow/interaction model specifies the internal mutual interaction forces between the soil "lattice" and the pore-air as a function of relative velocity, soil porosity, and a characteristic soil particle size. The model is described in Section 2.3.

Table 1.1 summarizes the five cases performed and analyzed. In Cases 1 through 4, vertical ground motions are numerically simulated for homogeneous porous soils which vary in initial permeability* by a factor of 8. The airblast history (100 psi peak overpressure) applied to the soil surface is similar to a 1 Mt ideal airblast history⁵ (see the bottom of Table 1.1). Case 5 is a calculation of the vertical ground motions corresponding to one location in the HE multiburst experiment MISERS BLUFF II-2 (see Section 4). Three ground material layers were modeled based on measured material properties including hysteretic load-unload paths. The measured airblast loading used in the calculation is also shown on Table 1.1.

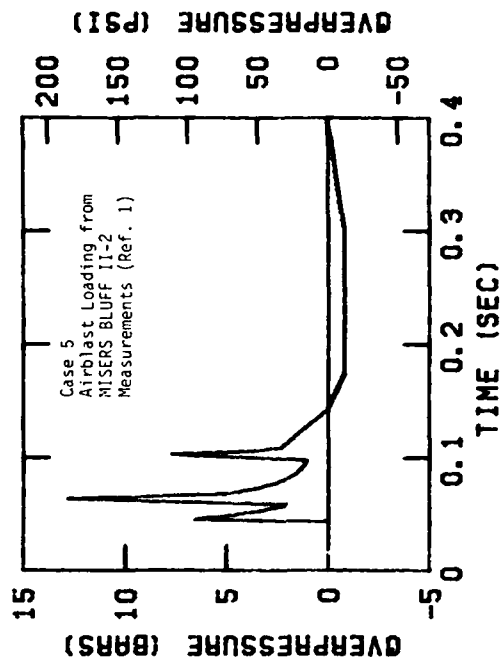
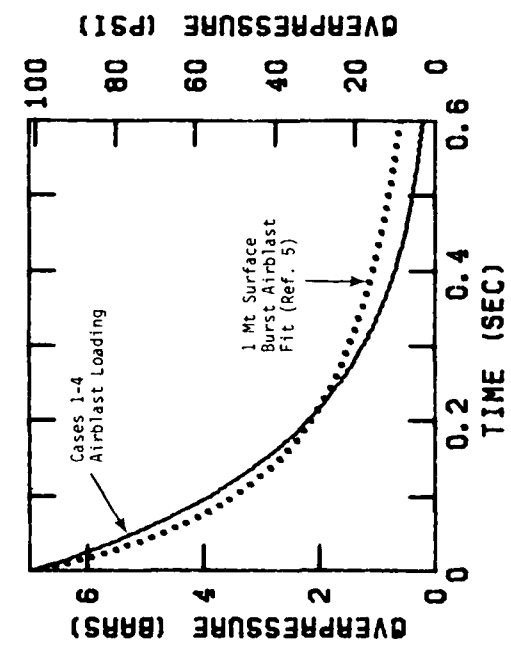
Cases 1 to 4 are described and compared to laboratory vertical shock tube tests³ in Section 3, and Case 5 is described

*Note that the soil permeability (k) depends on both porosity and the characteristic particle size (D_p) as described in Section 2.3. Therefore, D_p will be used to show differences in permeability for the various cases, where $k \propto D_p^2$.

Table 1.1. Cases Performed/Analyzed.

| Case | Initial Soil Parameters | | | | Gravity | Comment |
|------|---|----------------------------|--|---------------------------------|---------------|---------|
| | Density ρ_0 (g/cm ³) | Porosity ν_a (%) | Characteristic Particle Size D_p (cm) | Permeability k (Darcy)* | g (cm/s/s) | |
| 1 | 1.6 | 33.3 | .1 | 469 | 980 | |
| 2 | 1.6 | 33.3 | .05 | 117 | 980 | |
| 3 | 1.6 | 33.3 | .05 | 117 | 0 | |
| 4 | 1.6 | 33.3 | .1422 | 948 | 0 | |
| 5 | Layer 1 1.32 | 44.0 | .0005 | 0.039 | 980 | |
| | Layer 2 1.75 | 32.6 | .04 | 69.4 | 980 | |
| | Layer 3 2.06 | 1.0 | .08 | .003 | 980 | |

*1 Darcy = 9.87×10^{-9} cm²

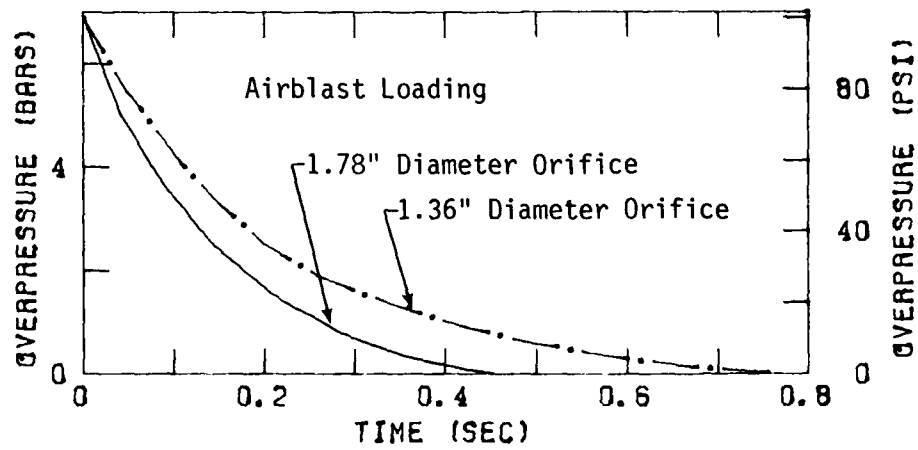


and compared to the MISERS BLUFF measured ground motions in Section 4. Multiphase flow theory and DICE code modeling techniques are described in Section 2.

1.3 SUMMARY OF RESULTS

Pore-air phenomena were studied by Zernow *et al.*³ in a series of laboratory experiments. The experiments involved the use of a shock tube to load the surface of a column of sand with overpressure histories similar to the positive phase of the ideal airblast at the 100 psi range from a 1 Mt nuclear burst. The motion of the sand column was observed photographically. The DICE numerical simulation Cases 1 to 4 had a similar overpressure loading function applied at the soil surface.

Figure 1.1 shows the surface displacements observed in the laboratory experiments compared to those calculated in DICE Cases 1 and 2. The 1.78" diameter orifice experiments (see Section 3) had a faster decay rate in the airblast loading compared to the 1.36" diameter orifice experiments, as shown below:



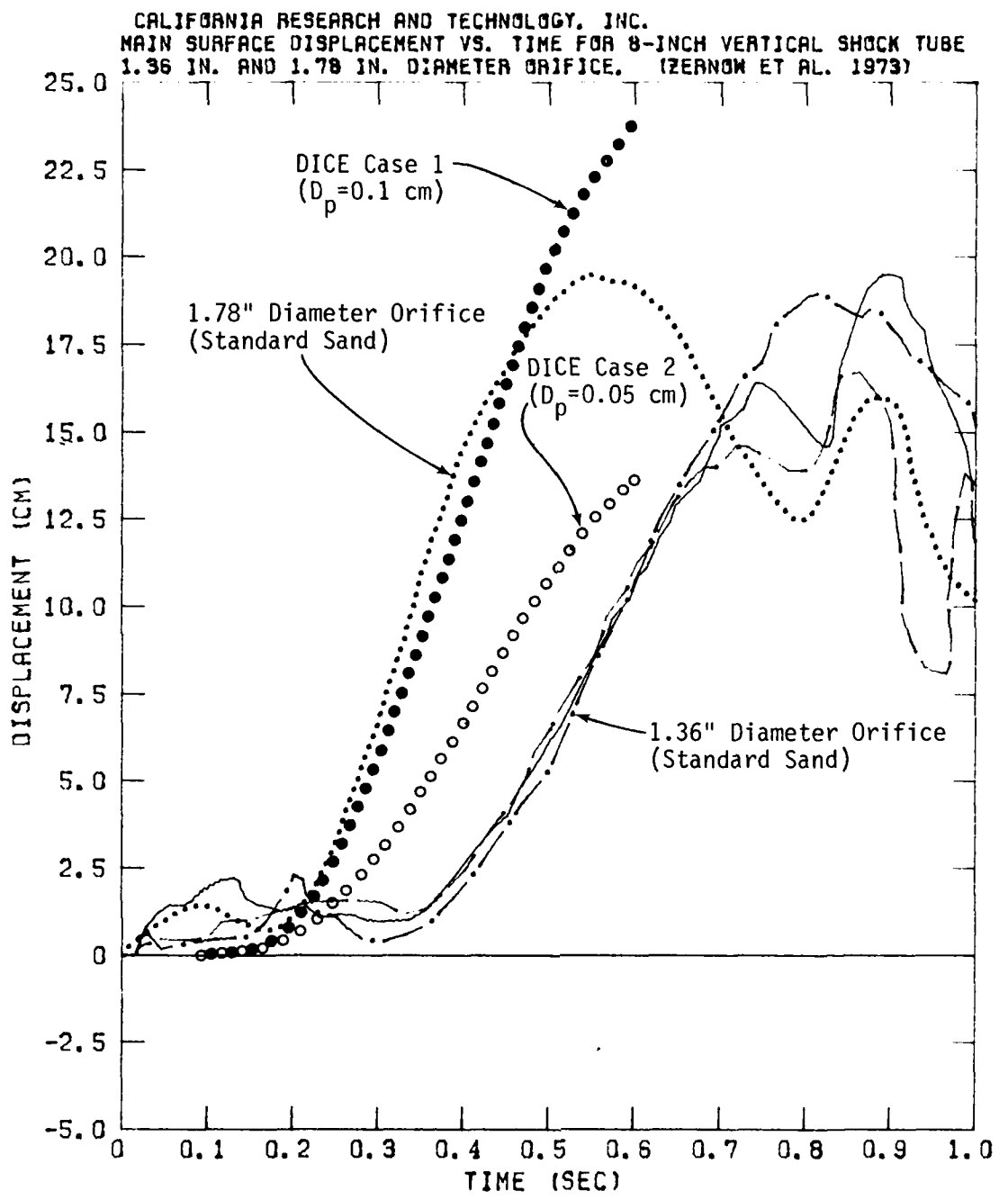


Figure 1.1. Main Surface Displacement Versus Time Observed in Experiments (Zernow et al., 1973) and Calculated by DICE (Cases 1 and 2).

The result is an earlier upward motion of the main sand column (~.200 s compared to ~.400 s) and higher velocity (~75 cm/s compared to ~45 cm/s) for the 1.78" diameter orifice experiments. Maximum heights of nearly 20 cm are attained by the lofted sand. In the absence of a sustained upward force acting on the sand, the initial lofting velocity needed to reach 20 cm height is $V = \sqrt{2gH} \sim 200$ cm/s. Thus, the experimental and numerical results provide convincing evidence of the sustained application of an upward force associated with pore-air phenomena.

The surface displacement in Case 1 is similar to the 1.78" diameter orifice experiment. Both surfaces start to move upward at $t \sim .200$ s and maintain an approximately constant upward velocity until $t \sim .400$ s. The continuing rise of the soil surface in Case 1 above the experimental curve is due to the longer duration of the airblast loading function used in the numerical simulation.

The upward surface displacement in Case 2 also begins at $t \sim .200$ s, but a smaller constant upward velocity develops. The smaller displacements and velocities compared to Case 1 are indicative of a smaller sustained upward force resulting from the permeability dependence of the internal interaction (drag) forces. The factor of 2 smaller characteristic particle size used in Case 2 yields a factor of 4 decrease in modeled permeability compared to Case 1.

The fact that the soil surface displaces upward during the positive air overpressure loading on the surface is a pore-air flow phenomenon. High pressure air flows into the porous soil from the airblast loading on the surface. As air flows or permeates downward through the soil pores, the pore-air pressure

increases and the total applied pressure load supported by the solid soil particles decreases. Thus, $P_{\text{total}} = P_{\text{soil}} + P_{\text{air}}$. Fluidization of the soil occurs when the soil particles lose contact with each other and the total pressure is entirely supported by the pore-air. Once fluidization occurs, the fluidized soil displaces upward (with respect to the unfluidized soil). These phenomena are described in more detail in Section 3.2 for Cases 1 to 4 and illustrated on Figures 1.2 and 1.3.

Figure 1.2 shows the pressure and velocity versus depth profiles at $t = .200$ s for Cases 1 and 2. The pressure profiles (at top of figure) show the extent of fluidization to be ~40 cm in Case 1 and ~25 cm in Case 2. The velocity profiles (at bottom of Figure 1.2) indicate that there is an upward acceleration of the soil material associated with fluidization. The soil is moving downward at a constant velocity of ~23 cm/s below the fluidized region. The air is permeating down through the soil below the fluidized region, and is flowing up and out of the soil in the fluidized region. For the more permeable soil modeled in Case 1, the air has larger downward velocities and flows through the soil pores to greater depths. A greater relative velocity between the air and soil is also present in the fluidized region for Case 1 as compared to the less permeable soil in Case 2.

Figure 1.3 shows the pore-air overpressure and soil particle velocity versus time at various depths in the soil for Case 1. At a given depth, the air overpressure gradually rises to a peak and then decays to a level approximately equal to the applied surface overpressure at which time the soil becomes fluidized. The soil velocity histories (Figure 1.3b) show that up to $t \sim .100$ s the entire soil column essentially moves downward as a rigid body. Fluidization at each station depth becomes apparent

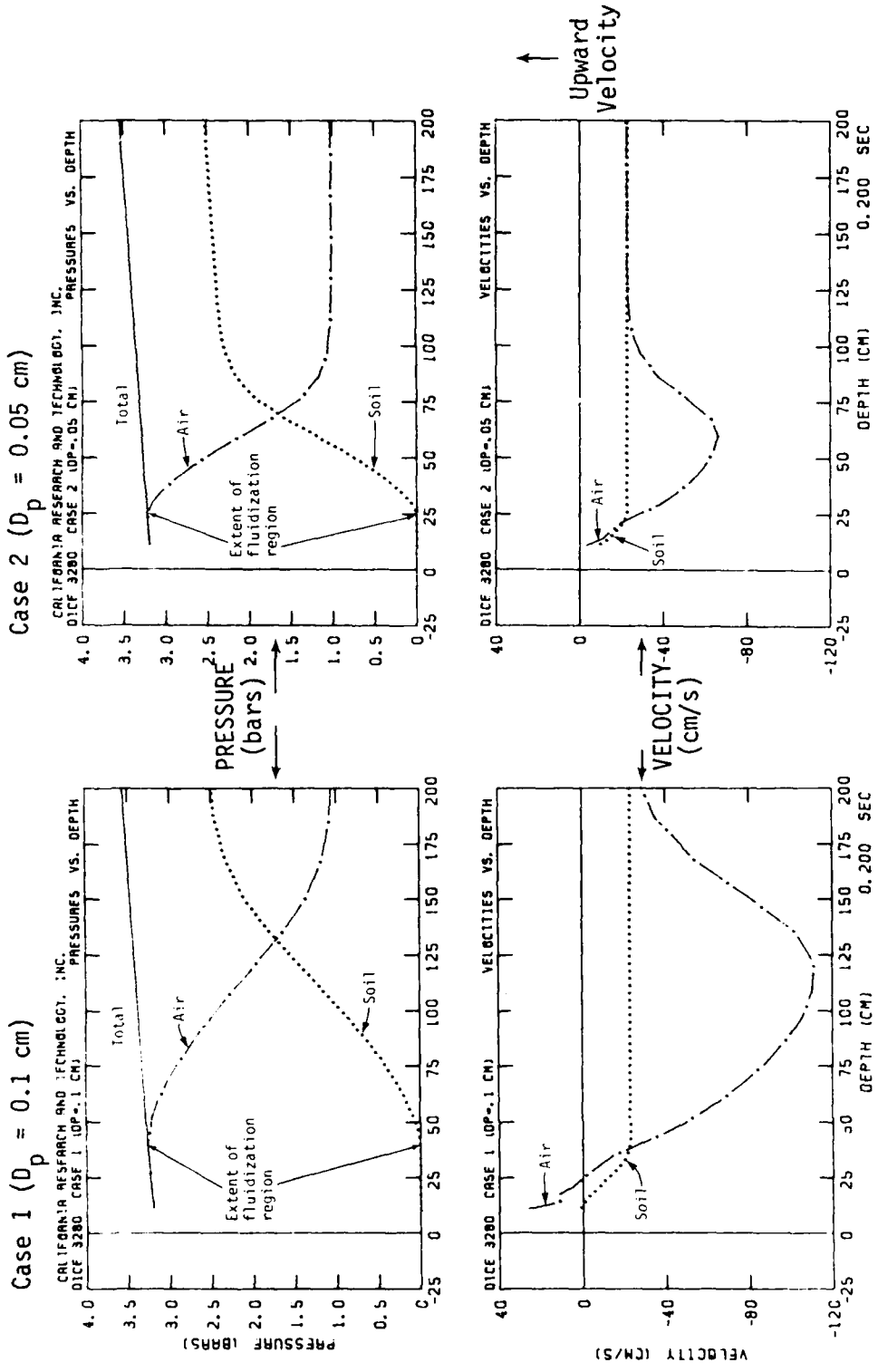
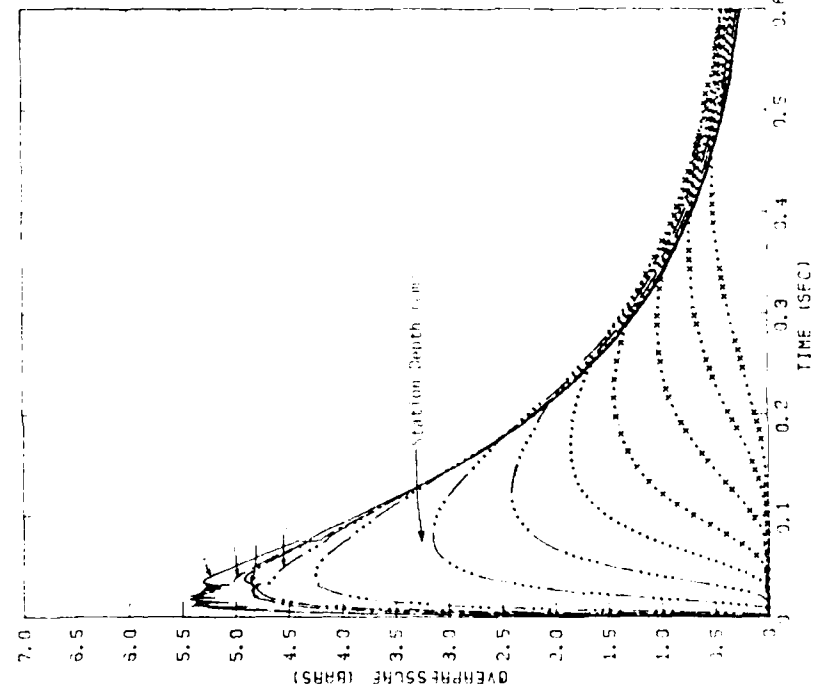


Figure 1.2. Pressure and Velocity Profiles Versus Depth at $t = .200$ Seconds for Cases 1 and 2.

(a) Pore-Air Overpressures



(b) Soil Particle Velocities

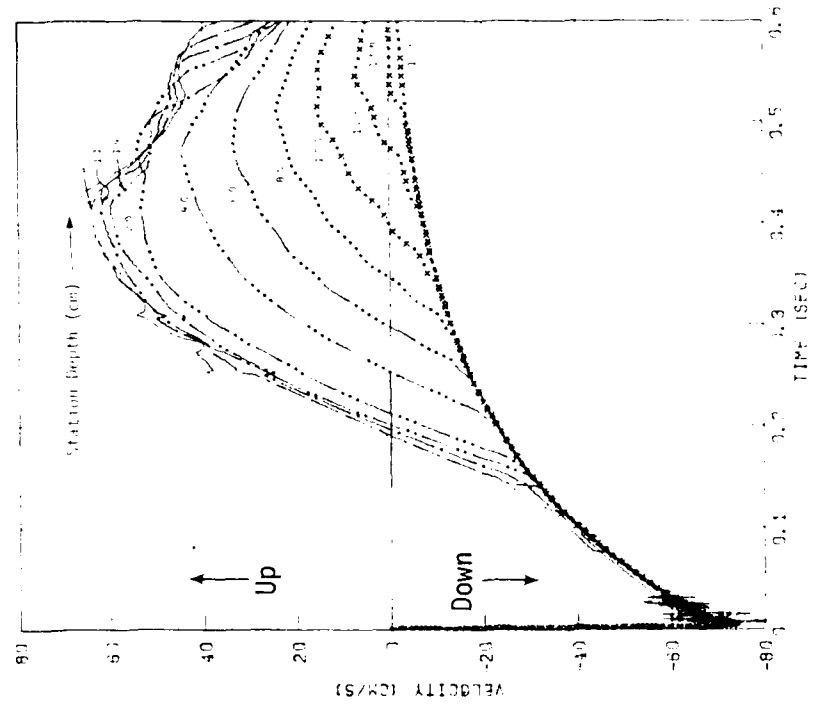


Figure 1.3. (a) Pore-Air Overpressure and (b) Soil Velocity Versus Time at Various Station Depths for Case 1 ($D_p = 0.1$ cm).

after this time when the soil flowing at that depth suddenly accelerates its velocity above the velocity of the soil column below that depth.

The progression of fluidization down through the soil column is shown on Figure 1.4a for Cases 1 to 4. For Case 1 the "fluidization front" moves down the soil at ~4 m/s. The fluidization front moves more slowly at ~2 m/s for the less permeable soil modeled in Case 2. In Case 3, the soil at a given depth is fluidized earlier than in Case 2 because there is no lithostatic pressure distribution ($g = 0$) in the soil to be overcome by the pore-air before fluidization occurs. A fluidization front velocity of ~7 m/s is predicted for the highly permeable soil in Case 4.

Figure 1.4b shows the calculated peak air overpressure arrival times versus depth for Cases 1 to 4; the experimental data are also shown for comparison. The more permeable soils allow air to travel faster down the soil pores, causing earlier arrival times for the peak overpressure. The slope of the peak arrival time versus depth curves for Cases 1 to 4 are quite similar to the soil fluidization time versus depth curves in Figure 1.4a. For each case there is a delay of ~.080 to .120 s after the arrival of the peak overpressure at a given depth until soil fluidization begins at that depth.

The MISERS BLUFF II-2 experiment involved the simultaneous detonation of six high-explosive charges forming a hexagon 100 m on a side. An approximation to the airblast measured at 25 m radius from the center of the hexagon was used in Case 5 as the overpressure loading function. In this case, the airblast

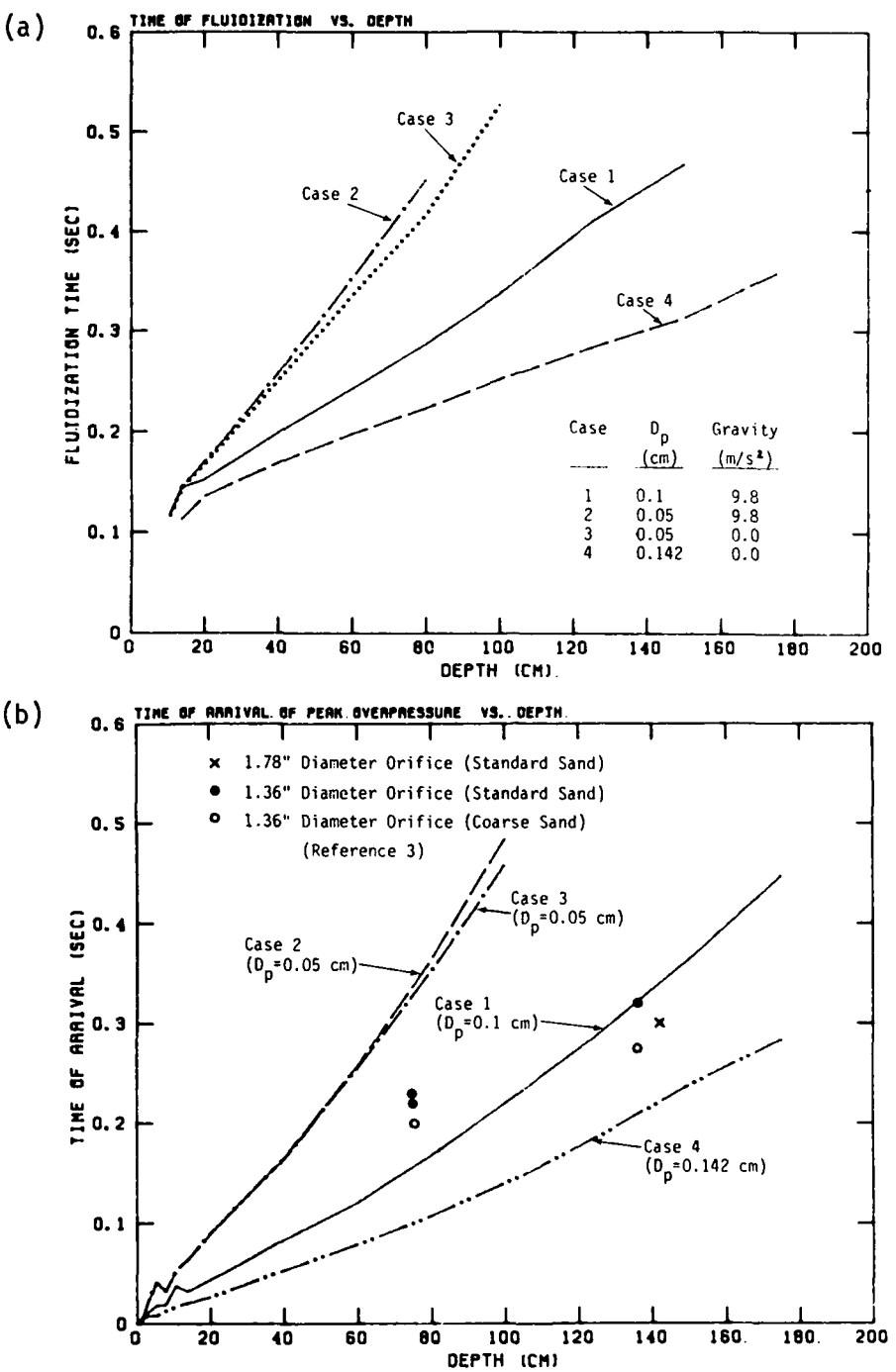


Figure 1.4. (a) Time of Fluidization Versus Depth for Cases 1 to 4 and (b) Comparison of Calculated (Cases 1 to 4) and Observed (Zernow et al., 1973) Time of Arrival of Peak Overpressure at Various Depths.

included a negative overpressure phase beginning at $t \sim .150$ s and returning to zero overpressure at $t \sim .400$ s.

The material properties for the MISERS BLUFF II-2 calculation (Case 5) involved three soil layers including hysteresis and the associated variation in load-unload constrained moduli. The initial soil permeabilities in Case 5 were much smaller than in Cases 1 to 4 where the initial permeabilities were in the $10^2 - 10^3$ Darcy range ($1 \text{ Darcy} = 9.87 \times 10^{-9} \text{ cm}^2$). In Case 5, the initial permeabilities were different in each soil layer - $k = .04$ Darcy for the top layer, $k = 69$ Darcy for Layer 2 and $k = .003$ Darcy for Layer 3. The low permeability in the top layer limited the amount of high pressure air which flowed into the soil. Also, the internal interaction forces between the air and soil particles (i.e., drag) increased with the decrease in permeability, so that the relative air-soil velocities were nearly zero.

Sustained upward velocities and fluidization of the MISERS BLUFF II-2 soils occurred primarily because of the negative overpressures in the airblast and the associated expansion of the pore-air in the soil; the pore-air expands so that pressure equilibrium can be attained with the applied airblast pressure. If the soils were not hysteretic, this fluidization would begin when the negative overpressures were first applied to the incohesive soils. The hysteresis in the soils, however, permit fluidization to occur at small positive overpressures since the soil irreversibly compacts and cannot support stresses, upon unloading, at soil densities slightly above the initial density.

Various ground motion gauges originally at 0.5 m depth and 25 m radius in MISERS BLUFF II-2 measured the vertical velocity

(and thus displacement) time histories. Figure 1.5 compares the experimental vertical velocity and displacement data with the Case 5 predictions of a tracer particle originally at 0.5 m depth. The sustained upward velocity from $t \sim 0.150$ s to beyond $t \sim 0.400$ s demonstrates the important role of pore-air phenomena during the negative overpressure phase in low permeability soils.

1.4 CONCLUSIONS AND RECOMMENDATIONS

1. Large sustained upward velocities can develop in near-surface soils subjected to airblast loading due to soil fluidization caused by pore-air phenomena.
2. In the laboratory experiments³ involving relatively high soil permeabilities, the 100 psi peak overpressure airblast caused air to flow through the soil pores, thereby increasing pore-air pressures which resulted in soil fluidization during the positive overpressure phase. Peak pore-air flow speeds of ~15 m/s are predicted, and the soil fluidization front propagates at ~4 m/s (Case 1).
3. In the MISERS BLUFF II-2 field experiment¹ involving low soil permeabilities and almost no pore-air flow, soil fluidization and sustained upward velocities occurred during the negative overpressure phase as the pore-air in the soil expanded to reach pressure equilibrium with the low airblast pressure.
4. The DICE code numerical simulations (Cases 1 to 5) reproduced the phenomenology observed in the laboratory and field experiments. The relatively simple models used for soil permeability and internal interaction forces (drag) were adequate for quantitatively reproducing the experimental data; however,

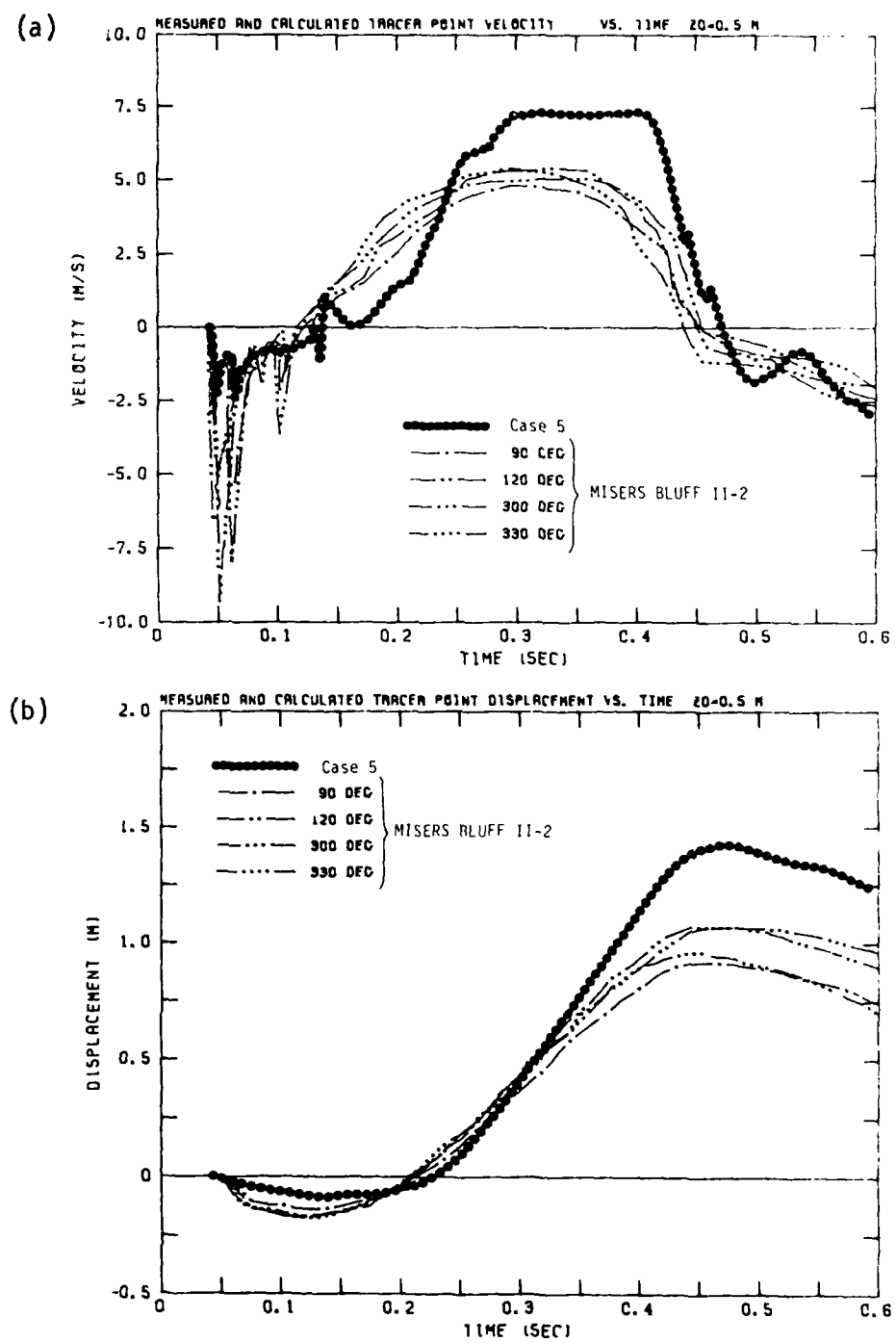
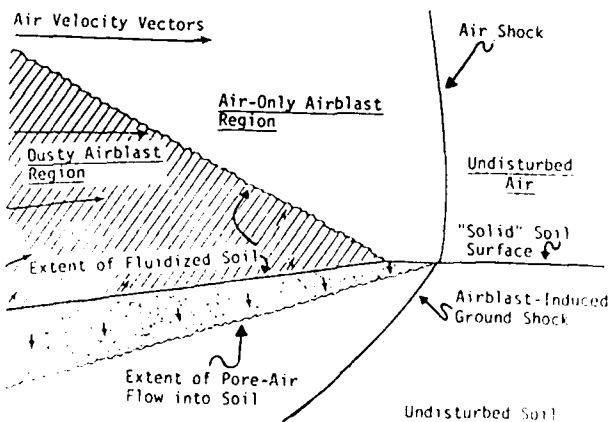


Figure 1.5. (a) Vertical Velocity and (b) Vertical Displacement Time History Comparisons, Case 5 Versus MISERS BLUFF II-2 Experimental Data at 25 m Radius and 0.5 m Initial Depth.

the in-situ soil permeability is a sensitive physical parameter and careful measurements and model calibrations will be necessary before quantitative predictions and associated uncertainties of ground motions can be made concerning strategic/tactical sites of interest.

5. The following recommendations are suggested:

- Evaluate the pore-air and associated soil fluidization effects on ground motions for peak overpressures up to 1 kbar ~15,000 psi.
- Obtain in-situ soil permeability measurements for strategic and tactical sites of interest.
- Extend the pore-air analysis capability to pore-air-water environments since most soil pores contain some water; and in fact, many cases of interest involve saturated or nearly saturated soils below some depth.
- Analyze the importance of pore-air and soil fluidization phenomena in two space (2-D) dimensions for propagating airblast waves which interact with surface dust/pebble material. (See following sketch.) Both experimental and theoretical analyses should be conducted.



Schematic of Two-Dimensional Soil-Air Interactions Behind Air Shock

SECTION 2

MULTIPHASE THEORY

2.1 GOVERNING PHYSICAL EQUATIONS - GENERAL FORMULATION

Consider a bounded volume Ω with surface area S which contains physically distinct material phases. Distinct phases can include solid, liquid and/or vapor phases as well as individual phases distinguished by particle type/size. If the volume of each phase is Ω_k , where $k = 1$ to K , then

$$\Omega = \sum_{k=1,K} \Omega_k$$

or

$$1 = \sum_{k=1,K} \Omega_k / \Omega = \sum_{k=1,K} v_k$$

where

$$v_k = \Omega_k / \Omega \text{ is the } \underline{\text{Volume Fraction.}} \quad (2.1)$$

The continuum mechanics concept of a mass density for each phase is assumed. Thus, as a test volume Ω' and associated phase volume Ω'_k become small, the mass M'_k and the average and local densities are related by

$$\rho_k = \lim_{\Omega' \rightarrow 0} (M'_k / \Omega') ; \quad \rho_k \text{ is } \underline{\text{average density}}$$

$$\hat{\rho}_k = \lim_{\Omega' \rightarrow 0} (M'_k / \Omega'_k) = \rho_k / v_k ; \quad \hat{\rho}_k \text{ is } \underline{\text{local density}}$$

The total mass density is then

$$\rho_{\text{total}} = \sum_{k=1,K} \rho_k = \sum_{k=1,K} \hat{\rho}_k v_k \quad (2.2)$$

The dynamic physical equations for each phase (and thus for the entire multiphase system) involve identical considerations concerning conservation of mass, momenta and energy. For simplicity, and without any loss in generality, the subscript k for each phase will be dropped in the following derivation. Thus, the mass, momenta and energy of any one material phase in a volume Ω are given by

$$M(t) = \int_{\Omega} \rho dV$$

$$MOM^i(t) = \int_{\Omega} \rho u^i dV = \int_{\Omega} \rho \ddot{u} dV \quad (2.3)$$

$$EN(t) = \int_{\Omega} \rho (e + \frac{1}{2} u^j u_j) dV = \int_{\Omega} \rho E dV$$

where

ρ is the average density of one phase ($\rho = \hat{\rho} v$),

u^i is the local velocity vector of one phase,

e is local specific internal energy of one phase, and

E is specific total energy = $e + \frac{1}{2} u^i u_i$ of one phase.

The summation convention on repeated indices is assumed, and a comma preceding an index will indicate covariant differentiation.

The dynamic equations of motion will be derived for arbitrary changes in the volume $\Omega = \Omega(t)$ since the DICE code uses an expanding computational grid which is not coupled to the material particle velocity. The horizontal and vertical grid lines are permitted to move with arbitrary velocities, u_S^i . Thus, in general, the volume Ω and surface area S of the computational cells will vary with time in a prescribed fashion. The following fundamental equation relates the time derivative of a volume integral to the arbitrary surface velocity u_S^i (Ref. 6, Eqn. 81.4):

$$\frac{d}{dt} \int_{\Omega} \psi dV = \int_{\Omega} \frac{\partial \psi}{\partial t} dV + \int_S \rho u_S^j dA_j \quad (2.4)$$

where $\psi = \psi(x^i, t)$ is an arbitrary tensor and dA_j is the outward surface vector.

Equations (2.3) and (2.4) can be used to obtain the dynamic mass, momentum and energy equations in terms of volume and surface integrals. The approach for the mass equation is indicated below.

Letting $\psi = \rho$ in Equation (2.4) gives

$$\frac{dM(t)}{dt} = \int_{\Omega} \frac{\partial \rho}{\partial t} dV + \int_S \rho u_S^j dA_j \quad (2.5)$$

The usual global conservation of mass equation in integral form is obtained by letting $u_S^i = u^i$, i.e., the surface S moves with the particle velocity u^i and therefore the mass contained in $\Omega(t)$ is constant if there are no mass sources. Thus,

$$0 = \int_{\Omega} \frac{\partial \rho}{\partial t} dV + \int_S \rho u^j dA_j \quad (\text{no mass sources in Lagrangian frame})$$

If there are mass sources for this phase, for example from the vaporization of a solid phase to a vapor phase, then the mass source term can be written as

$$\frac{dM(t)}{dt} = \int_{\Omega} \dot{\rho}_+ dV \quad (\text{mass source term in Lagrangian frame}) \quad (2.6a)$$

where $\dot{\rho}_+$ is the mass source per unit volume. Thus, one form* of the dynamic mass equation is

$$\int_{\Omega} \dot{\rho}_+ dV = \int_{\Omega} \frac{\partial \rho}{\partial t} dV + \int_S \rho u^j dA_j \quad (\text{Lagrangian frame}) \quad (2.6b)$$

Subtracting Equation (2.6b) from Equation (2.5) and rearranging terms, we obtain

$$\frac{dM(t)}{dt} \equiv \frac{d}{dt} \int_{\Omega} \rho dV = \frac{\rho(u_s^j - u^j)}{S(t)} dA_j + \int_{\Omega} \dot{\rho}_+ dV \quad (2.7)$$

Equation (2.7) is the integral form of the mass equation for an arbitrary moving volume $\Omega(t)$.

In a similar fashion, the momenta and energy equations are obtained. However, surface and body forces acting on $S(t)$ and in $\Omega(t)$ must now be considered since these forces generate momenta and energy. The surface forces per unit area are obtained from a material stress tensor σ^{ij} , which for hydrodynamic problems is

*Using the Gauss divergence theorem to change the surface integral to a volume integral, we find the usual differential equation forms

$$\dot{\rho}_+ = \frac{\partial \rho}{\partial t} + (\rho u^j)_{,j} = \dot{\rho} + \rho u^j_{,j}$$

$\sigma^{ij} = -P\delta^{ij}$; thus, the surface force F_S^i is

$$F_S^i = \int_S \sigma^{ij} dA_j \quad \text{Surface Force} \quad (2.8)$$

Note that only the stresses for the one phase being considered are integrated to get F_S^i for that phase. See Section 2.2 for further discussions of the partitioning of stresses.

Body forces are of two types:

- External Gravitational Body Force

$$\int_{\Omega} \rho g^i dv$$

- Internal Body Force from the relative motions and interactions with other phases (~drag force)

$$\int_{\Omega} f_{int}^i dv$$

Thus, the body force F_B^i is

$$F_B^i = \int_{\Omega} (\rho g^i + f_{int}^i) dv \quad \text{Body Force} \quad (2.9)$$

The surface and body forces in Equations (2.8) and (2.9) represent momenta source terms; in addition, there may be additional momenta sources due to phase changes [analogous to the mass sources in Equation (2.6a)]. Thus, in the Lagrangian or material frame of reference, i.e., $u_S^i = u^i$, we have

$$dMOM^i/dt = F_S^i + F_B^i + \int_{\Omega} \dot{\rho} u^i dv$$

where $\dot{\rho}_+ u_+^i$ are the momenta/volume source terms due to phase changes. And finally, the integral form of the momenta equation for an arbitrarily moving volume $\Omega(t)$ is

$$\begin{aligned} d\text{MOM}^i/dt \equiv d/dt \int_{\Omega(t)} \rho u^i dv &= \int_{S(t)} \{ \rho u^i (u_S^j - u^j) + \sigma^{ij} \} dA_j \\ &+ \int_{\Omega(t)} \{ \rho g^i + f_{int}^i + \dot{\rho}_+ u_+^i \} dv \end{aligned} \quad (2.10)$$

Similarly, the energy equation is

$$\begin{aligned} d\text{EN}/dt \equiv d/dt \int_{\Omega(t)} \rho E dv &= \int_{S(t)} \{ \rho E (u_S^j - u^j) + \sigma^{ij} u_i \} dA_j \\ &+ \int_{\Omega(t)} \{ \rho g^i u_i + f_{int}^i u_i + \dot{Q}_+ \} dv \end{aligned} \quad (2.11)$$

where \dot{Q}_+ represents the energy/volume source terms due, in general, to any combination of phase changes, heat conduction and thermal radiation transport.

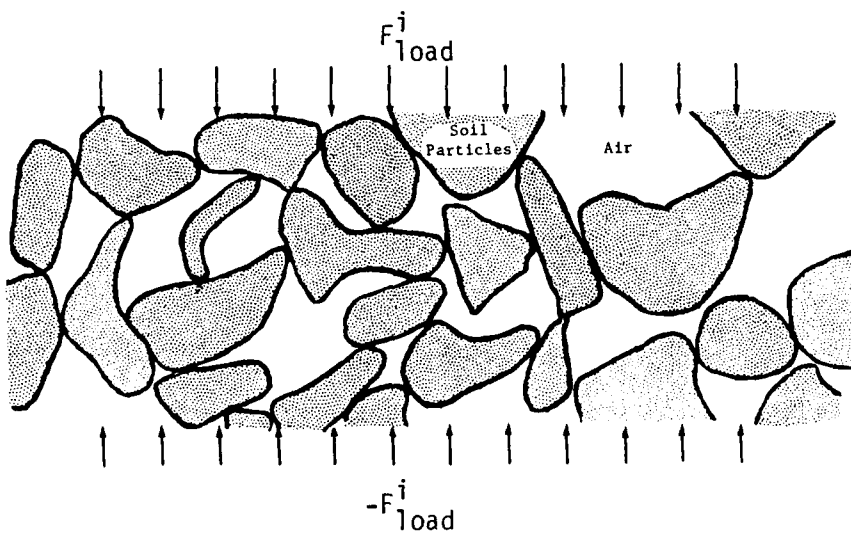
Equations (2.7), (2.10) and (2.11) represent the general dynamic equations governing each phase in a mixed phase flow configuration. Before a solution to a specific problem can be obtained, the initial and boundary conditions must be specified as well as a complete set of constitutive equations including:

- Material Equations of State (elastic-plastic-hydro description of σ^{ij})
- Internal Interaction Forces (f_{int}^i) as a function of relative velocity, pressure, porosity, etc.

The generalized approach for material equations of state in two-phase media is described in Section 2.2, and the specific material parameters are described in Sections 3 and 4 with the case descriptions and calculational results. The formulation used for f_{int}^i for all the cases is described in Section 2.3. And, Sections 2.4 and 2.5 contain DICE test cases.

2.2 STRESS PARTITIONING IN A SOIL-AIR MEDIA

A small portion of a two-phase material consisting of a solid soil phase and a pore-air phase is schematically shown below:



If a loading force, F_i^load , is applied to a surface, S , then

$$F_i^load = \int_S \sigma_{load}^{ij} dA_j \quad (2.12)$$

The partitioning of the load stress, σ_{load}^{ij} , into solid soil and pore-air parts is accomplished by introducing the following equation and associated variables:

$$\sigma_{load}^{ij} = \hat{\sigma}_s^{ij} v_s - \hat{P}_a \delta^{ij} v_a \quad (2.13)$$

where

v_s and v_a are the soil and air area fractions ($v_s + v_a = 1$);

these are often assumed to be equal to the volume fractions, but anisotropic pore/channeling configurations are possible which would invalidate this assumption.

$\hat{\sigma}_s^{ij}$ and $-\hat{P}_a \delta^{ij}$ are the local stresses* such that

$\int \hat{\sigma}_s^{ij} v_s dA_j$ is the force contribution from the soil, and

$\int -\hat{P}_a \delta^{ij} v_a dA_j$ is the force contribution from the air.

The material equations of state (EOS) for the air and the soil complete the specification of Equation (2.13). The air EOS is relatively straightforward:

$$\hat{P}_a = \hat{P}_a(\hat{\rho}_a, e_a) \quad \text{General EOS} \quad (2.14)$$

*These local stresses $\hat{\sigma}_k$ (force/area for one phase) are analogous to the local density $\hat{\rho}_k$ (mass/volume for one phase). Note that the particle velocity and specific internal energy are always local variables in the current formulation and a u or e is suppressed.

For example,

$$\hat{P}_a = (\gamma - 1)\hat{\rho}_a e_a \quad \text{Ideal Gas EOS}$$

The solid soil stress, $\hat{\sigma}_s^{ij}$, is generally not measured; however, the measured soil stress can be identified by noting that for relatively incompressible soil particles, the pore-air pressure (\hat{P}_a) and the stresses supported by the touching soil particles ($\tilde{\sigma}_s^{ij}$) both contribute to the local soil stress,

$$\hat{\sigma}_s^{ij} = \tilde{\sigma}_s^{ij} - \hat{P}_a \delta^{ij} \quad (2.15)$$

and plugging this equation into Equation (2.13), we find

$$\sigma_{load}^{ij} = \tilde{\sigma}_s^{ij} v_s - \hat{P}_a \delta^{ij} \quad (2.16)$$

Thus experiments measuring σ_{load}^{ij} performed on soils with pore pressure \hat{P}_a will provide the soil EOS ($\bar{\sigma}_s^{ij}$), where

$$\bar{\sigma}_s^{ij} = \tilde{\sigma}_s^{ij} v_s, \text{ and} \quad (2.17)$$

$$\sigma_{load}^{ij} = \bar{\sigma}_s^{ij} - \hat{P}_a \delta^{ij}$$

The measured soil EOS ($\bar{\sigma}_s^{ij}$) can be a complicated function of many variables, including density (ρ_s), specific internal energy (e_s), strain, and strain rate.

2.3 INTERNAL INTERACTION (OR DRAG) FORCE

The internal body force per unit volume, f_{int}^i , for the simple two-phase system consisting of air and soil particles of radius R is modeled in this subsection. Note that in a two-phase

system, the internal force acting on the soil by the air is exactly opposite to the internal force acting on the air by the soil.* Thus,

$$\left(f_{int}^i\right)_s + \left(f_{int}^i\right)_a = 0 \quad (2.18)$$

In this exploratory study, Darcy's linear law⁷ is used as the basic equation relating the apparent volumetric fluid (air) flow rate to the fluid pressure gradient, i.e.,

$$v_a u_r^i = \frac{-k}{\mu} \frac{\partial P_a}{\partial x_i} \quad (2.19)$$

where

v_a is air filled porosity of soil

u_r^i is local relative velocity $u_a^i - u_s^i$

$v_a u_r^i$ is the apparent flow velocity of air

k is permeability

μ is the air viscosity

And, since Darcy's law is for steady-state conditions, the pressure gradient on the air is just equal to the internal drag force/volume on the air, thus

$$\left(f_{int}^i\right)_a = \frac{v_a \partial P_a}{\partial x_i} = \frac{-\mu v_a^2}{k} u_r^i \quad (2.20)$$

*In the general multiphase system $\sum_{k=1,K} \left(f_{int}^i\right)_k = 0$

Drag formulations of the internal interaction force define an effective single particle force, F^i , which acts on a single soil particle of radius R . Since $\frac{4\pi R^3}{3v_s}$ is the soil + air volume per soil particle,

$$F^i = -\frac{4\pi R^3}{3v_s} \left(f_{int}^i \right)_a \quad (2.21)$$

In the current study, a single particle drag formulation is used with three porosity regimes. The first regime applies to relatively low porosities, v_a less than or equal to 0.5. In this regime the flow of air through the soil is modeled using a drag formulation of Darcy's law derived by Brinkman⁸:

$$F_1^i = 6\pi\mu u_r^i R \left(1 + \frac{R}{\sqrt{k}} + \frac{R^2}{3k} \right) ; \quad 0 \leq v_a \leq 0.5 \quad (2.22)$$

where

μ = viscosity

u_r^i = relative velocity of air and soil particles,
 $u_r^i = u_a^i - u_s^i$

$R = D_p/2$ = characteristic radius of soil particles

k = permeability

In the derivation of Equation (2.22) it is assumed that the soil particles are rigid spheres and that the air flow is steady and incompressible. These assumptions may not be adequate for a final model but they do permit a first-order assessment of the pore-air phenomena of interest.

The second regime is transitional and applies for $0.5 < \nu_a < 0.8$. In this regime the soil is distended and the individual soil particles are not touching but are still relatively close together. The interaction between the soil and air is a linear interpolation on ν_a between Equation (2.22) and the single particle aerodynamic drag interaction force [Equation (2.24) below]:

$$F_2^i = \frac{(0.8 - \nu_a)}{0.3} F_1^i + \frac{(\nu_a - 0.5)}{0.3} F_3^i \quad (2.23)$$

$$0.5 < \nu_a < 0.8$$

where F_1 is given by Equation (2.22) above and F_3 is given by Equation (2.24).

In the third regime $\nu_a > 0.8$, the soil is highly distended, soil particles are relatively far apart and do not strongly interact, and the soil-air interaction is modeled as single particle drag:

$$F_3^i = \frac{1}{2} \rho_a \pi R^2 C_D u_r^i |u_r^i| \quad ; \quad \nu_a > 0.8 \quad (2.24)$$

where C_D is the variable drag coefficient which, in general, will depend on the relative velocity and local Reynolds number.

In order to calculate the soil-air interaction in regimes 1 and 2, it is necessary to specify the permeability. The permeability of the soil will change as the soil is compressed by the airblast and pores collapse; also, soil cementation is broken and thus the particle size distribution is altered. It is thus essential that permeability be treated as a variable. As an initial model, permeability is assumed to vary with porosity and

characteristic particle size. For porosities less than or equal to about 0.48, an empirically based equation formulated by Carman is used⁷.

$$\frac{k}{R^2} = \frac{v_a^3}{45(1 - v_a)^2} ; \quad v_a \leq 0.4785 \quad (2.25)$$

For higher porosities, a theoretical formulation by Brinkman⁸ is used.

$$\frac{k}{R^2} = \frac{1}{18} \left[3 + \frac{4}{1 - v_a} - 3 \left(\frac{8}{1 - v_a} - 3 \right)^{\frac{1}{2}} \right] \quad (2.26)$$

$$0.4785 < v_a \leq 0.8$$

Figure 2.1 shows the quantity k/R^2 as a function of porosity as calculated from the Carman and Brinkman equations.

2.4 TWO-PHASE FLOW TEST CASE

The details of the internal interaction (or drag) forces and the associated relative velocities (u_r^i) between the air and soil phases will influence the wave propagation characteristics in the soil-air medium. Under the special case of $u_r^i = 0$ which occurs as the permeability goes to zero, the sound speed in the two-phase medium is related to the soil and air densities, local sound speeds, and volume fractions as shown on Table 2.1. Note that when $v_a = v_s = 0.5$, the two-phase sound speed reaches a minimum and is a small fraction of the air sound speed⁹, in fact

$$C \sim 2 \sqrt{\rho_a / \rho_s} C_a$$

$$\text{for } v_a = v_s = 1/2$$

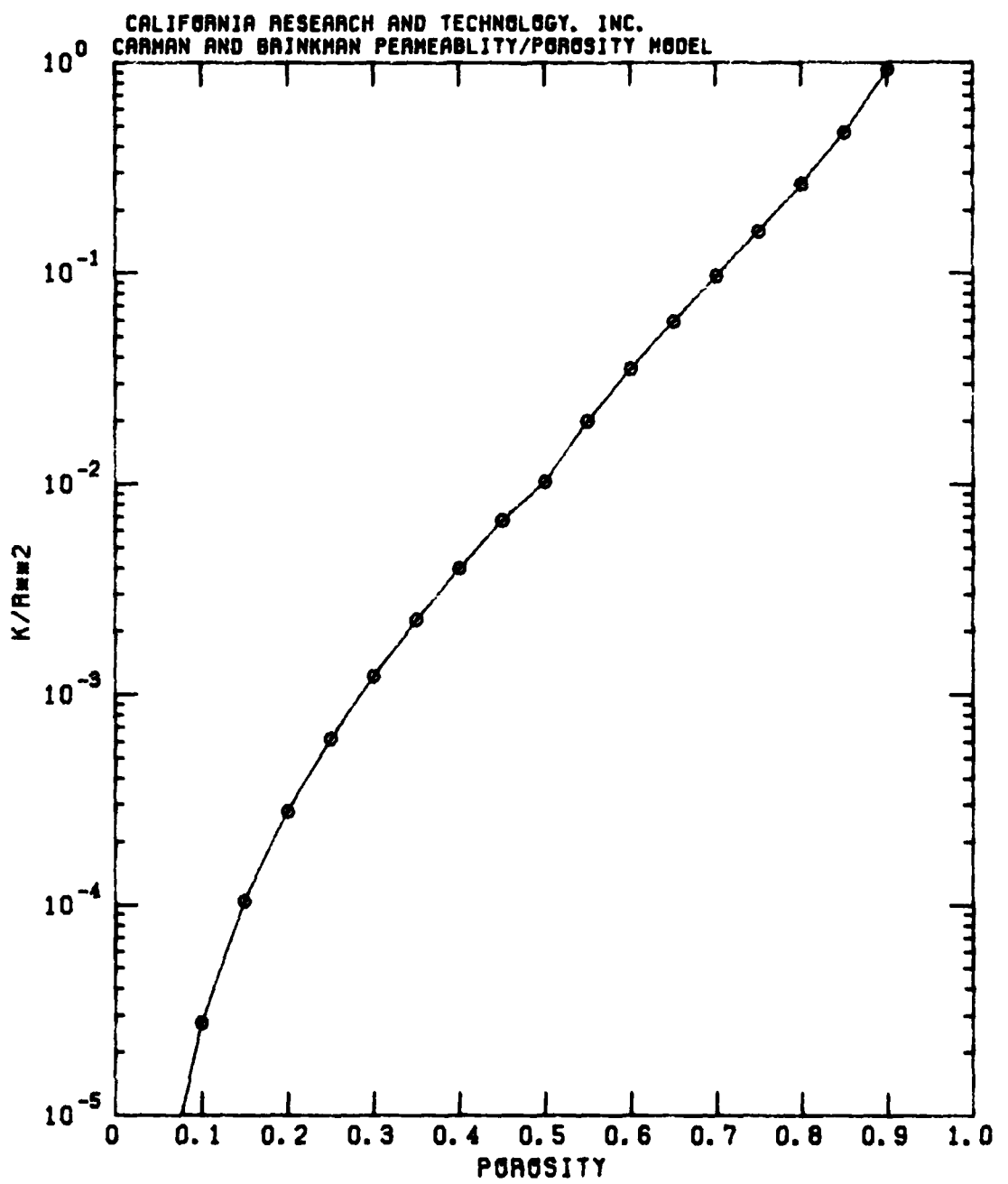


Figure 2.1. Normalized Permeability (k/R^2) Versus Porosity from the Carman and Brinkman Equations.

Table 2.1. Sound Speed for Multiphase Mixture.

(particles not in contact with one another and $u_r^i = 0$)

$$C^2 = \frac{(\rho_s C_s^2 + \rho_a C_a^2)}{\left[v_s \rho_a C_a^2 + v_a \rho_s C_s^2 \right] \left[v_s \rho_s + v_a \rho_a \right]}$$

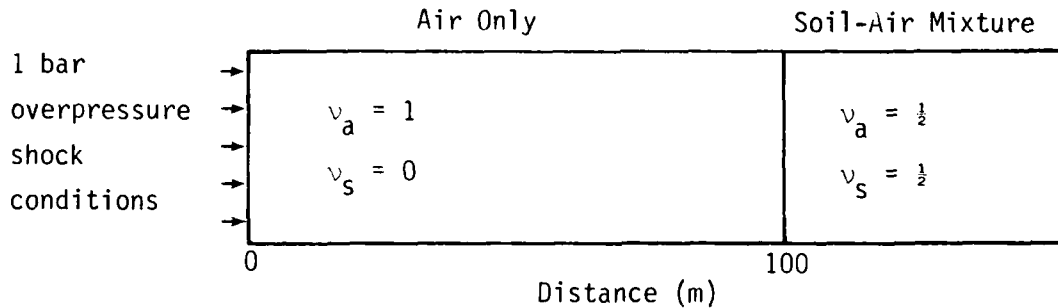
$$C^2 = \frac{\frac{\rho_a}{\rho_s} C_a^2}{\left(\frac{v_s \rho_a C_a^2}{\rho_s C_s^2} + v_a \right) \left(v_s + \frac{v_a \rho_a}{\rho_s} \right)}$$

Note that $\frac{\rho_a C_a^2}{\rho_s C_s^2} \sim 10^{-4}$ and $\frac{\rho_a}{\rho_s} \sim 10^{-3}$

$$\text{Thus, } C^2 \sim \frac{\rho_a C_a^2}{\rho_s v_s v_a} \quad (\text{rigid soil particles})$$

is good approximation until $v_a \rightarrow 0$ or $v_s \rightarrow 0$.

A test case was performed with the DICE code to approximately simulate the specialized condition just described and to verify the ability to calculate low wave speeds in two-phase mixtures. The problem configuration and soil/air volume fractions are indicated below:



A 1 bar overpressure shock wave travels through 100 m of air at STP in a simulated shock tube and then interacts with the soil/air mixture.

Figure 2.2 shows the overpressure versus distance profiles at three times prior to the shock wave interaction with the two-phase mixture. Figure 2.3 shows the overpressure profiles at four times after the shock wave begins interacting with the soil/air. Figure 2.4 is the related shock speed versus time curve. The shock wave in the air propagates at ~463 m/s; when the initial shock reaches the relative dense soil/air mixture ($\rho = 1 \text{ gm/cm}^3$) at $x = 100 \text{ m}$, a reflected shock wave travels back into the air with a reflection factor of ~2.6.

The shock wave speed in the two-phase mixture is ~28 m/s or about 6% of the air shock wave speed.

CALIFORNIA RESEARCH AND TECHNOLOGY, INC.
DICE 1-0 TWO PHASE SOUND SPEED TEST
OVERPRESSURE VS. DISTANCE

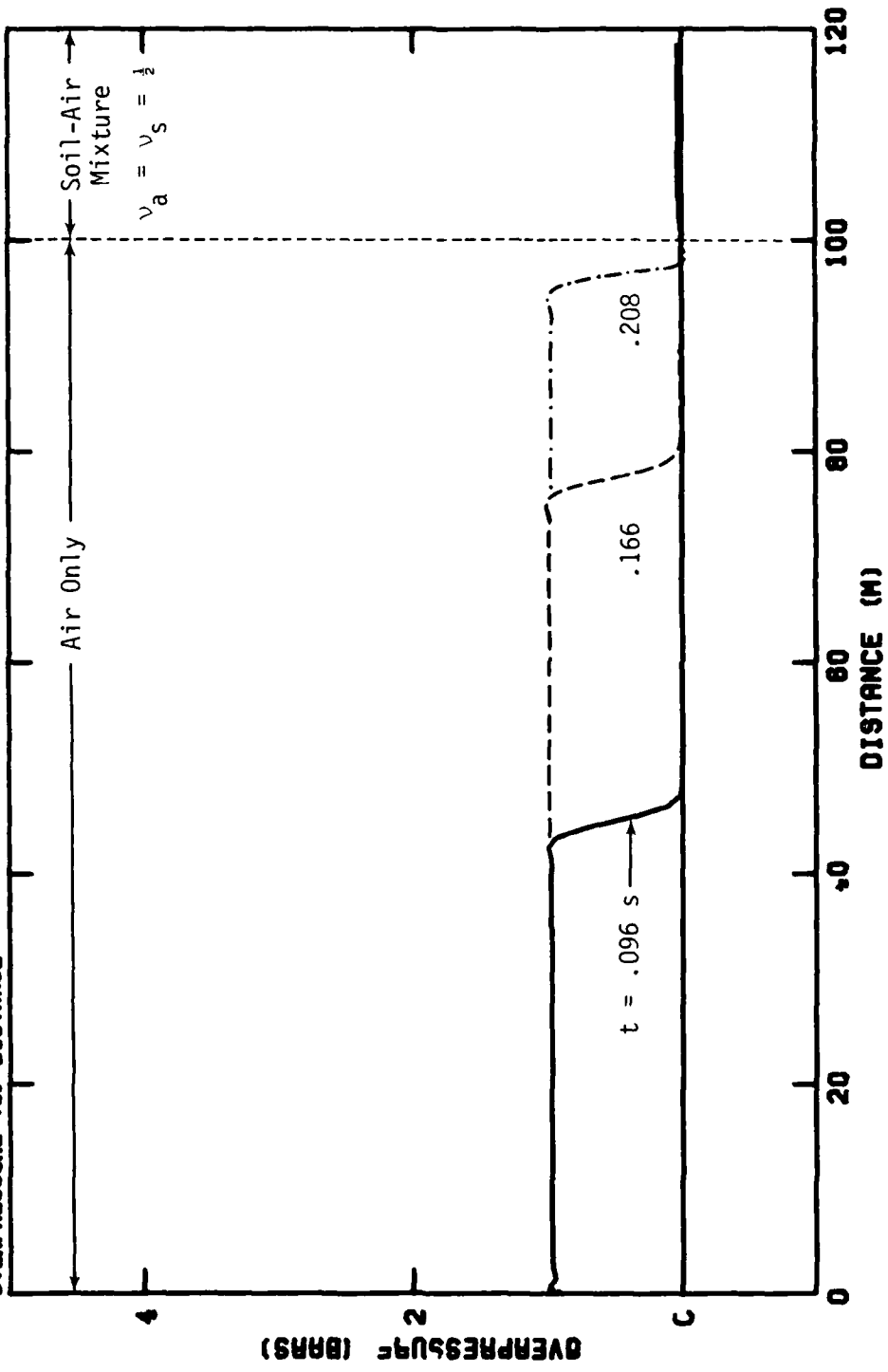


Figure 2.2. Overpressure Versus Distance Profiles at $t = .096$, $.166$ and $.208$ Seconds for Shock Tube Test Case.

CALIFORNIA RESEARCH AND TECHNICAL, INC.
DICE 1-0 TWO PHASE SOUND SPEED TEST
OVERPRESSURE V.S. DISTANCE

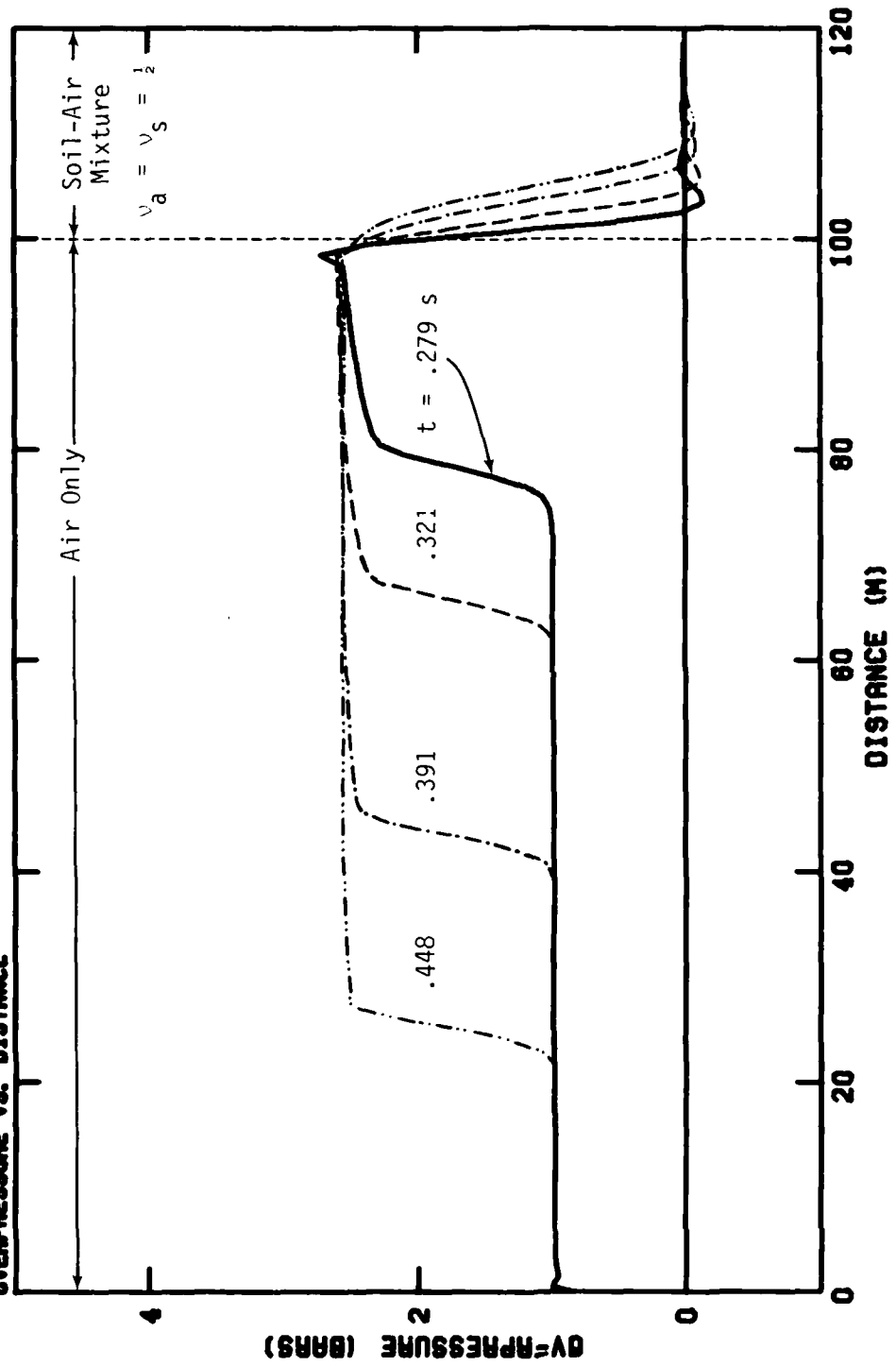


Figure 2.3. Overpressure Versus Distance Profiles at $t = .279$, $.321$, $.391$ and $.448$ Seconds for Shock Tube Test Case.

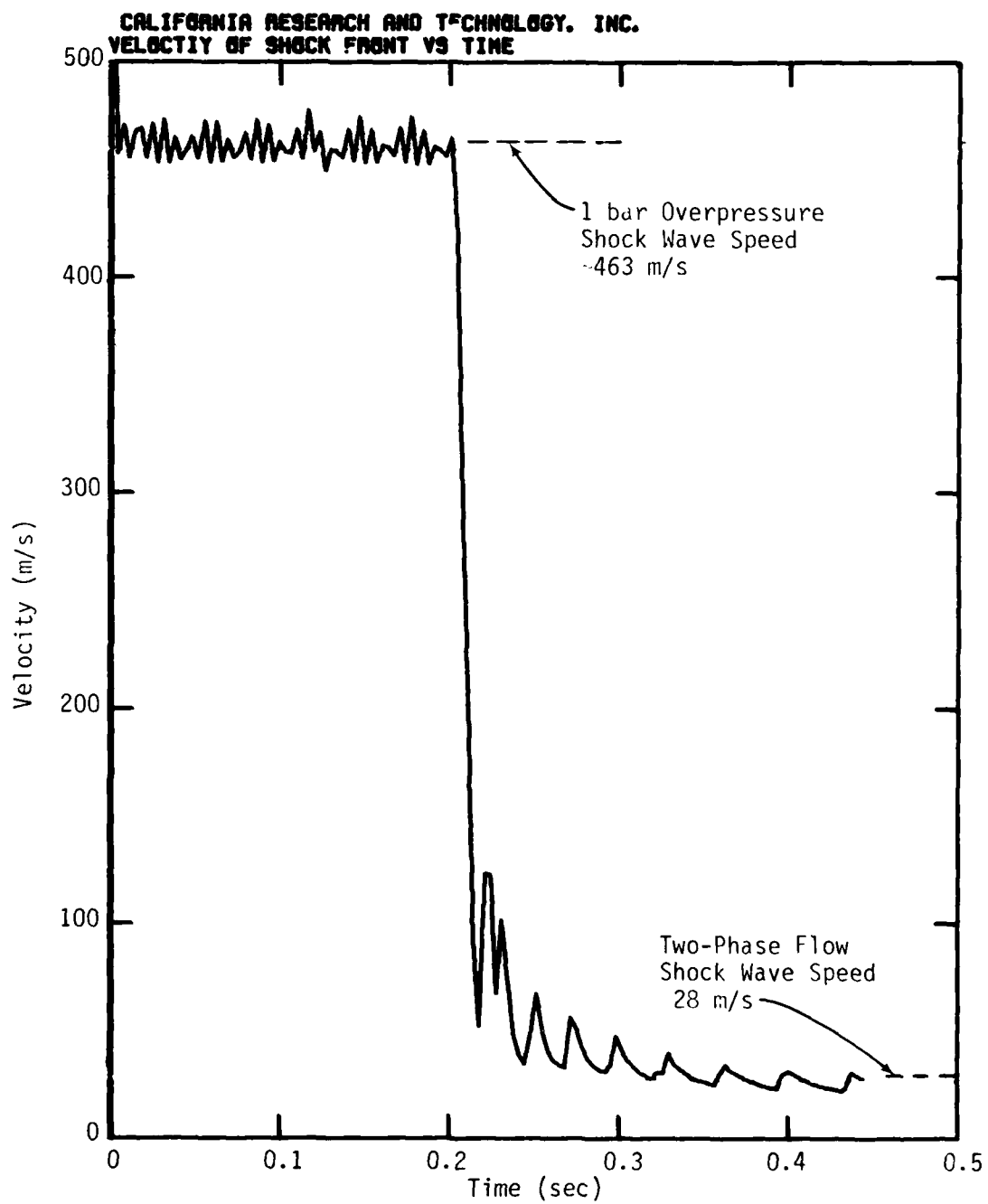
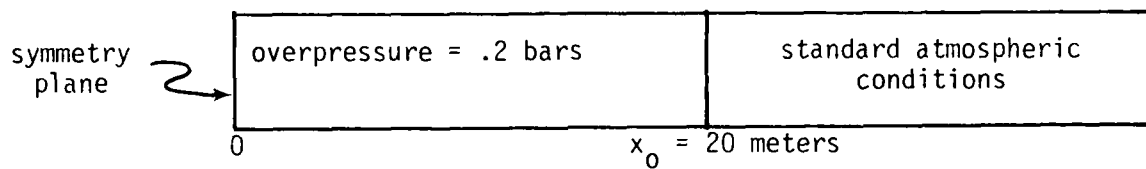


Figure 2.4. Shock Wave Speed Versus Time for Shock Tube Test Case.

2.5 AIR ONLY TEST CASE FOR WEAK SHOCK ($\Delta P = 0.1$ bar)

For some airblast problems of interest, the air overpressures are quite low. Therefore, a low overpressure test integration of the DICE code was performed to demonstrate that the code can calculate shocks and rarefaction waves correctly at overpressures of ~0.1 bar. The following sketch shows the initial pressure conditions used:



Initial "Shock Tube" Conditions

Initially, the air was at rest in both regions and is assumed to follow the ideal gas law ($\gamma = 1.4$). The zoning consisted of a uniform grid with one meter cells.

Analytical (closed form) solutions (see Ref. 10, pp. 181-191) can be obtained in 1-D by considering the equations governing the conservation of mass, momentum and energy plus the ideal gas equation of state for air. The results for the initial conditions considered are summarized in Figure 2.5. In this x-t diagram, the theoretical positions of the shock front, contact discontinuity and rarefaction fan are plotted as a function of time. The physical parameters describing the properties of each of the separate regions are also shown.

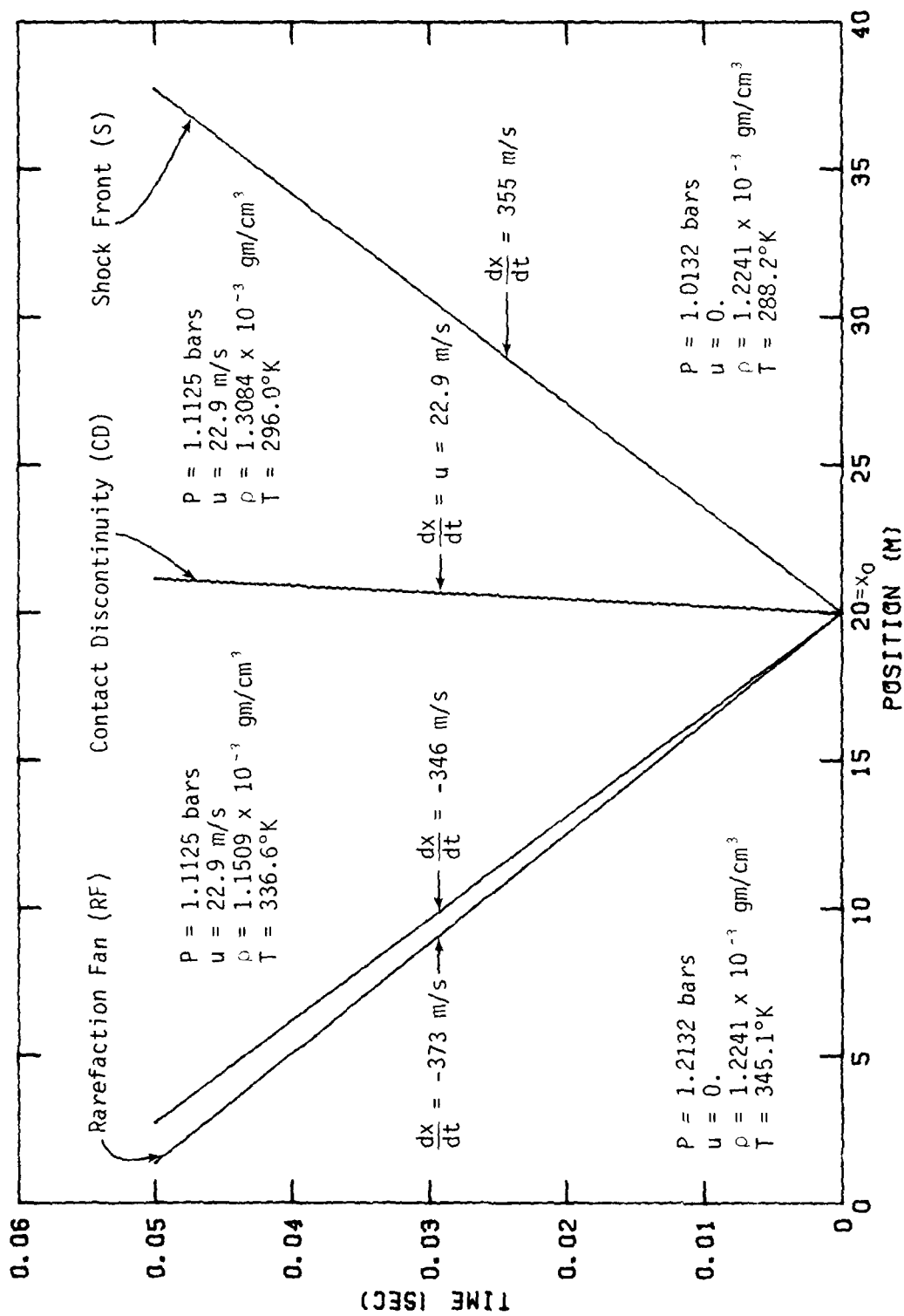


Figure 2.5. Theoretical Positions of Shock Front, Contact Discontinuity and Rarefaction Fan Versus Time for Low Overpressure Test Case.

DICE code integration results at .030 s, as well as the theoretical solution, are shown in Figures 2.6 through 2.9. Air overpressure versus distance is shown in Figure 2.6. A shock wave of 0.1 bar overpressure is seen to move forward into the undisturbed region, while rarefaction waves move backward into the initial overpressure region. These rarefaction waves comprise the rarefaction fan. For both the shock front and rarefaction fan, DICE is able to define the rapid variations with five cells. The shock pressure is matched almost exactly. Similar accurate results are seen for the discontinuities within the velocity, temperature and density profiles shown in Figures 2.7, 2.8 and 2.9, respectively. We conclude that DICE can handle shocks and rarefaction waves correctly for low overpressures at the 0.1 bar level.

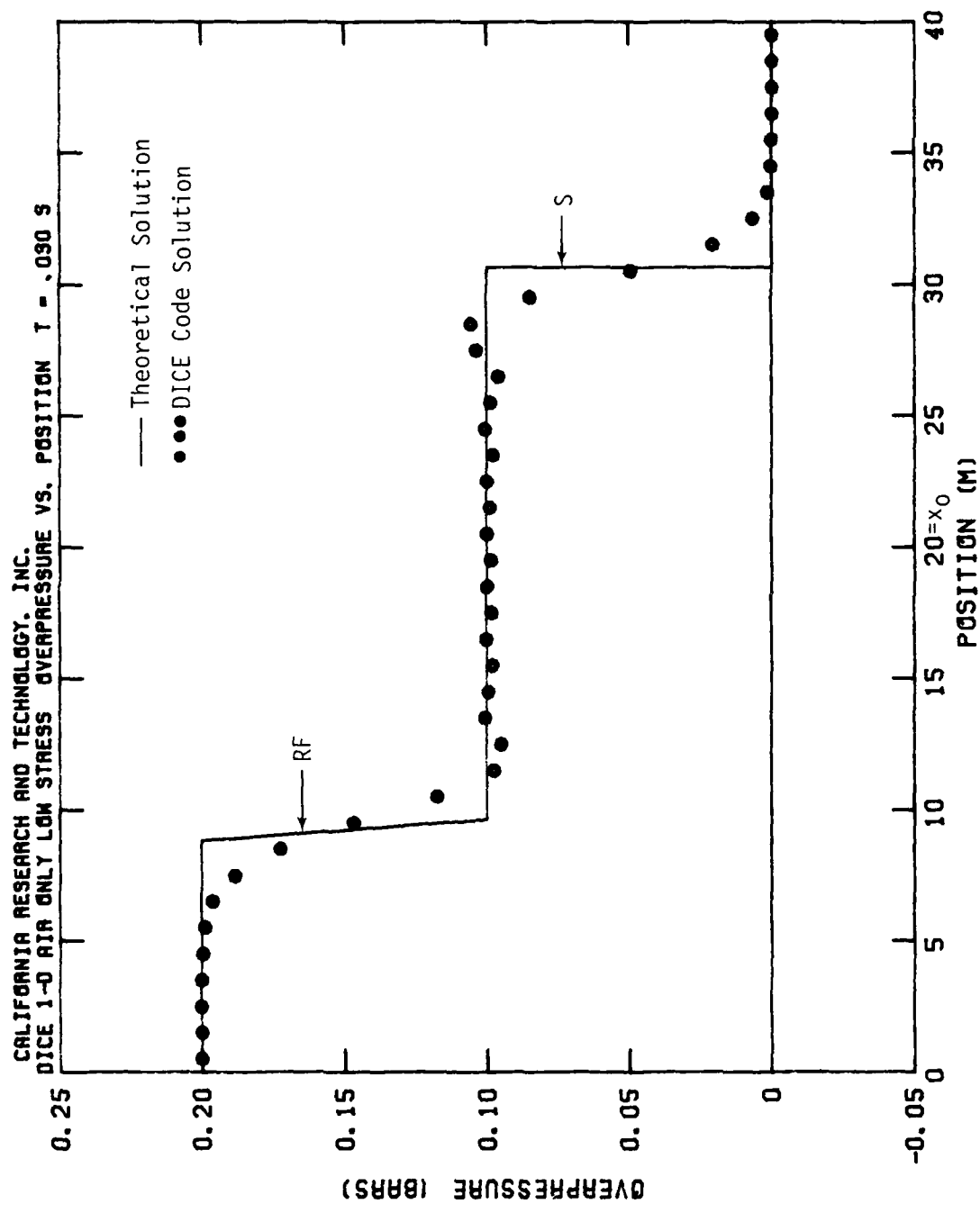


Figure 2.6. Air Overpressure Versus Position at $t = .030$ Seconds for Low Overpressure Test Case.

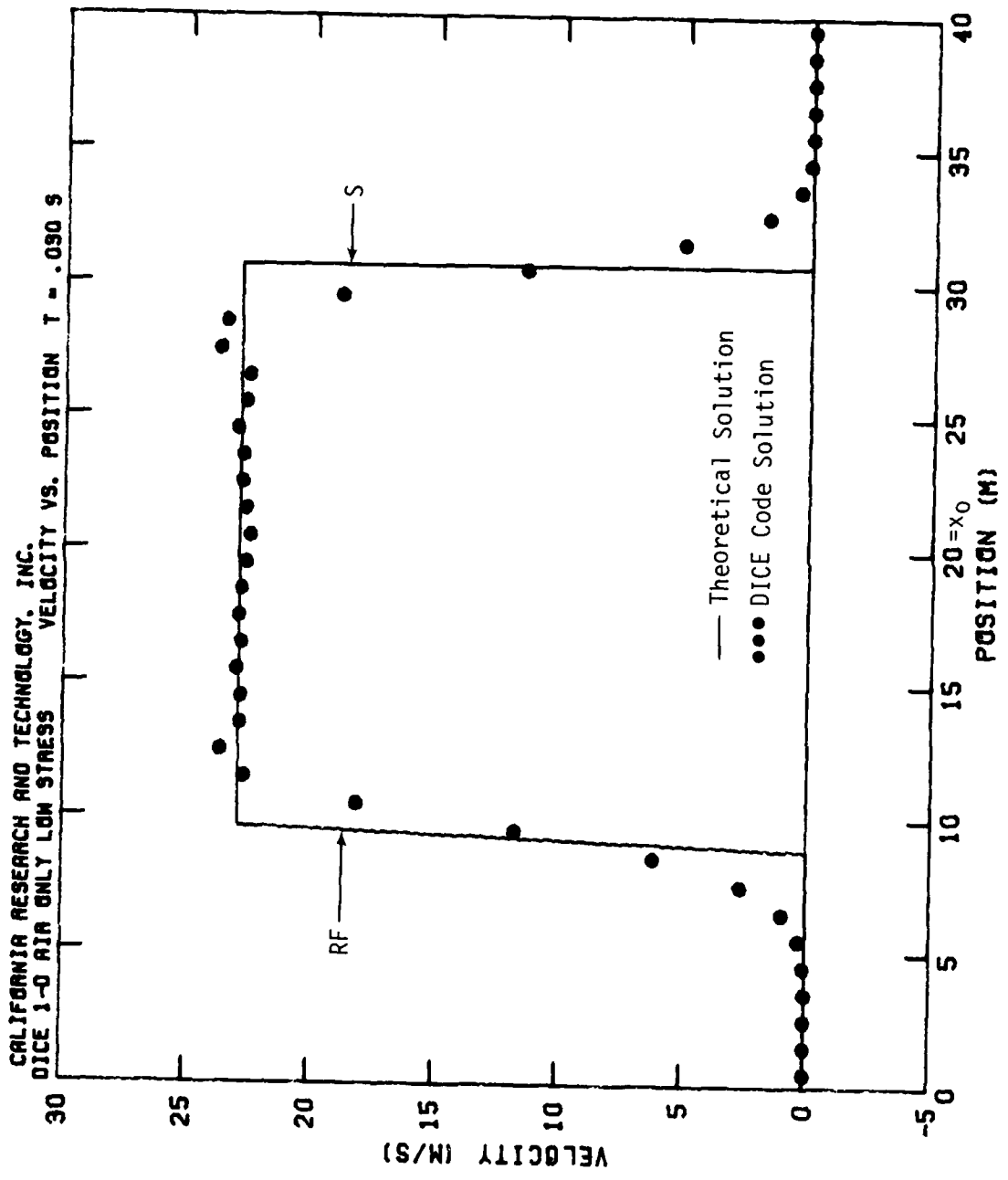


Figure 2.7. Air Particle Velocity Versus Position at $t = .030$ Seconds for Low Overpressure Test Case.

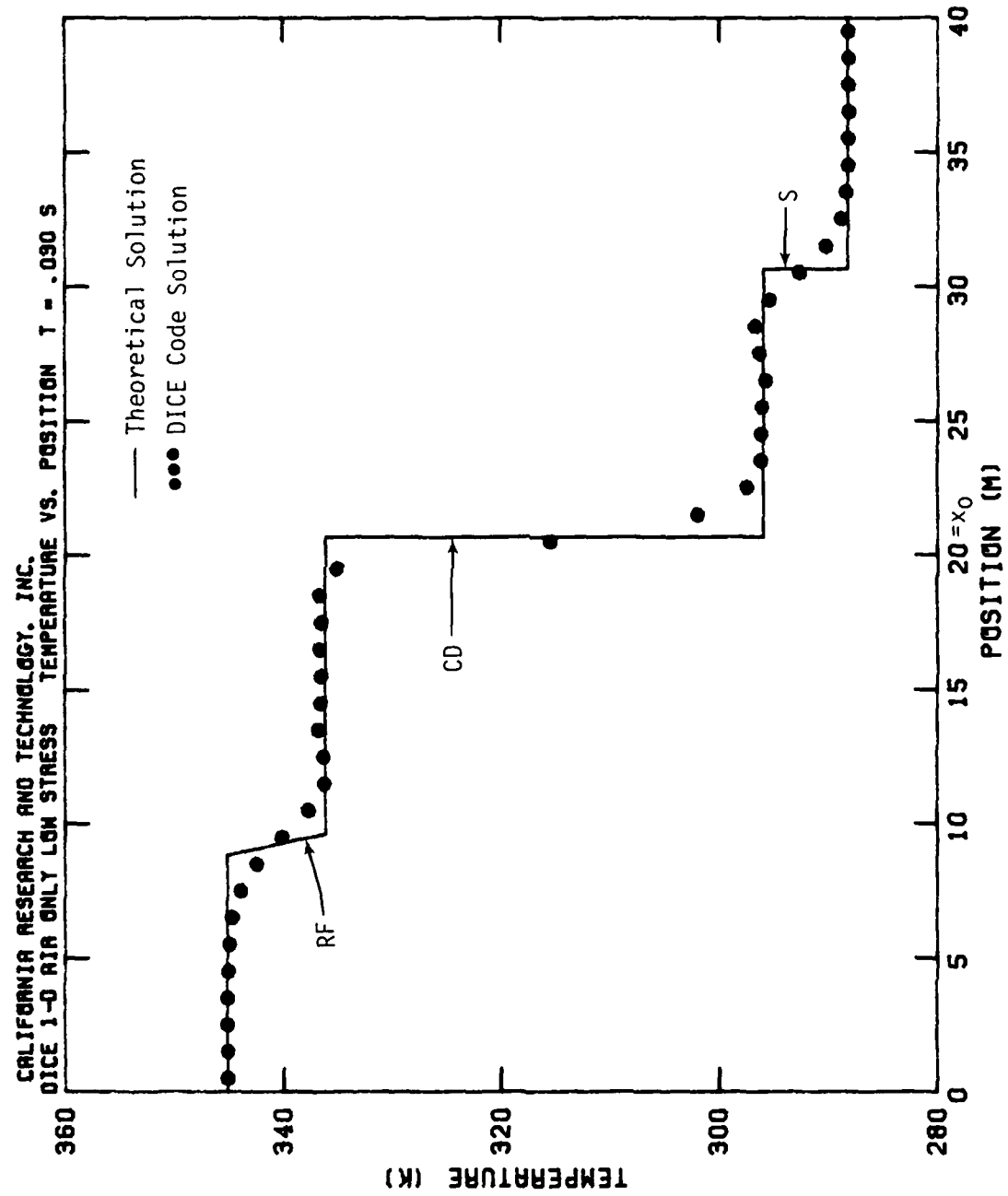


Figure 2.8. Air Temperature Versus Position at $t = .030$ Seconds for Low Overpressure Test Case.

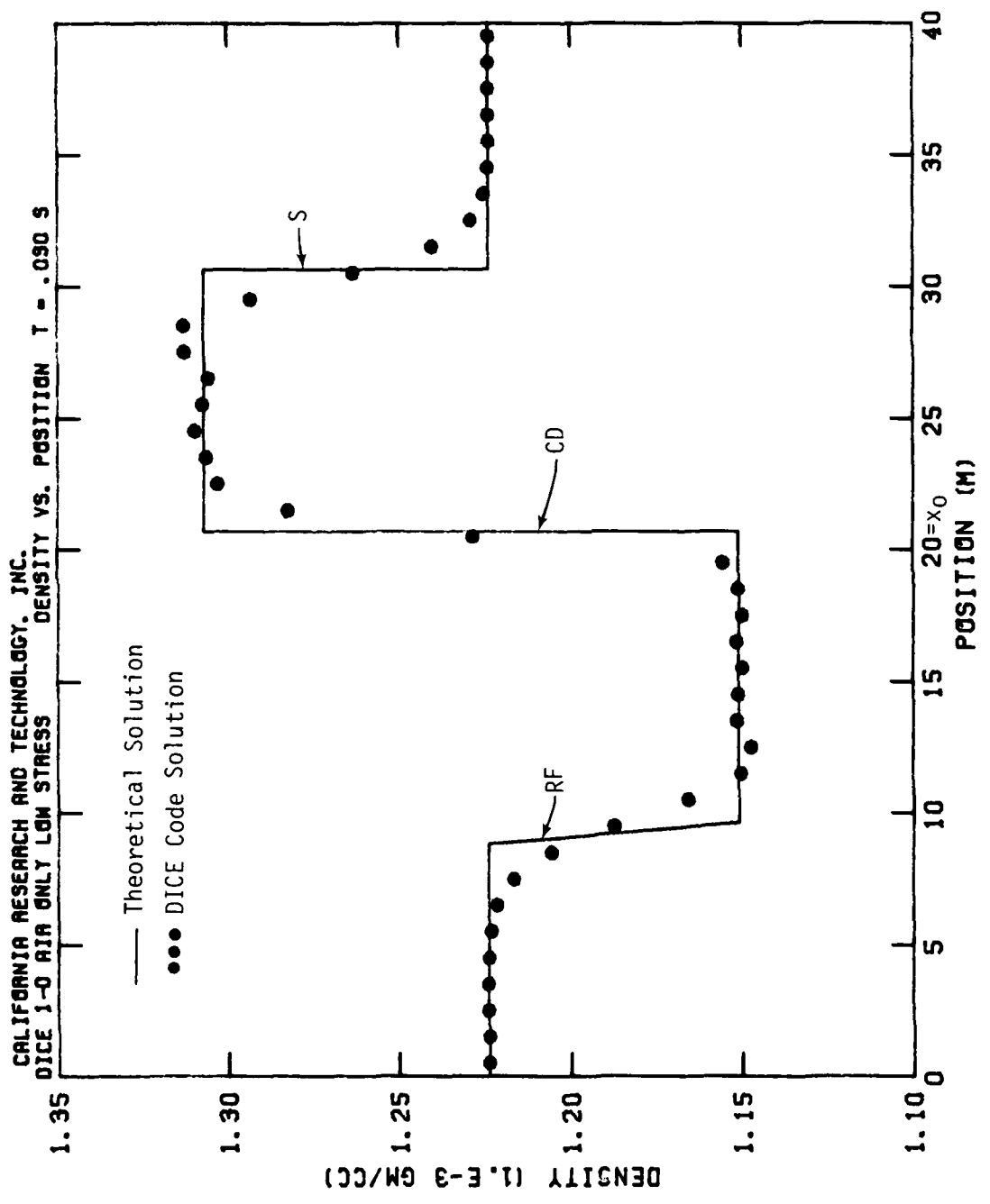


Figure 2.9. Air Density Versus Position at $t = .030$ Seconds for Low Overpressure Test Case.

SECTION 3

PORE-AIR PHENOMENA IN A SHOCK TUBE

3.1 LABORATORY EXPERIMENTS

Pore-air phenomena were studied by Zernow *et al.*³ in a series of laboratory experiments. The experiments involved the use of a shock tube (Figure 3.1) to load the surface of a column of sand with a known overpressure history. By breaking diaphragms 1 and 2 at appropriate times, the surface of the column of sand was exposed to air overpressure histories similar to the positive phase of the airblast at the 100 psi range from a 1 Mt nuclear burst. No negative phase was simulated. The motion of the sand column was observed photographically and pore-air pressure measurements were made at various depths in the sand.

Figure 3.2 shows the observed surface load overpressure time histories for the experiments conducted with a 8" diameter shock tube. Two orifice diameters were used to control the overpressure decay rate. The 1.78" diameter orifice yielded a faster decay rate with a shorter duration (~.450 s positive phase) compared to 1.36" diameter orifice with a positive phase of ~.750 s. Also shown in the figure is an overpressure time history described by a simple exponential decay function of the form

$$\Delta P_L = \Delta P_0 e^{-t/\tau} \quad (3.1)$$

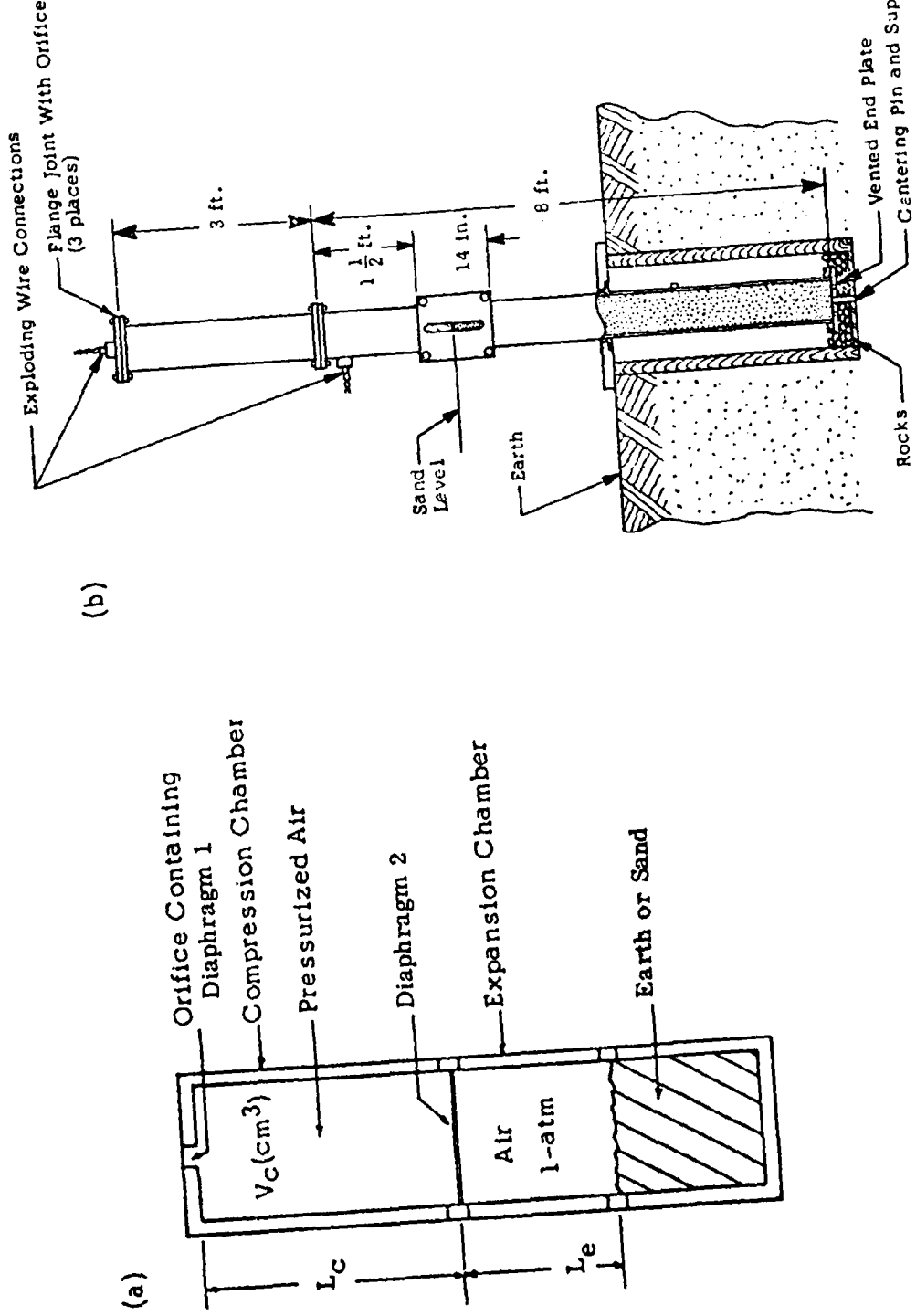


Figure 3.1. (a) Conceptual Design of a Shock Tube Utilizing Gas Flow Through an Orifice to Control Pressure-Time History on the Sand Surface, and (b) Schematic View of 8-Inch Vertical Shock Tube.

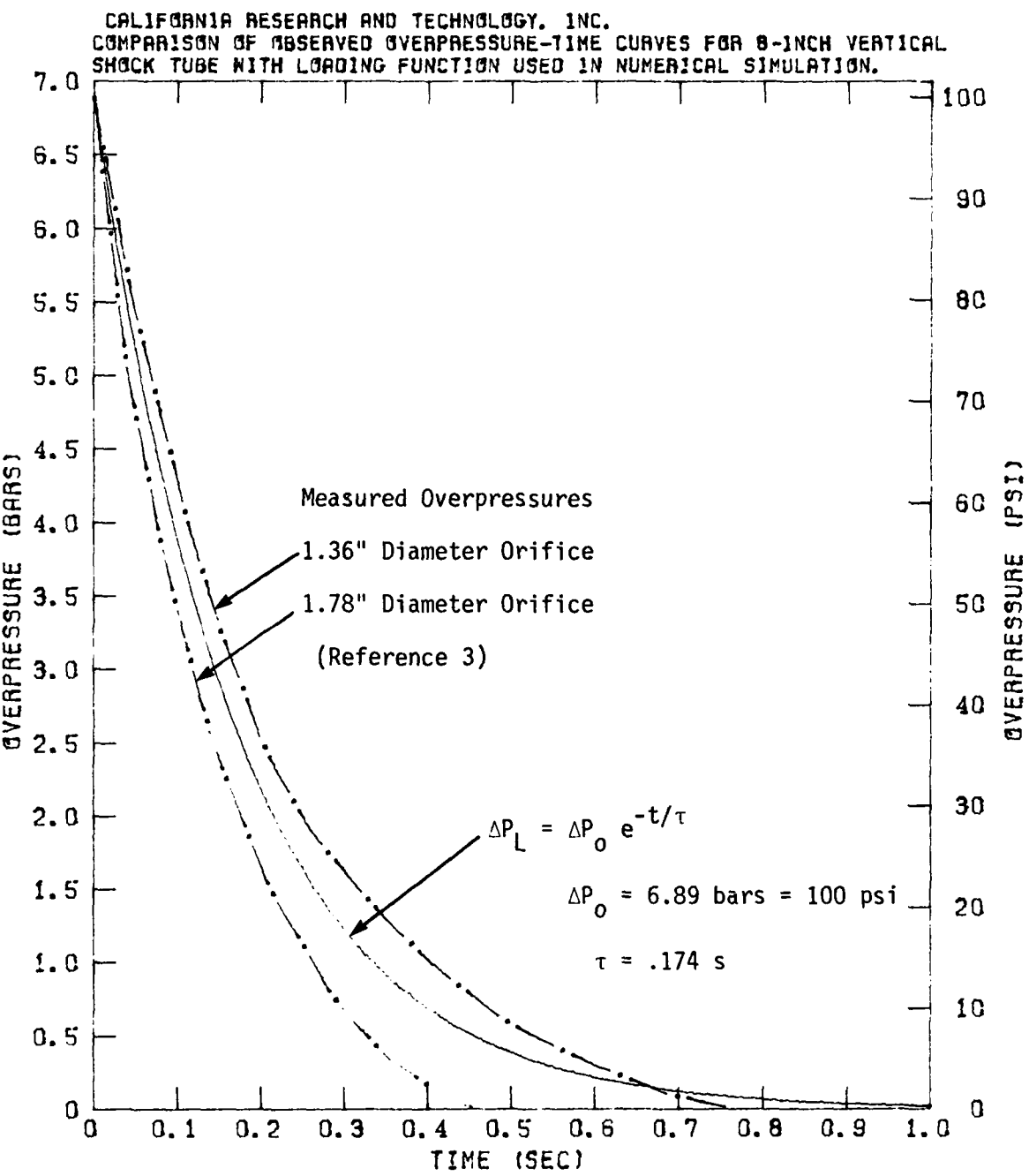


Figure 3.2. Overpressure Load to Surface of Sand Column Versus Time
 Observed in Experiments (Zernow *et al.*, 1973) and Fit
 Exponentially (used in DICE Cases 1 to 4 Calculations).

where

ΔP_L is the overpressure at time t

ΔP_o is the peak overpressure (at the shock front)

t is the elapsed time (after peak overpressure arrival)

τ is the decay parameter constant.

A value of 6.89 bars (100 psi) for ΔP_o and .174 s for τ results in an approximate fit to both of the experimentally observed time histories. This loading function is used in subsequent DICE code numerical simulations.

The average density of the standard sand used was found to be 1.60 gm/cm³. The estimated grain density of 2.40 gm/cm³ corresponds to a porosity (or air void ratio) of 0.33. Figure 3.3 shows the particle size distribution (% by weight) for the standard sand; the mass mean diameter is ~650 μ . Some of the experiments were conducted with "coarse" sand with particle diameters greater than 841 μ sieved from the standard sand. The coarse sand had an average density of 1.55 gm/cm³ and porosity of 0.354.

The bulk compressibility modulus was determined to be 85,000 psi (~5860 bars), which implies a compression wave velocity of ~605 m/s. For the 6 ft sand column this means that the transit time for the initial shock to reach the bottom is .003 s.

Note that in the experiments, the bottom of the sand column (~6 ft) was restricted from moving downward. Ideally, the sand column should be "infinitely long" with respect to the physical

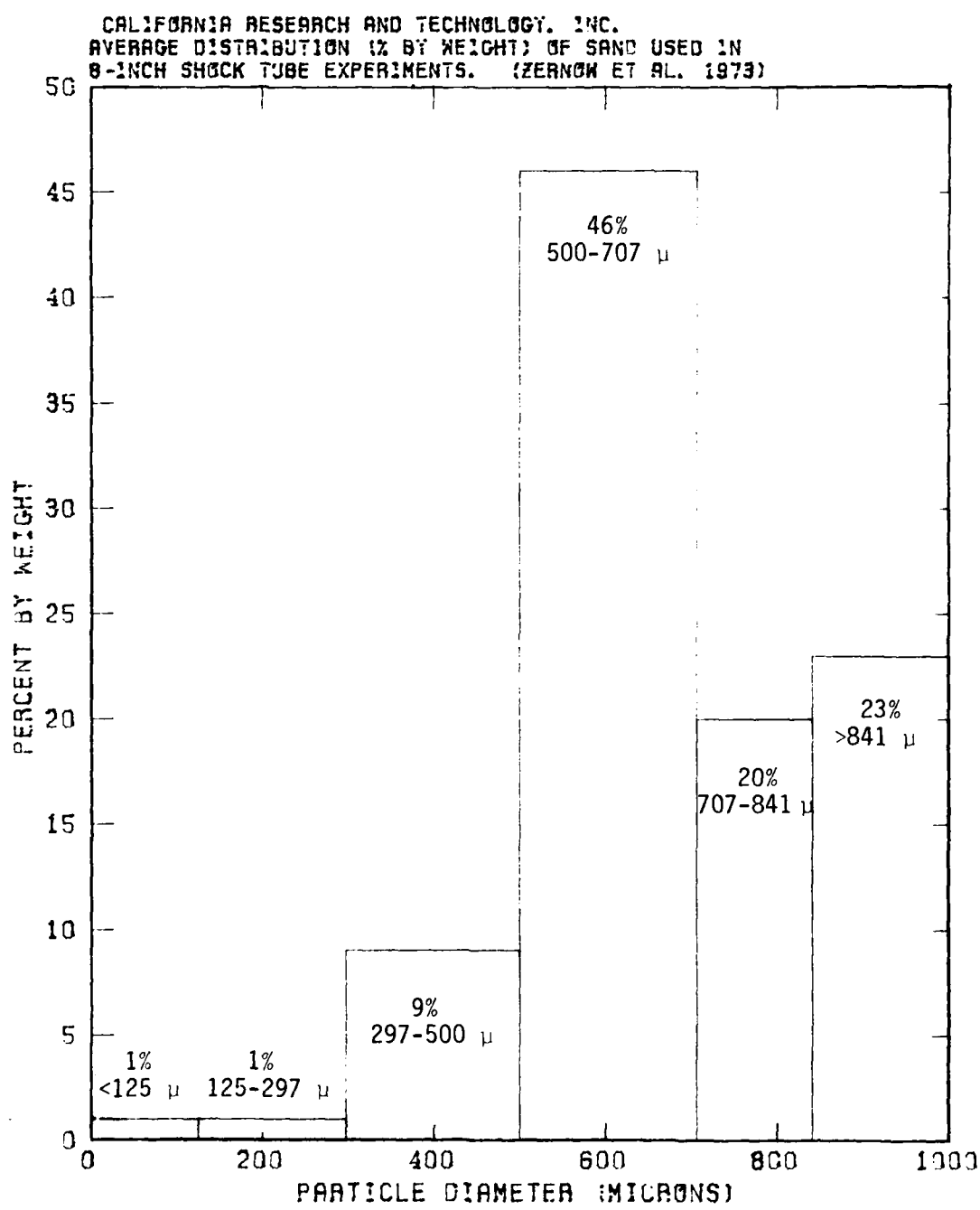


Figure 3.3. Average Distribution (% By Weight) of Standard Sand Used in 8" Diameter Shock Tube Experiments (Zernow et al., 1973).

effects which are being observed. In an ideal elastic material, the sand at a depth equivalent to the bottom of the sand column would behave similar to the sand near the surface. A pressure force applied to the sand surface would be felt 3 ms later at a 6 ft depth, and would eventually cause the entire sand column to translate downward. However, the rigid bottom in the experiments prevents this downward translation at the surface as well as at the bottom since the sand is essentially elastic. To simulate an infinitely long sand column with respect to pore-air phenomena, the bottom closure of the shock tube had small holes in it to allow restricted air flow. The intent was to approximate a permeability similar to that of the sand above the bottom closure.

Figure 3.4 shows the vertical displacement of the sand surface as a function of time from the 1.36" and 1.78" diameter orifice tests. The initial small displacements are considered to be a "precursor" sand cloud resulting from the shock tube induced "initial large amplitude reverberation oscillations in the very early portion of the shock pulse" affecting the top ~2 cm of the sand column. The main sand column starts to move upward at $t \sim .400$ s for the standard sand 1.36" tests and maintains a nearly constant velocity of ~43 cm/s for another .300 to .400 s. The 1.78" tests with faster overpressure decay rates resulted in the main sand column moving upward at an earlier time (~.200 s) and higher velocity (~77 cm/s). Both sets of curves for the standard sand experiments indicate that the maximum height attained by the lofted sand is nearly 20 cm. If the only force acting on a sand particle projected upward were gravity, the initial lofting velocity needed to reach 20 cm height is $V = \sqrt{2gH} \sim 200$ cm/s. Including air drag effects would increase the needed initial lofting velocity. The observed maximum velocity of 80 cm/s would

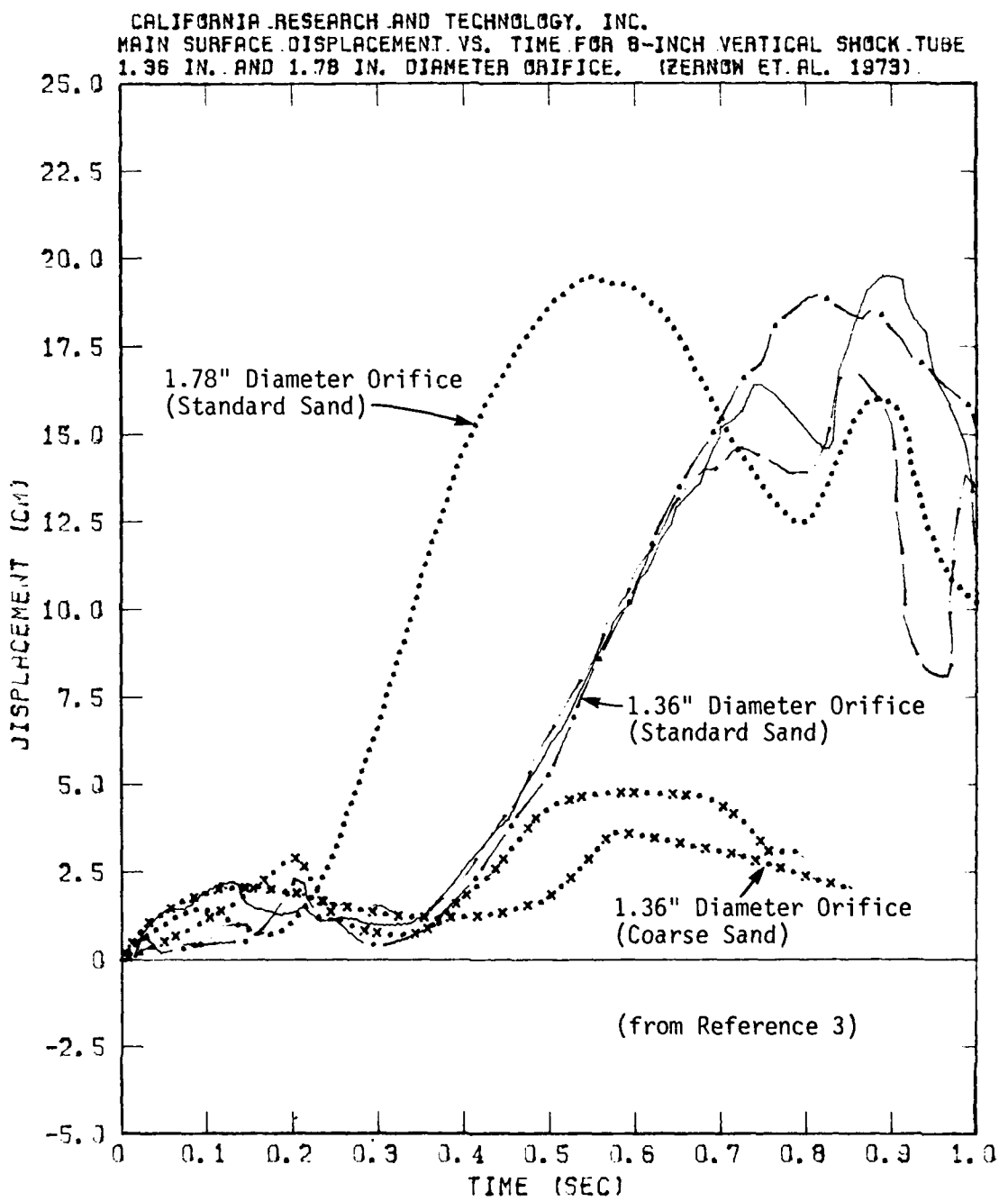


Figure 3.4. Main Surface Displacement Versus Time for 8" Diameter Shock Tube Experiments (Zernow et al., 1973).

project a sand particle less than 4 cm above the surface. Thus, the experimental evidence points to the sustained application of an additional upward force associated with pore-air phenomena.

Figure 3.4 also shows the main surface displacement for experiments run with the coarse sand (particle diameter $> 841 \mu$). The coarser sand particles yielded an increase in porosity and permeability. And although the same 1.36" diameter orifice pressure loading was used, there was a reduction in the main column motion by a factor of 4 both in velocity and displacement when compared to the standard sand cases. The coarse sand characteristics are very uncertain; a possible explanation is described in Section 3.3.

Figure 3.5 shows the position of the near-surface marked sand layers as a function of time for the 1.78" and 1.36" diameter orifice tests. Sustained upward motion is again seen for the sand below the surface to depths of approximately 10 to 15 cm.

Additional experiments involved saturating the standard sand 100% with water so that the porosity and permeability were essentially zero, and saturating the standard sand to 50% saturation level. The result was either total or near total elimination of main column motion.

3.2 NUMERICAL SIMULATIONS

Numerical simulations were performed with the multiphase DICE code in order to examine the pore-air phenomenology in a homogeneous porous soil. The calculations were designed using one-dimensional (1-D) planar geometry to approximate the

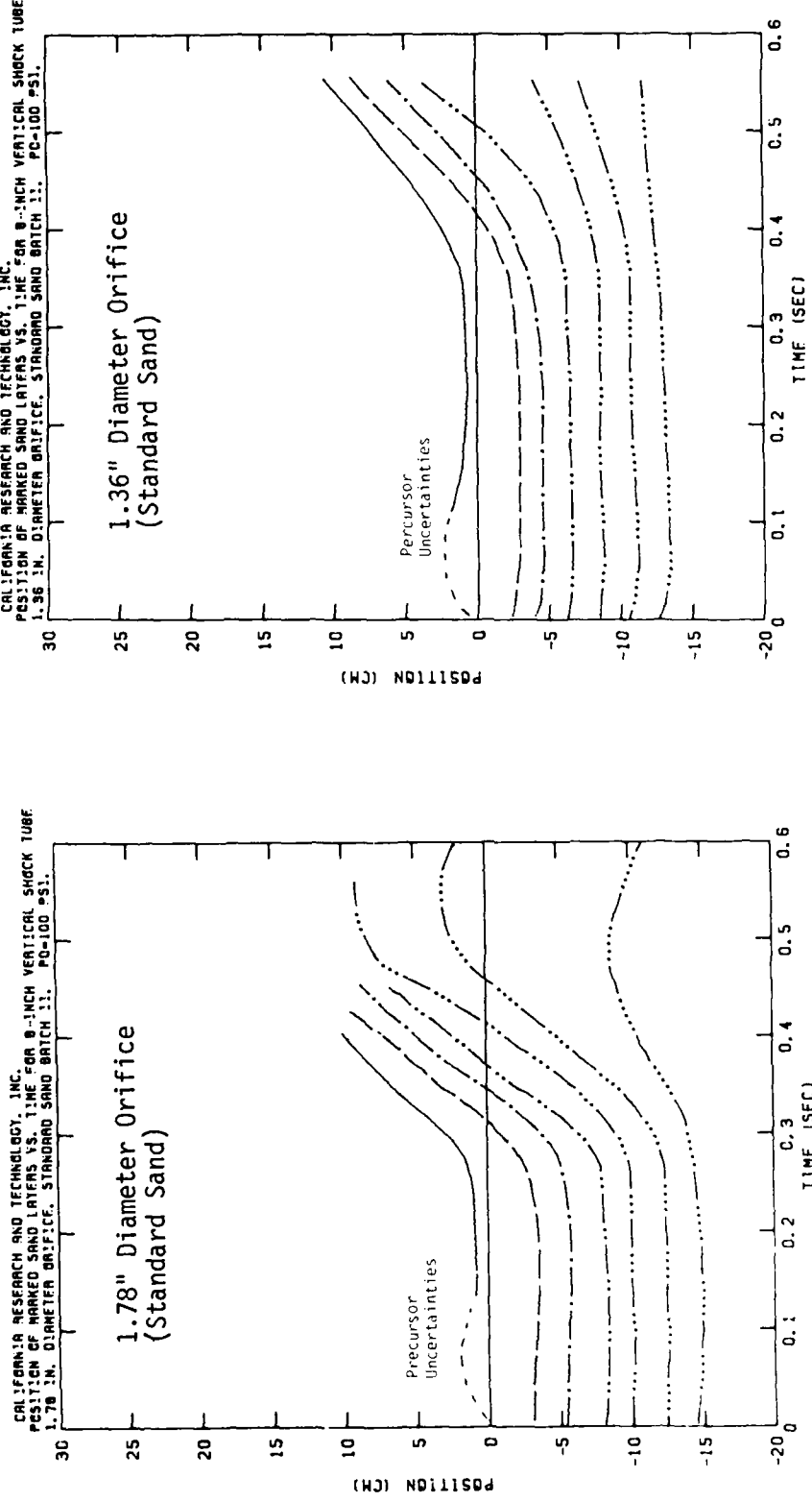


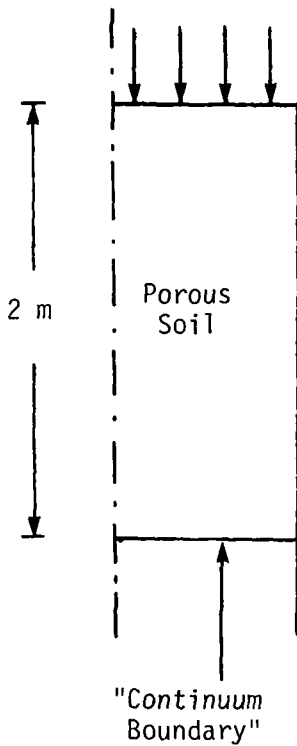
Figure 3.5. Position of Near-Surface Marked Sand Layers Versus Time Observed in Shock Tube Experiments (Zernow *et al.*, 1973).

laboratory shock tube experiments.³ The equations governing the relevant physics are discussed in Section 2.

Figure 3.6 defines the physical parameters used in DICE Cases 1 to 4. The overpressure loading function applied at the soil surface is the exponential fit shown in Figure 3.2, falling between the two overpressure time histories measured in the laboratory experiments. Its rate of decay is slower than for the 1.78" diameter orifice tests but faster than for the 1.36" tests.

The soil model parameters are taken from Reference 3. The initial soil density is 1.6 gm/cm³ with a porosity of $\nu_a = 0.33$. The soil is treated as a hydro-elastic material. The 605 m/s compression wave velocity implies a 3.3 ms transit time for the initial shock pulse at the surface to reach the bottom grid boundary. A semi-infinitely long column is modeled by imposing a continuum boundary at the grid bottom, allowing soil and air to flow past the bottom; note that in the laboratory experiments, the soil is rigidly constrained at the bottom of the shock tube.

In the calculation the soil is modeled using only one characteristic particle size. Case 1 uses a characteristic particle size diameter of $D_p = 0.1$ cm (all particles assumed to be uniform spheres), while Case 2 uses $D_p = 0.05$ cm. The permeability model described in Section 2.3 indicates that the permeability increases with porosity, and for a given porosity, the permeability varies as the square of the particle size. Thus, the permeability of the soil in Case 1 is four times larger than in Case 2 for a given porosity. Cases 1 and 2 include effects of a uniform gravitational field ($g = 980$ cm/s²).



Pressure Loading $\Delta P_L = \Delta P_0 e^{-t/\tau}$

$$\Delta P_0 = 6.89 \text{ bars} = 100 \text{ psi}$$

$$\tau = 174 \text{ ms} = .174 \text{ s}$$

Soil Model

$$\bar{\rho}_S = 1.6 \text{ gm/cm}^3$$

$$\rho_{OS} = 2.4 \text{ gm/cm}^3$$

$$v_a = 1 - \frac{\bar{\rho}_S}{\rho_{OS}} = .33$$

$$K = 5.86 \text{ kbars} = 85,000 \text{ psi}$$

$$C = 605 \text{ m/s}$$

$$\tau_T = 3.3 \text{ ms for a 2 meter transit}$$

| Case | Characteristic Particle Size D_p (cm) | Permeability k (Darcy)* | Gravity g (m/s^2) |
|------|---|------------------------------|----------------------------|
| 1 | 0.1 | 469 | 9.8 |
| 2 | 0.05 | 117 | 9.8 |
| 3 | 0.05 | 117 | 0.0 |
| 4 | 0.1422 | 948 | 0.0 |

*1 Darcy = $9.87 \times 10^{-9} \text{ cm}^2$

Figure 3.6. Pressure Loading and Soil Parameters for 1-D Shock Tube Calculations (Cases 1 to 4).

Cases 2 and 3 compare the effect of gravity on the pore-air lofting process. $D_p = 0.05$ cm for each case; but in Case 3, zero gravity is assumed. Case 4, which also has zero gravity, has a factor of ~3 increase in particle size and a factor of ~8 increase in permeability from Case 3.

Figure 3.7 shows the 1-D grid used in the calculations. The surface soil cell is 2 cm, with each subsequent cell 10% larger than the cell above it. All cells above the original surface ($z = 0$) are of uniform size (2 cm).

3.2.1 Case 1 ($D_p = 0.1$ cm, $g = 980$ cm/s²)

Figure 3.8 shows the initial pressure distribution versus depth for soil and air for Case 1. The total stress shown is the sum of the pressure due to the pore air and the effective stress contribution from the soil. The initial air pressure was taken to be 1.013 bars (= 1 atm) throughout the soil column depth. The initial lithostatic pressure at depth in the soil column is the pressure required to support the weight of the total amount of soil above that depth. It increases essentially linearly from zero at the surface to a value of 0.314 bars at a depth of 200 cm.

Figure 3.9 shows the pressure and velocity distributions for soil and air at $t = .001$ s after the initial application of the pressure loading function at the soil surface. The soil compression wave velocity of 605 m/s implies a transit distance of 60 cm by this time for the initial pressure loading impulse. First principle shock theory for an elastic medium yields a soil particle velocity of 71 cm/s behind the shock front for an initial pressure of 6.89 bars. DICE gives good agreement with

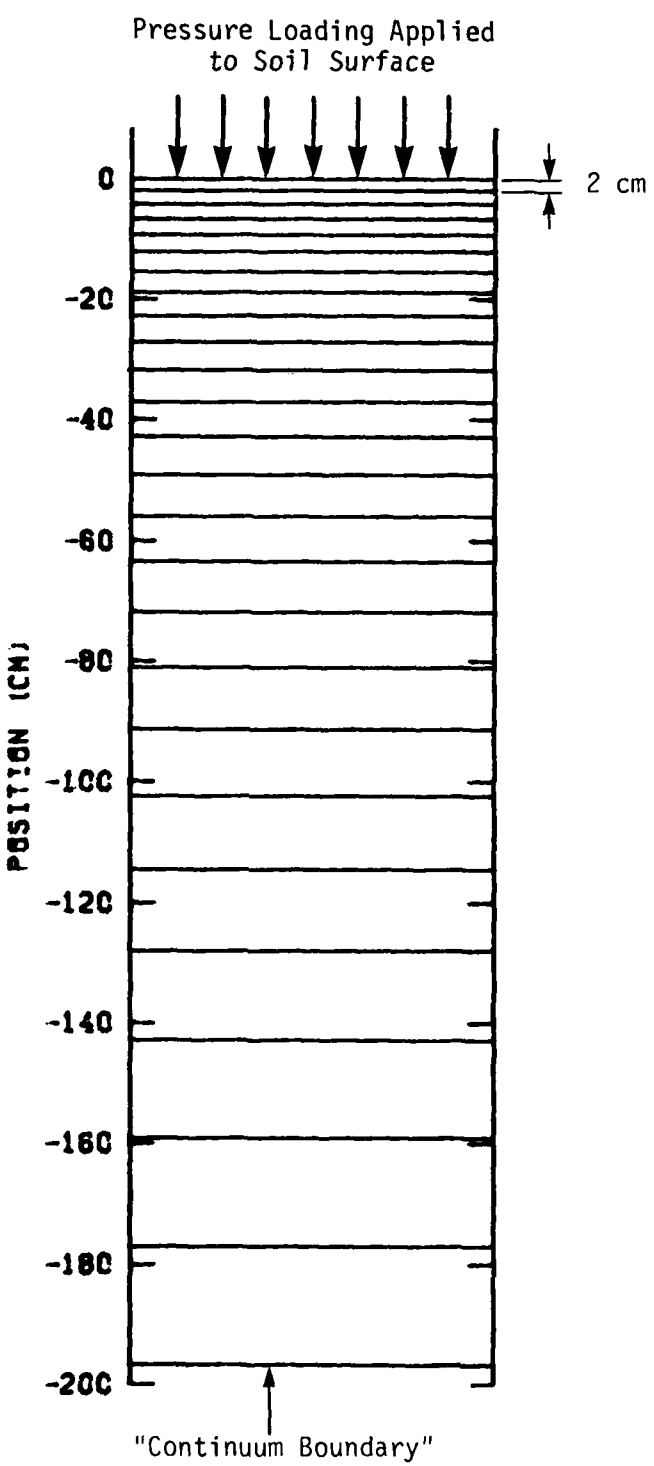


Figure 3.7. Grid Used for DICE 1-D Shock Tube Calculations, Cases 1 to 4.

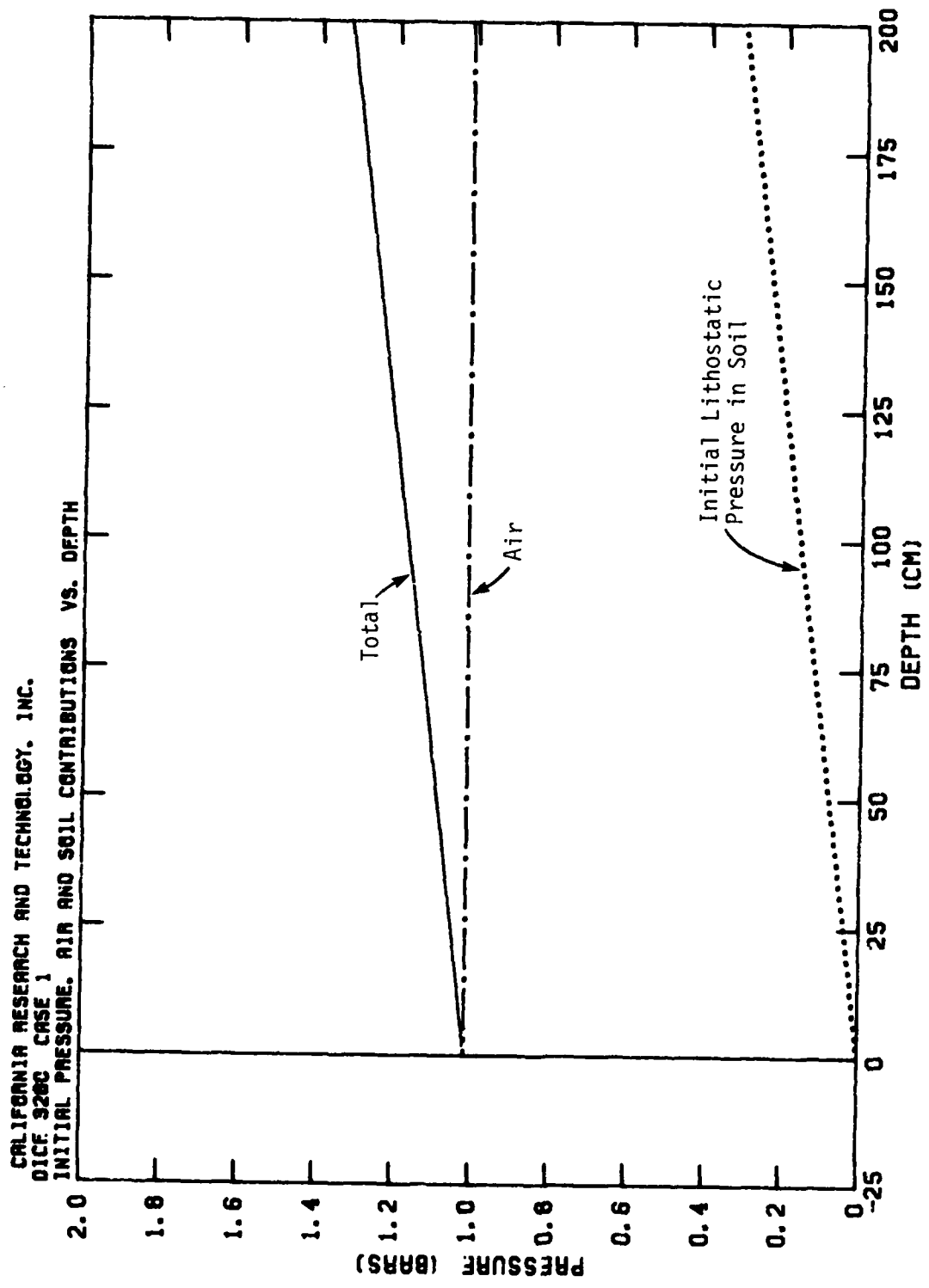


Figure 3.8. Initial Soil, Air and Total Stress Versus Depth for Case 1
($D_p = 0.1$ cm).

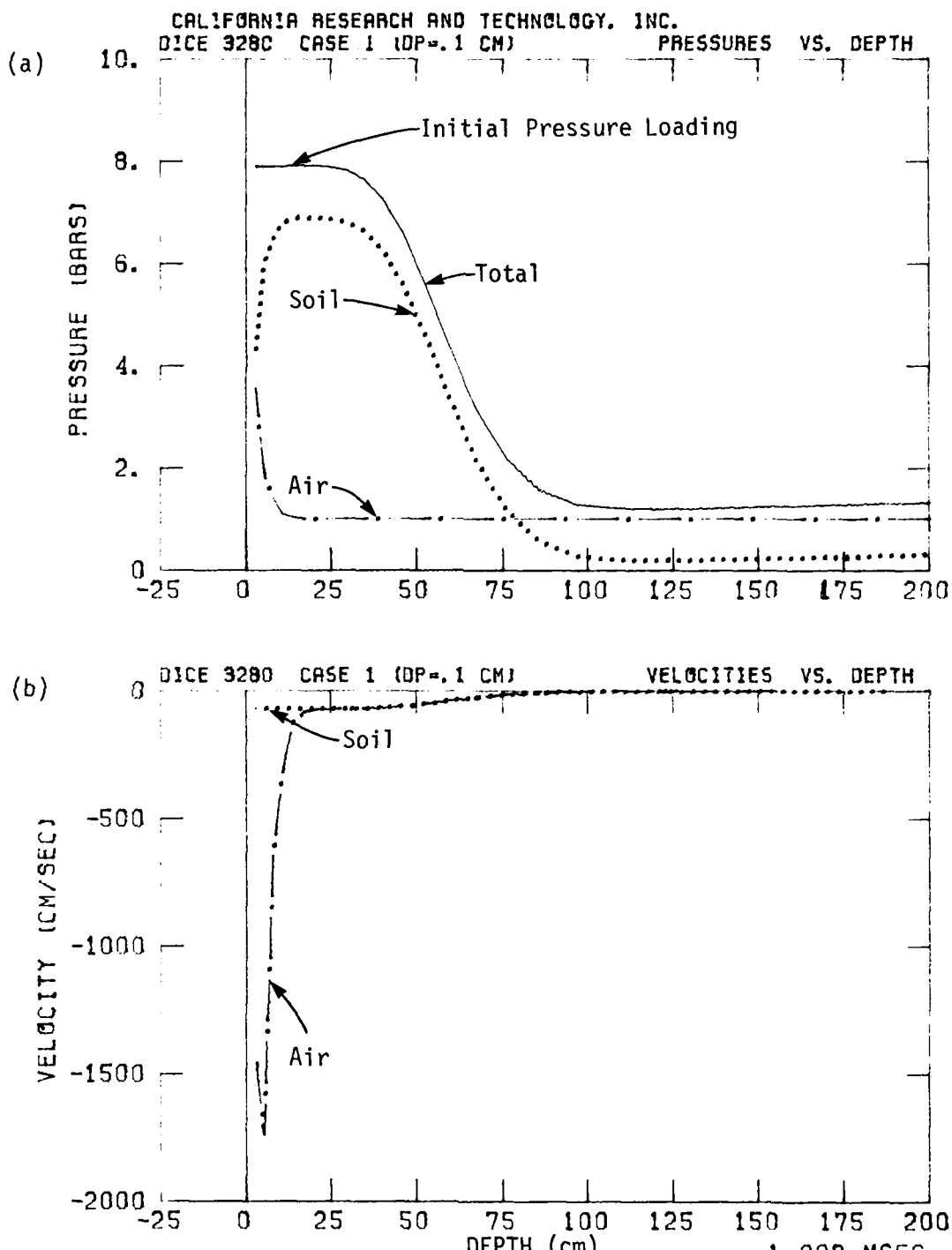


Figure 3.9. (a) Soil, Air and Total Stress Versus Depth, and
(b) Soil and Air Velocity Versus Depth at
 $t = .001$ Seconds for Case 1 ($D_p = 0.1$ cm).

these theoretical values. The pressure loading shock front is seen to travel to the theoretical depth (the numerically smeared transition region across the shock front is centered at ~60 cm); the downward soil velocity behind the front is approximately 70 cm/s.

At $t = .001$ s, the soil is supporting all of the overpressure load except near the surface, where air traveling down at over 1500 cm/s has begun to permeate into the soil. As the air is forced down into the soil matrix, the pore air density and thus pore air pressure increases and the air supports a portion of the pressure load.

Figure 3.10 shows that by $t = .050$ s the pressure loading of the soil surface has affected the entire column. Below 100 cm the entire overpressure load is supported by the soil (the air is still at its initial value). Above this depth the pore air pressure increases nearly linearly to the surface. At the surface the pressure load is supported almost entirely by the air. At the surface the air is flowing down through the soil at ~200 cm/s. The peak downward air velocity of nearly 350 cm/s is at a depth of ~50 cm. Below 100 cm the soil and air matrix move downward at a velocity 54 cm/s consistent with the theoretical velocity behind a shock front of overpressure $\Delta P_L(t = .050) = 6.89e^{-t/.174} = 5.17$ bars.

The total pressure at any time will still contain the initial air and soil contributions discussed previously (see Figure 3.8). In addition, because of the decay in time of the overpressure loading function, there is a net overpressure differential from the surface to any depth, due to the transit time (at sound speed velocity C) required for information (the

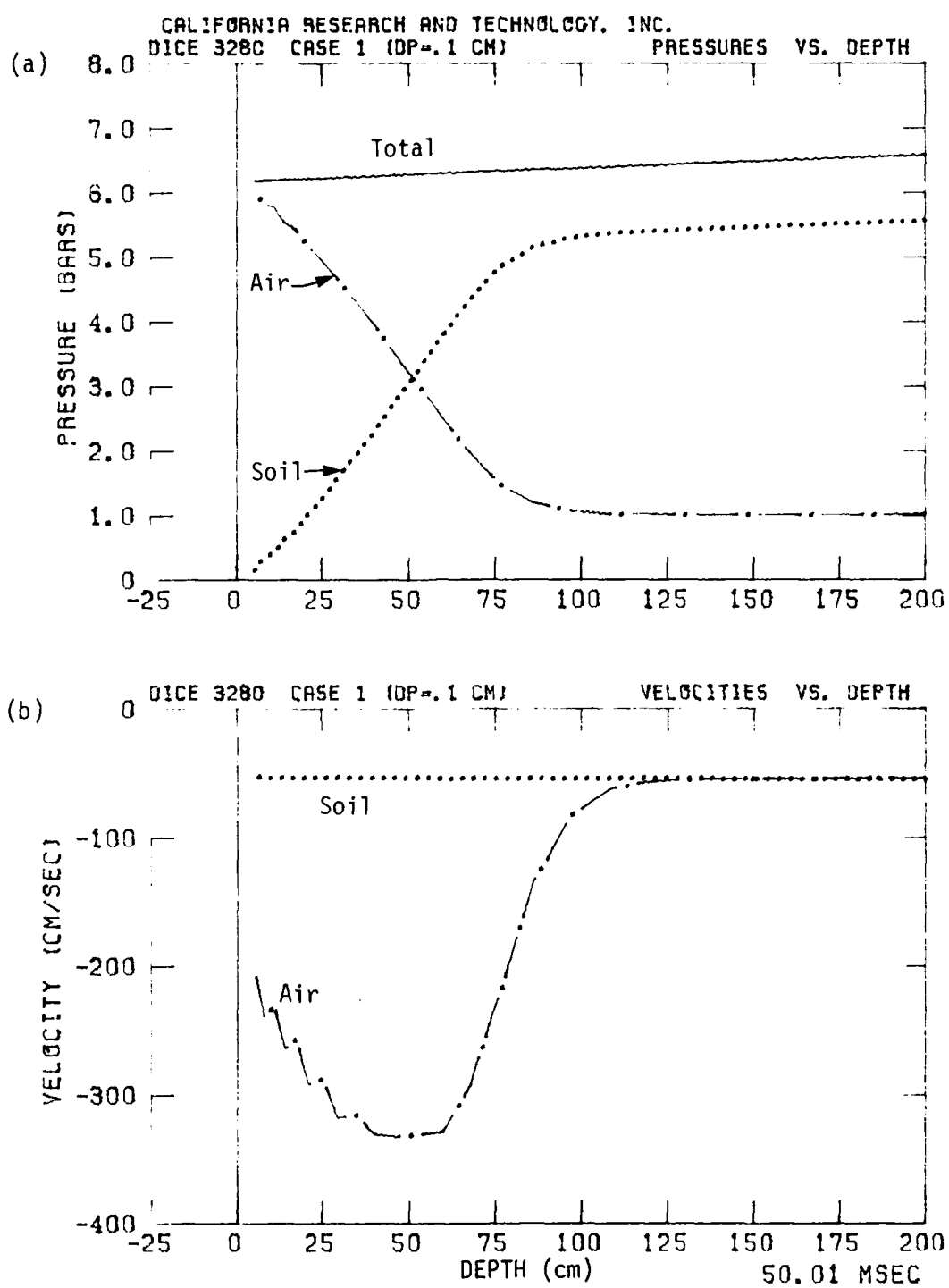


Figure 3.10. (a) Soil, Air and Total Stress Versus Depth, and
 (b) Soil and Air Velocity Versus Depth at
 $t = .050$ Seconds for Case 1 ($D_p = 0.1$ cm).

pressure load) from the surface to get to that depth. The theoretical overpressure at depth z and time t due to the loading function is thus $\Delta P(z,t) = 6.89e^{-(t-z/C)/.174}$ bars. The overpressure differential Δp from the surface to depth z (as a function of time) is thus

$$\Delta p(z,t) = 6.89e^{-t/.174} [e^{z/C/.174} - 1] \text{ bars.} \quad (3.2)$$

It is this net overpressure differential which provides the upward force which accelerates the soil and/or air upward, thus decreasing its downward velocity. Note the exponential decay in time which will result in weaker upward forces.

Figure 3.11 shows that by $t = .100$ s the air has begun to flow through the soil at a depth of over 150 cm, with the peak downward velocity of ~ 200 cm/s at ~ 80 cm depth. More significantly, by $t = .100$ s the air is supporting the entire pressure load at the surface. The soil particles become fluidized; they are no longer able to support any loads. The soil particle motion in a fluidized state is dominated by gravity and internal drag/permeability interactions with the air.

Figure 3.12 shows that at $t = .200$ s the soil is fluidized to a depth of ~ 40 cm and a pressure gradient causing upward accelerations exists in this near-surface region. Much lower sound speeds in the fluidized soil as compared to the unfluidized soil (see Section 2.4) will result in larger upward pressure forces as indicated by Equation (3.2). And because the air density is about three orders of magnitude less than the soil density, there is a larger increase in upward acceleration of the air as compared to the soil particles. The results of this are

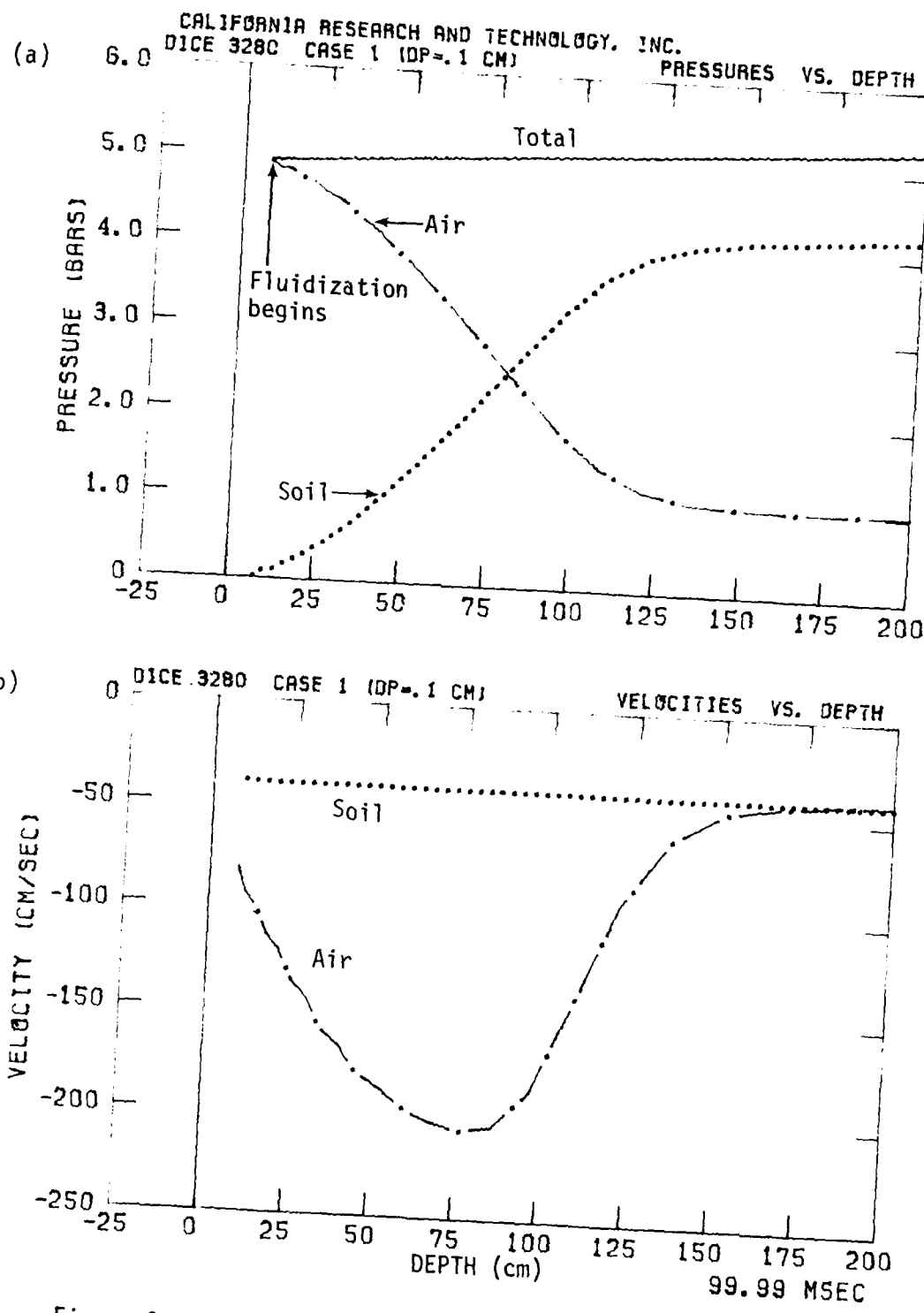


Figure 3.11. (a) Soil, Air and Total Stress Versus Depth, and
 (b) Soil and Air Velocity Versus Depth at
 $t = .100$ Seconds for Case 1 ($D_p = 0.1$ cm).

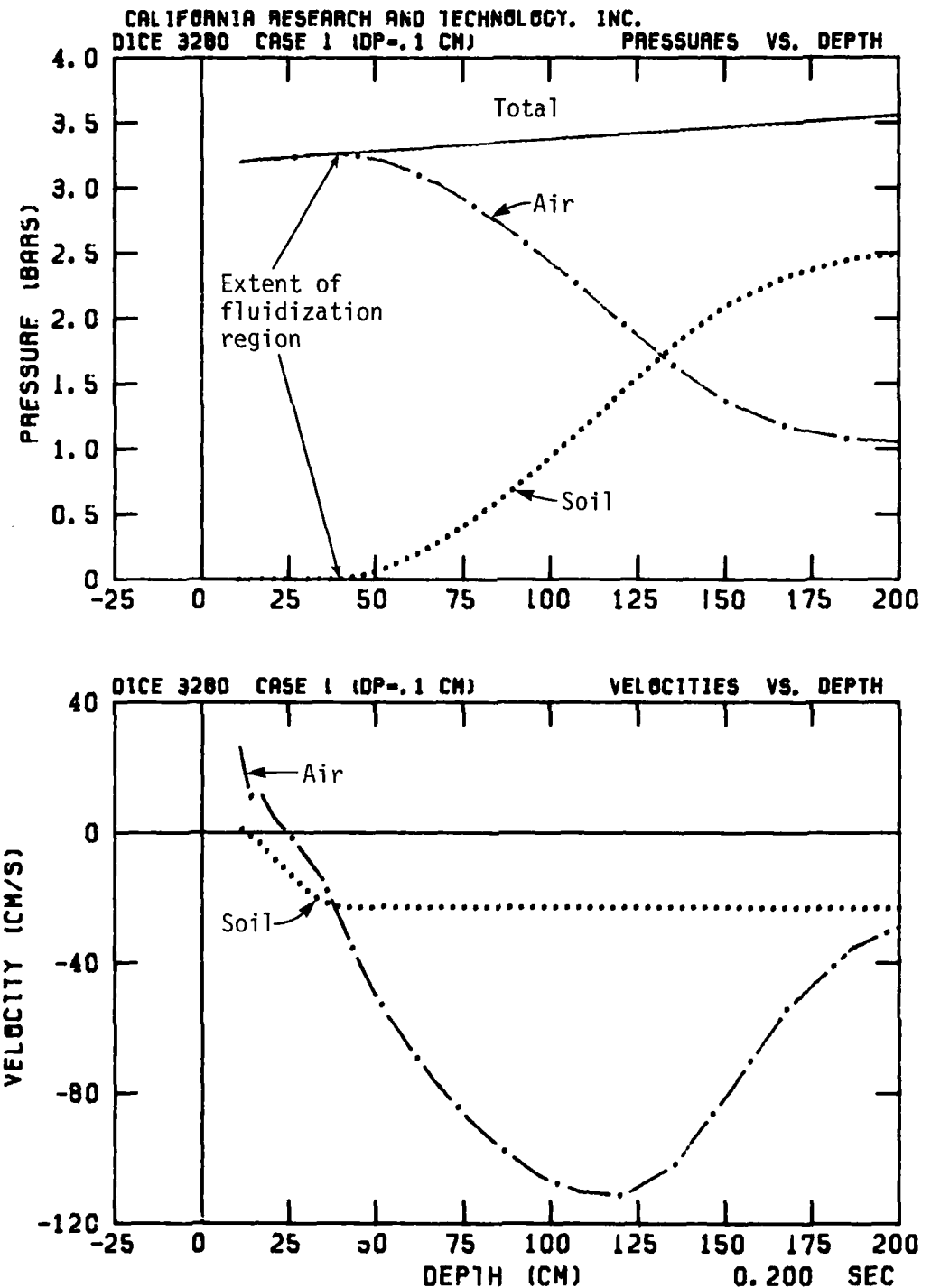


Figure 3.12. (a) Soil, Air and Total Stress Versus Depth, and
 (b) Soil and Air Velocity Versus Depth at
 $t = .200$ Seconds for Case 1 ($D_p = 0.1$ cm).

seen in the velocity profiles in Figure 3.12. The air in the fluidized region is moving upward relative to the soil. Internal force interactions with the soil particles is providing a deceleration of the air, while causing the soil particles to accelerate upward; the soil in the fluidized region is in fact moving upward relative to the remainder of the soil column.

Figure 3.13 shows that by $t = .400$ s the region of fluidization extends to ~ 115 cm depth. The soil column above 100 cm depth is moving upward, with a maximum velocity of 67 cm/s at the surface. The upward air velocity is also largest at the surface, with a value of over 100 cm/s.

Figure 3.14 shows that at $t = .600$ s the region of fluidization extends below 150 cm depth. The soil column above this depth is moving upward, with a maximum velocity of 40 cm/s near the surface. The upward air velocity peaks at the surface with a value of over 80 cm/s.

The progression of fluidization down the soil column can be seen in the soil density depth profiles at various times on Figure 3.15. Up to $t = .100$ s the soil density is still essentially at its initial value of 1.6 gm/cm^3 . The region of fluidization is clearly seen in the profiles at later times. The soil density drops below 1.6 gm/cm^3 as the soil becomes increasingly distended. By $t = .600$ s porosities near the surface have increased to over 0.5.

During the numerical simulations various predicted physical quantities are monitored at several station depths in the 1-D grid. This allows for time histories of quantities such as air

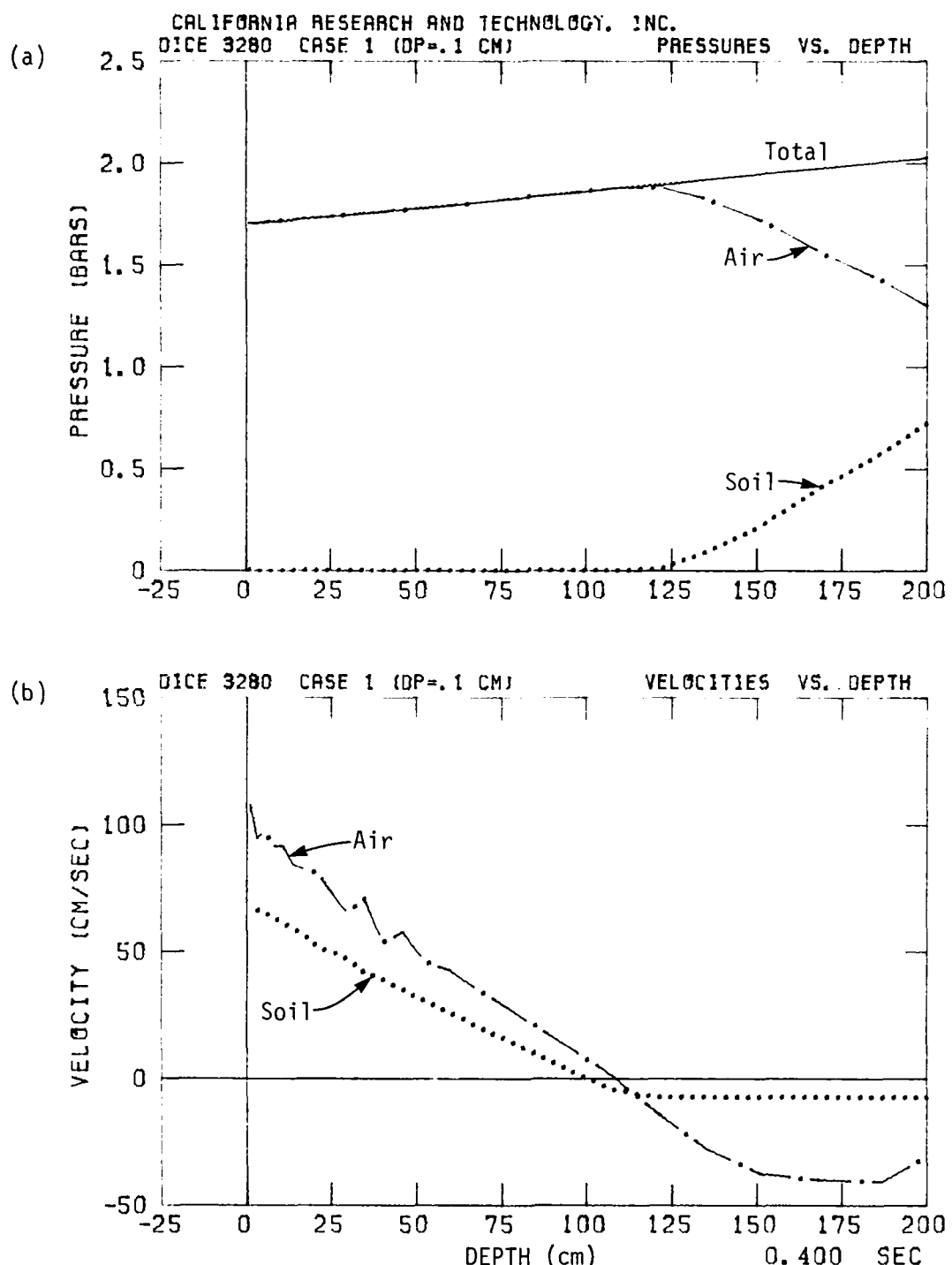


Figure 3.13. (a) Soil, Air and Total Stress Versus Depth, and
 (b) Soil and Air Velocity Versus Depth at
 $t = .400$ Seconds for Case 1 ($D_p = .1$ cm).

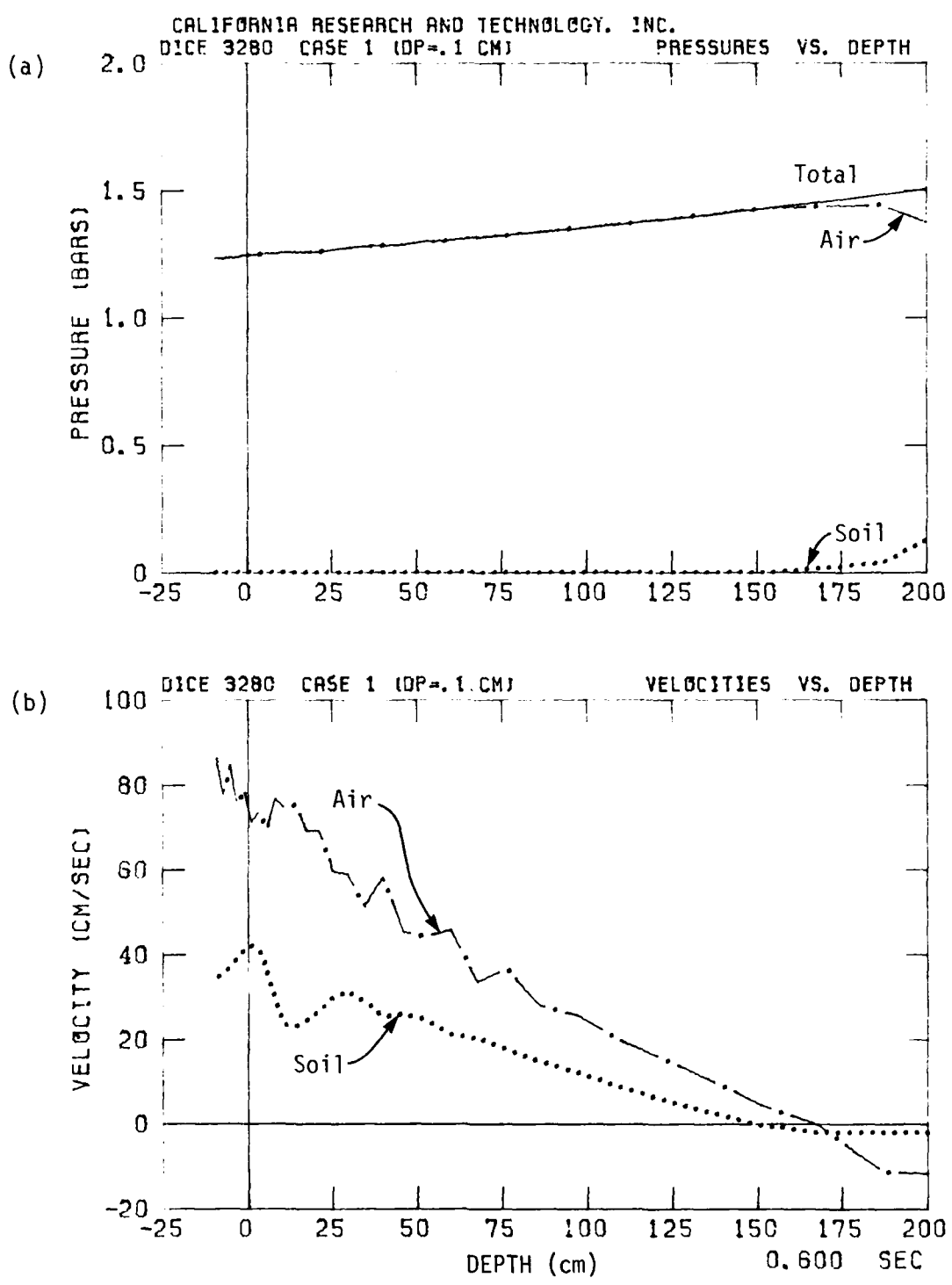


Figure 3.14. (a) Soil, Air and Total Stress Versus Depth, and
 (b) Soil and Air Velocity Versus Depth at
 $t = .600$ Seconds for Case 1 ($D_p = 0.1$ cm).

CALIFORNIA RESEARCH AND TECHNOLOGY, INC.
DICE 3280 CASE 1
SOIL DENSITY VS. DEPTH

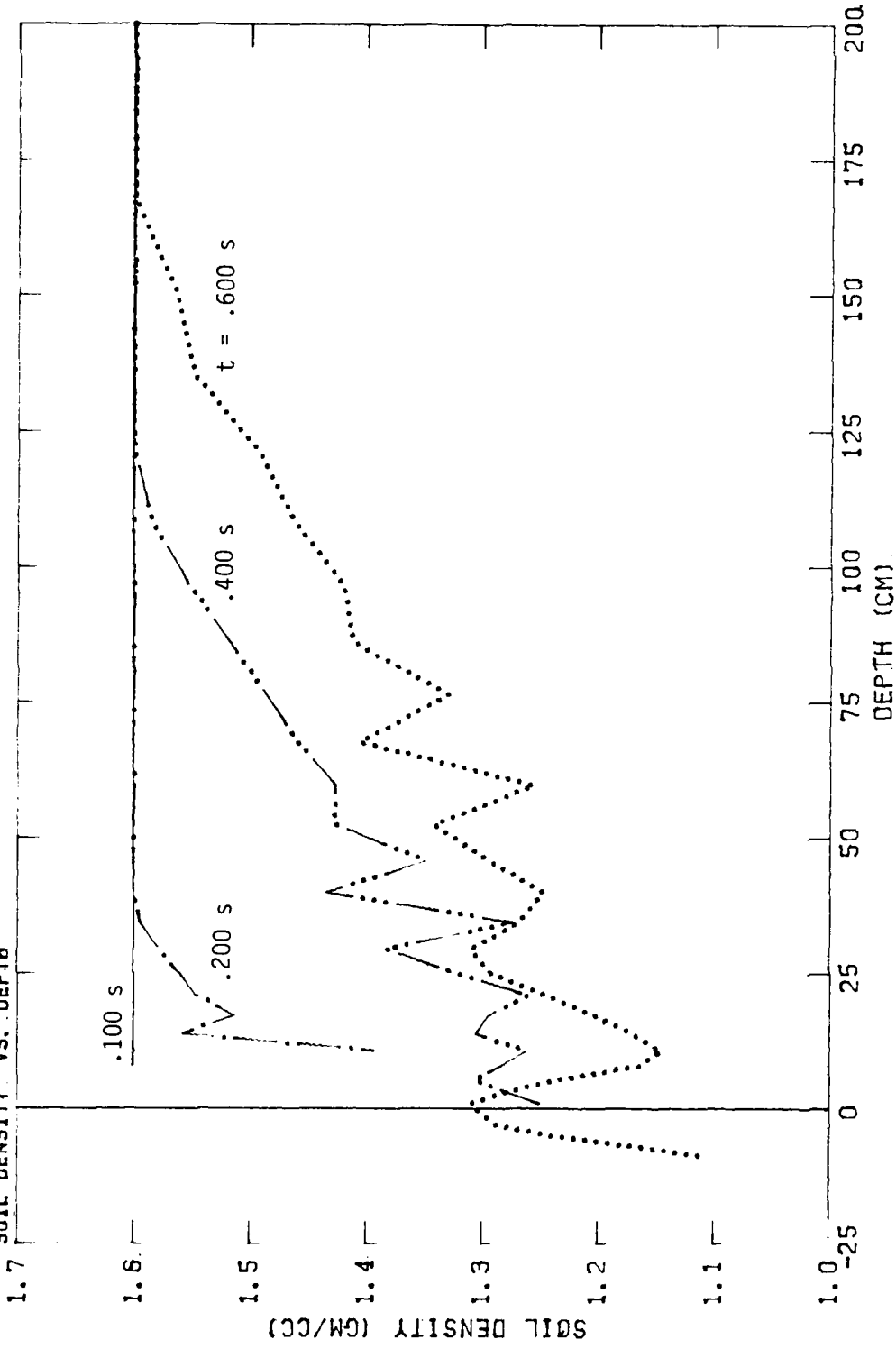


Figure 3.15. Soil Density Versus Depth at Various Times for Case 1 ($D_p = 0.1$ cm).

overpressure and soil velocity at the selected station depths to be analyzed.

Figure 3.16 shows the air overpressure versus time for Case 1 at various station depths of the modeled soil column from 5 cm to 175 cm. The peak overpressure decreases with depth while the time of arrival of the peak overpressure increases with depth. This figure shows that by $t = .200$ s, air overpressures down to 40 cm depth have become approximately equivalent to the overpressure loading applied at the surface. Thus, above 40 cm depth the soil has become fluidized and is supported entirely by the air.

Figure 3.17 shows the soil velocity versus time at various station depths from 5 cm to 175 cm. Up to time $t \sim .100$ s the soil column essentially moves downward as a rigid body. Fluidization at each station depth becomes apparent after this time when the soil flowing at that depth increases its velocity above the velocity of the soil column below that depth. At the 5 cm depth station a maximum upward velocity of ~ 65 cm/s is achieved at $t \sim .400$ s, after which time gravity becomes the dominating force.

3.2.2 Case 2 ($D_p = 0.05$ cm, $g = 980$ cm/s²)

The effect of permeability of the modeled soil is examined in Case 2 by using a characteristic particle size diameter of $D_p = 0.05$ cm, which is half that used in Case 1. For a given porosity, the soil permeability in Case 2 is four times smaller than in Case 1 (see the permeability model described in Section 2.3).

CALIFORNIA RESEARCH AND TECHNOLOGY, INC.
DICE 3280 - CASE 1
AIR OVERPRESSURE VS. TIME FOR STATIONS 7-18

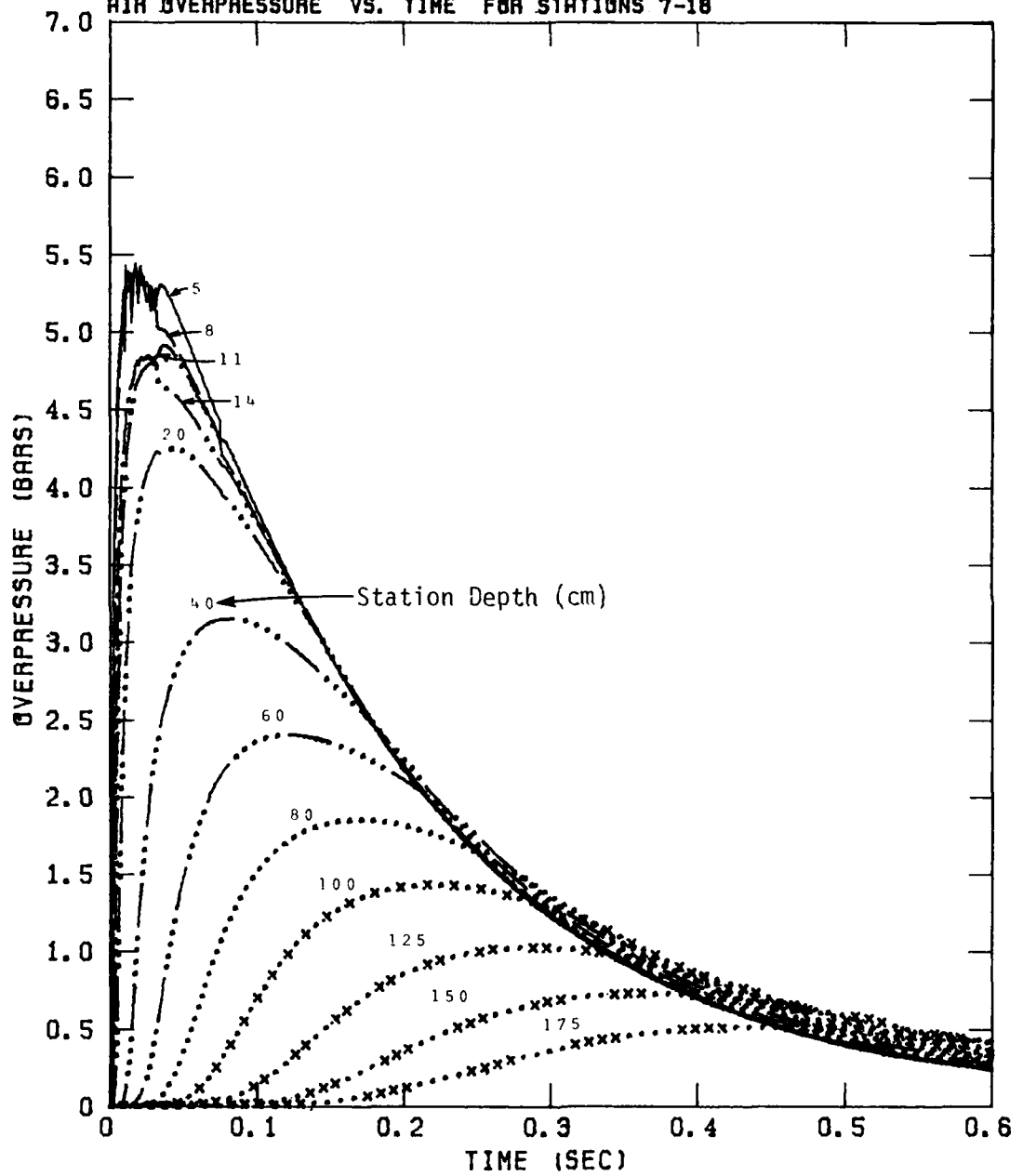


Figure 3.16. Air Overpressure Versus Time at Various Station Depths for Case 1 ($D_p = 0.1$ cm).

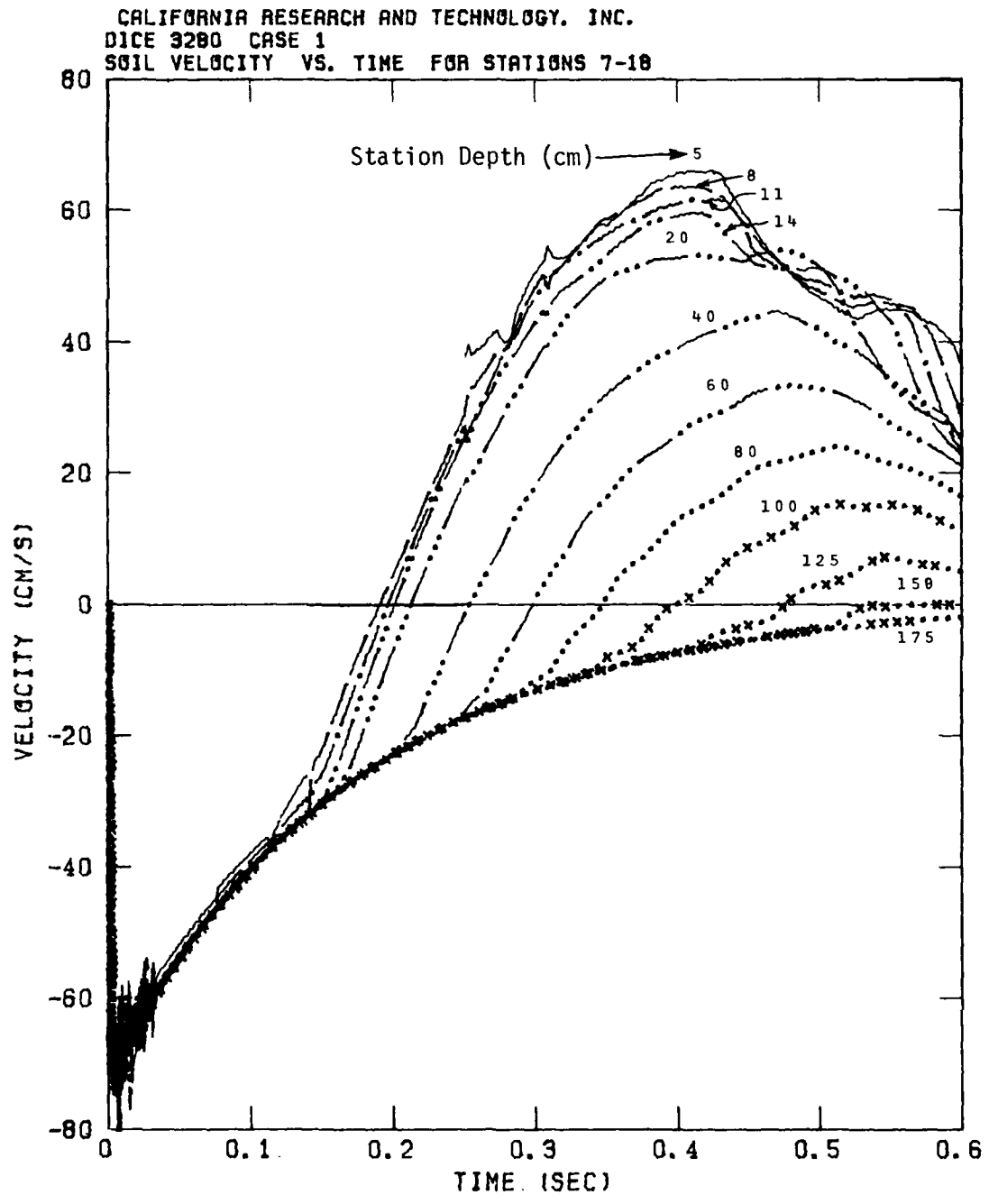


Figure 3.17. Soil Velocity Versus Time at Various Station Depths for Case 1 ($D_p = 0.1$ cm).

Figure 3.18 shows the pressure and velocity distributions for soil and air at $t = .001$ s for Case 2. Air is flowing down through the soil at just over 200 cm/s for Case 2 as compared to over 1500 cm/s for Case 1. There is also a corresponding decrease in the amount of support of the overpressure load at the surface by the air.

By $t = .050$ s (Figure 3.19) the peak downward velocity of ~200 cm/s is found at a depth of 25 cm for Case 2, slower and shallower than the ~330 cm/s peak at 50 cm depth for Case 1. The air pressure also indicates that there is a decrease in permeation of the soil; air is supporting at least part of the pressure loading down to almost 100 cm depth for Case 1, but only to 50 cm for Case 2.

Fluidization at the surface occurs near $t = .100$ s (Figure 3.20) for both Case 1 and Case 2, when the air is supporting the entire pressure load at the surface. By $t = .200$ s, Figure 3.21 shows the soil fluidized to only ~25 cm depth for Case 2, compared to ~40 cm depth for Case 1 (Figure 3.12). By $t = .400$ s (Figure 3.22) the soil in Case 2 is fluidized to a depth of ~70 cm compared to ~120 cm for Case 1, indicating the effect of the decrease in permeability for Case 2.

The air also achieves smaller upward velocities compared with those of Case 1. This is seen in Figure 3.22 at $t = .400$ s and Figure 3.23 at $t = .600$ s. Evidence of the increased air/soil drag forces due to the decrease in permeability is found in the smaller relative velocities between the air and soil particles in the fluidized region.

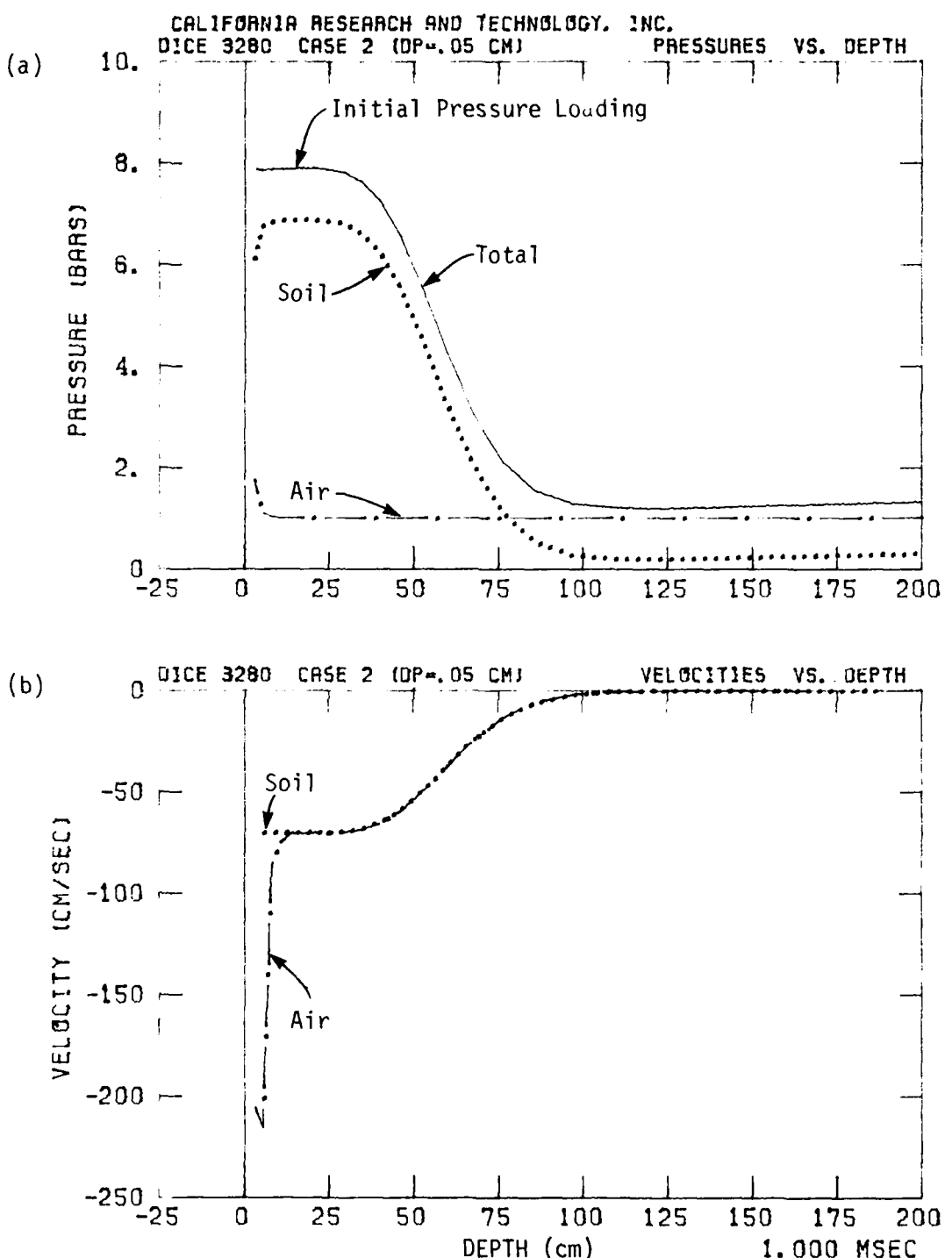


Figure 3.18. (a) Soil, Air and Total Stress Versus Depth, and
 (b) Soil and Air Velocity Versus Depth at
 $t = .001$ Seconds for Case 2 ($D_p = 0.05$ cm).

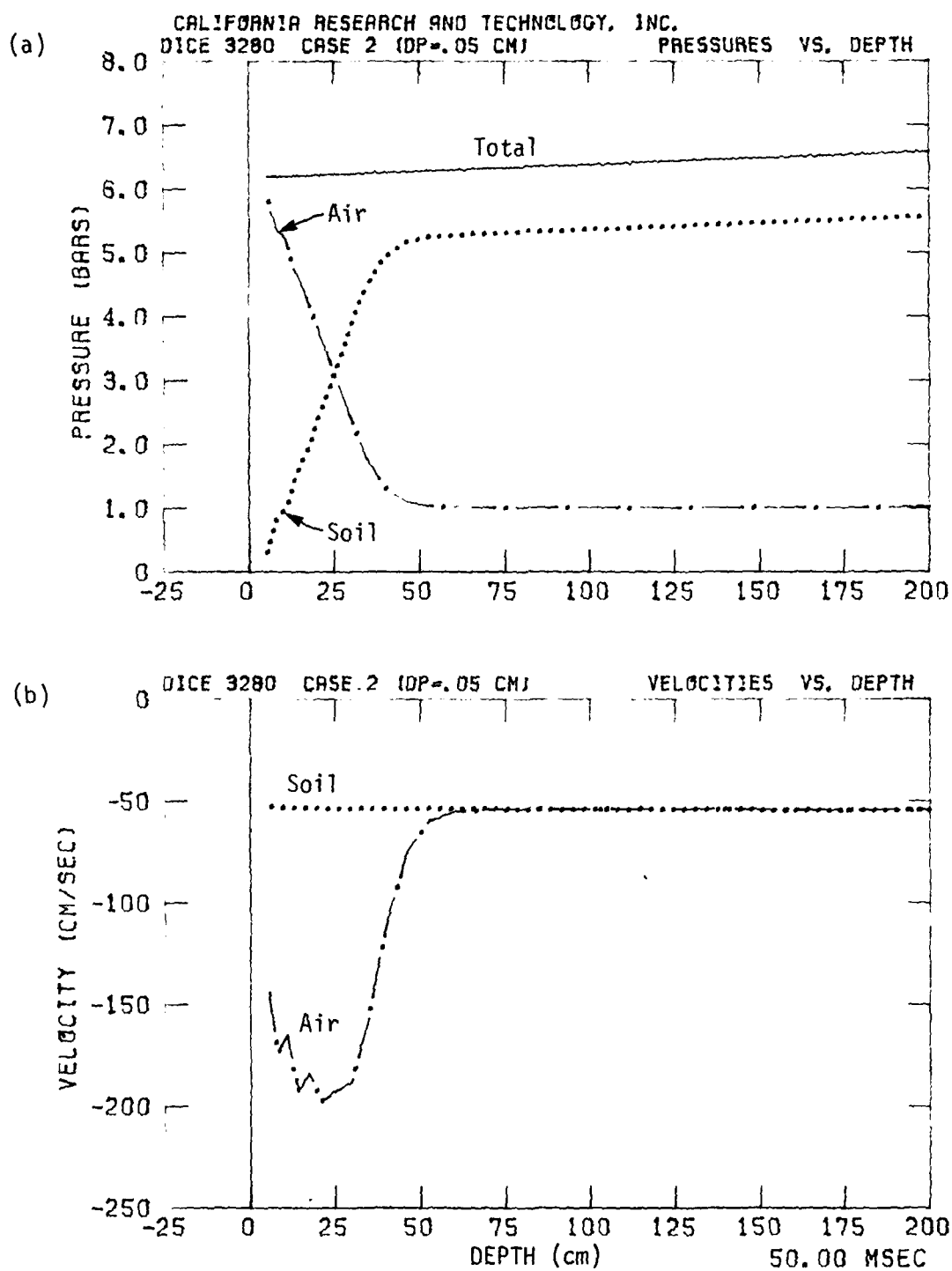


Figure 3.19. (a) Soil, Air and Total Stress Versus Depth, and
 (b) Soil and Air Velocity Versus Depth at
 $t = .050$ Seconds for Case 2 ($D_p = 0.05$ cm).

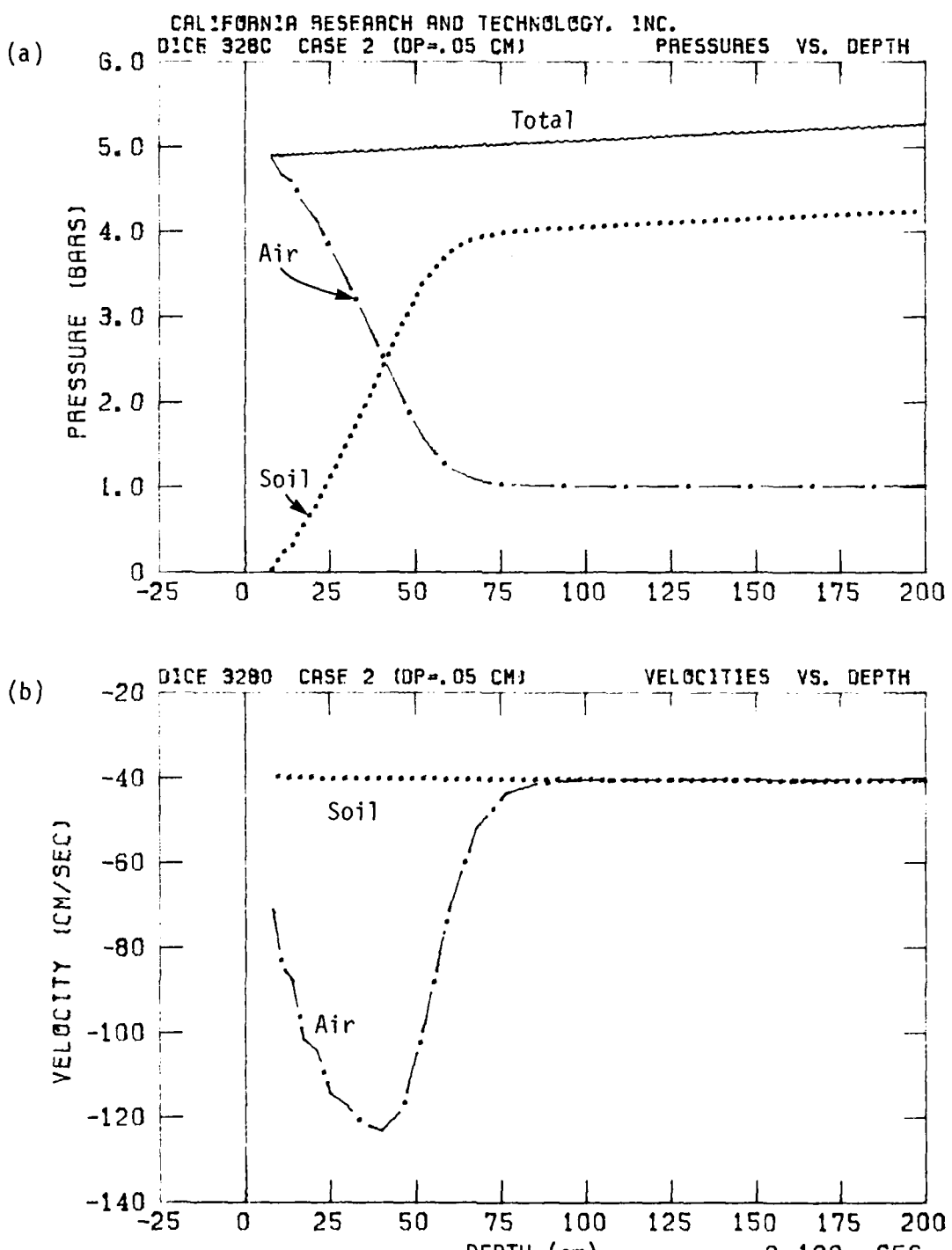


Figure 3.20. (a) Soil, Air and Total Stress Versus Depth, and
 (b) Soil and Air Velocity Versus Depth at
 $t = .100$ Seconds for Case 2 ($D_p = 0.05$ cm).

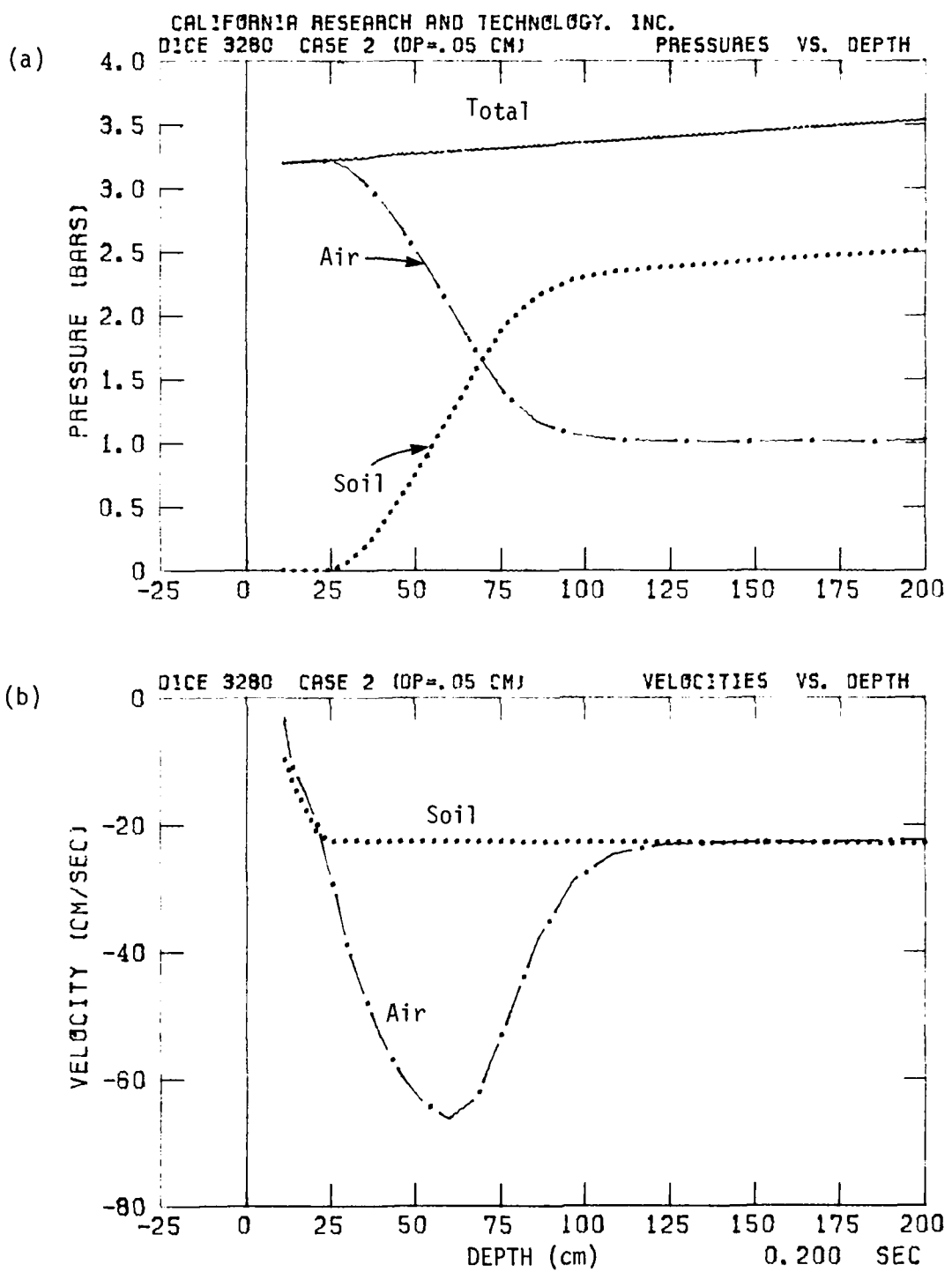


Figure 3.21. (a) Soil, Air and Total Atress Versus Depth, and
 (b) Soil and Air Velocity Versus Depth at
 $t = .200$ Seconds for Case 2 ($D_p = 0.05$ cm).

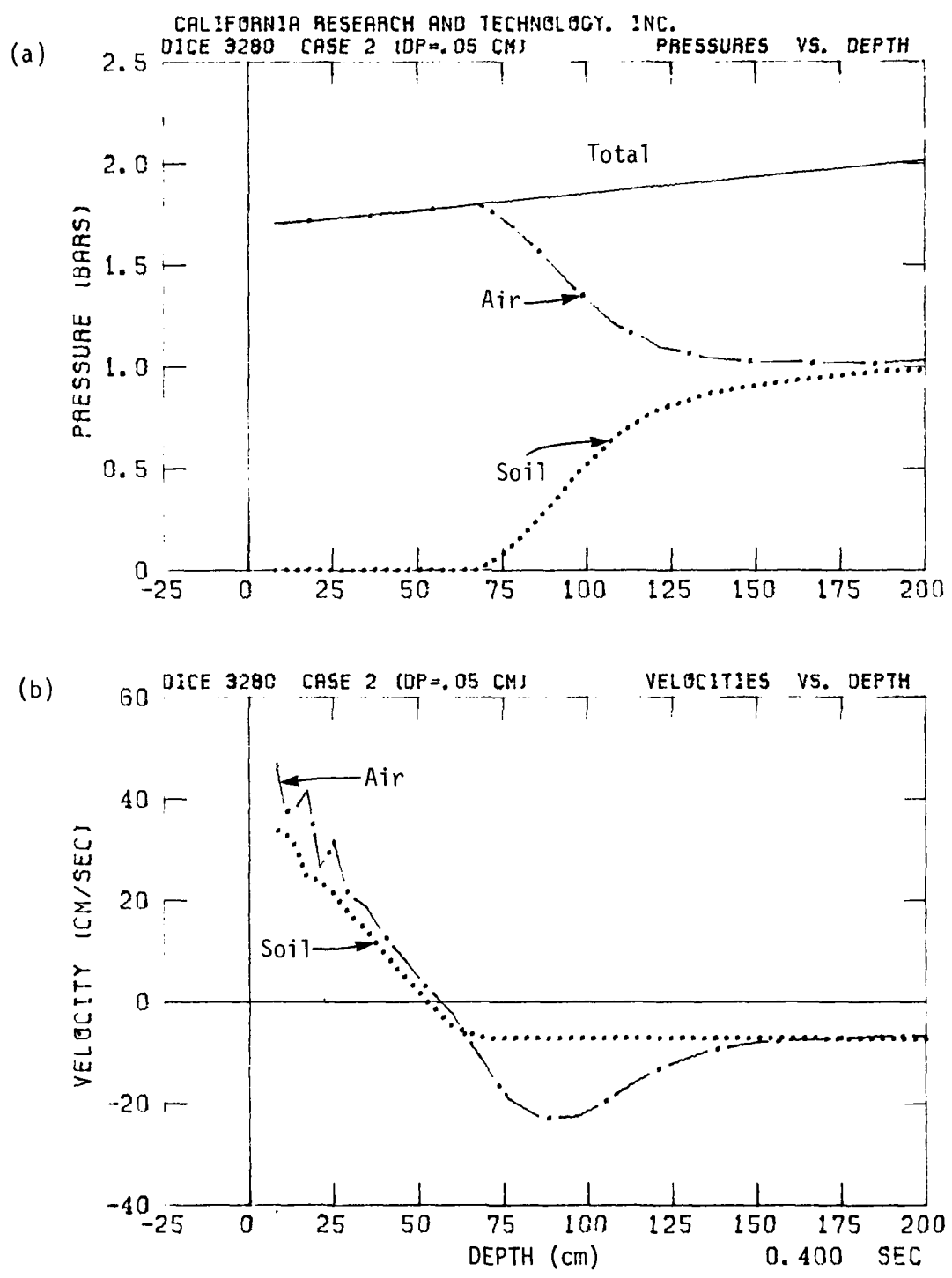


Figure 3.22. (a) Soil, Air and Total Stress Versus Depth, and
 (b) Soil and Air Velocity Versus Depth at
 $t = .400$ Seconds for Case 2 ($D_p = 0.05$ cm).

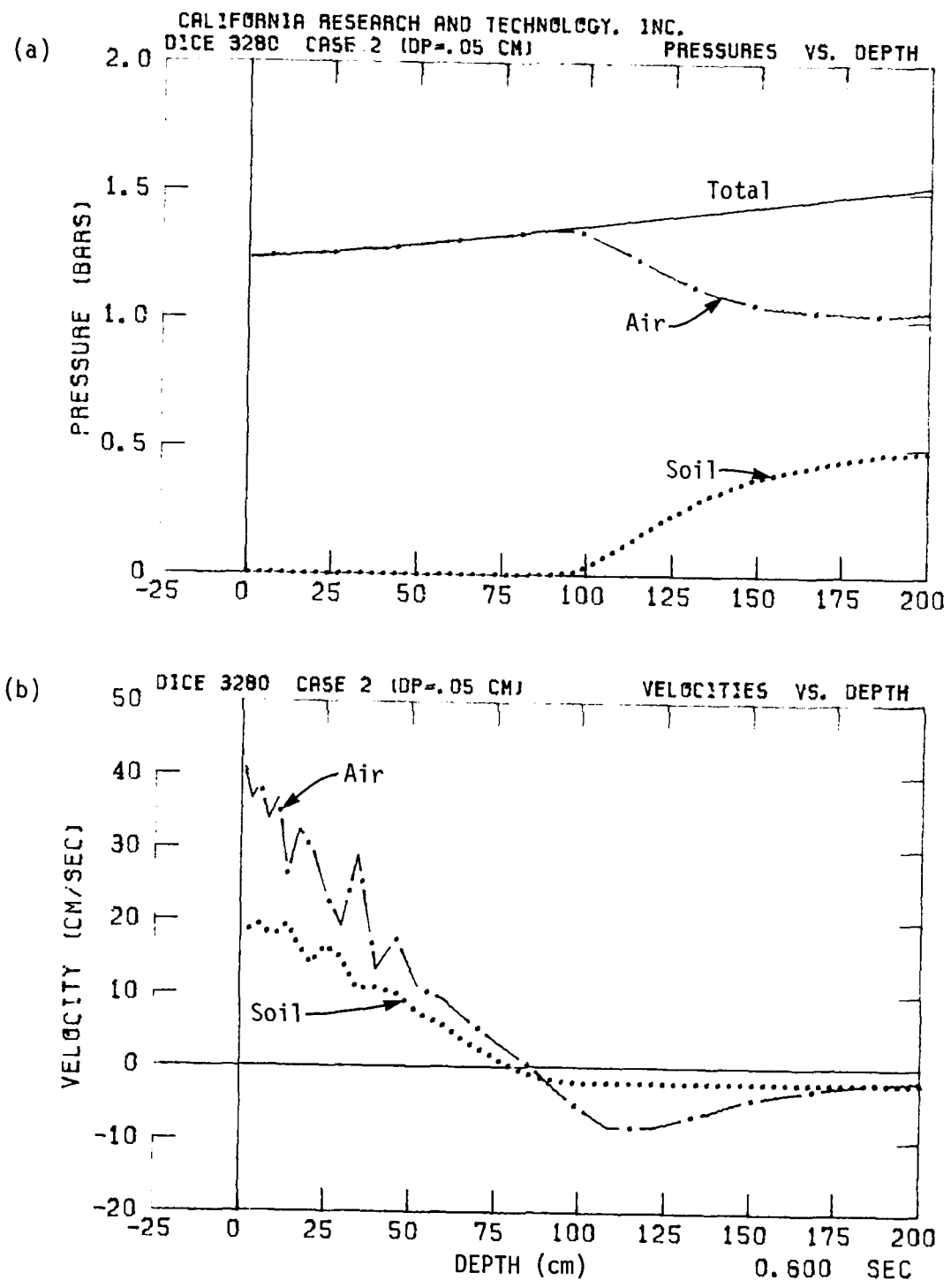


Figure 3.23. (a) Soil, Air and Total Stress Versus Depth, and
 (b) Soil and Air Velocity Versus Depth at
 $t = .600$ Seconds for Case 2 ($D_p = 0.05$ cm).

Figure 3.24 shows the air overpressure time histories at various station depths for Case 2. The peak overpressure at a particular depth is smaller than in Case 1 and also arrives later.

Figure 3.25 shows the soil velocity time histories at various station depths for Case 2. Fluidization is indicated by the increase in velocity at a particular depth above the velocity of the soil column below that depth. Fluidization at a particular depth below the surface occurs at later times for Case 2 than for Case 1. Equation 3.2 indicates that the later time leads to a weaker upward pressure force at that depth for the fluidized soil in Case 2. At the 5 cm depth station a maximum upward velocity of ~35 cm/s is achieved at $t \sim .400$ s. This peak velocity is less than in Case 1 by about a factor of two. However, the time at which the peak occurs is approximately the same in both cases.

3.2.3 Case 3 ($D_p = 0.05$ cm, $g = 0$)

The effect of gravity on the modeled soil column is examined in Case 3 by setting $g = 0$ instead of 980 cm/s² as used in Cases 1 and 2. A characteristic particle size of diameter $D_p = 0.05$ cm is used so that this case compares directly to Case 2. In the absence of gravity there is no initial lithostatic pressure at depth in the soil column required to support the soil weight above that depth. There is only an initial pore air pressure of 1.013 bars (= 1 atm) taken throughout the soil column depth.

Figures 3.26 through 3.31 show the pressure and velocity distributions for soil and air from times $t = .001$ s to $t = .600$ s for Case 3. Up to $t = .100$ s the air pressure and the

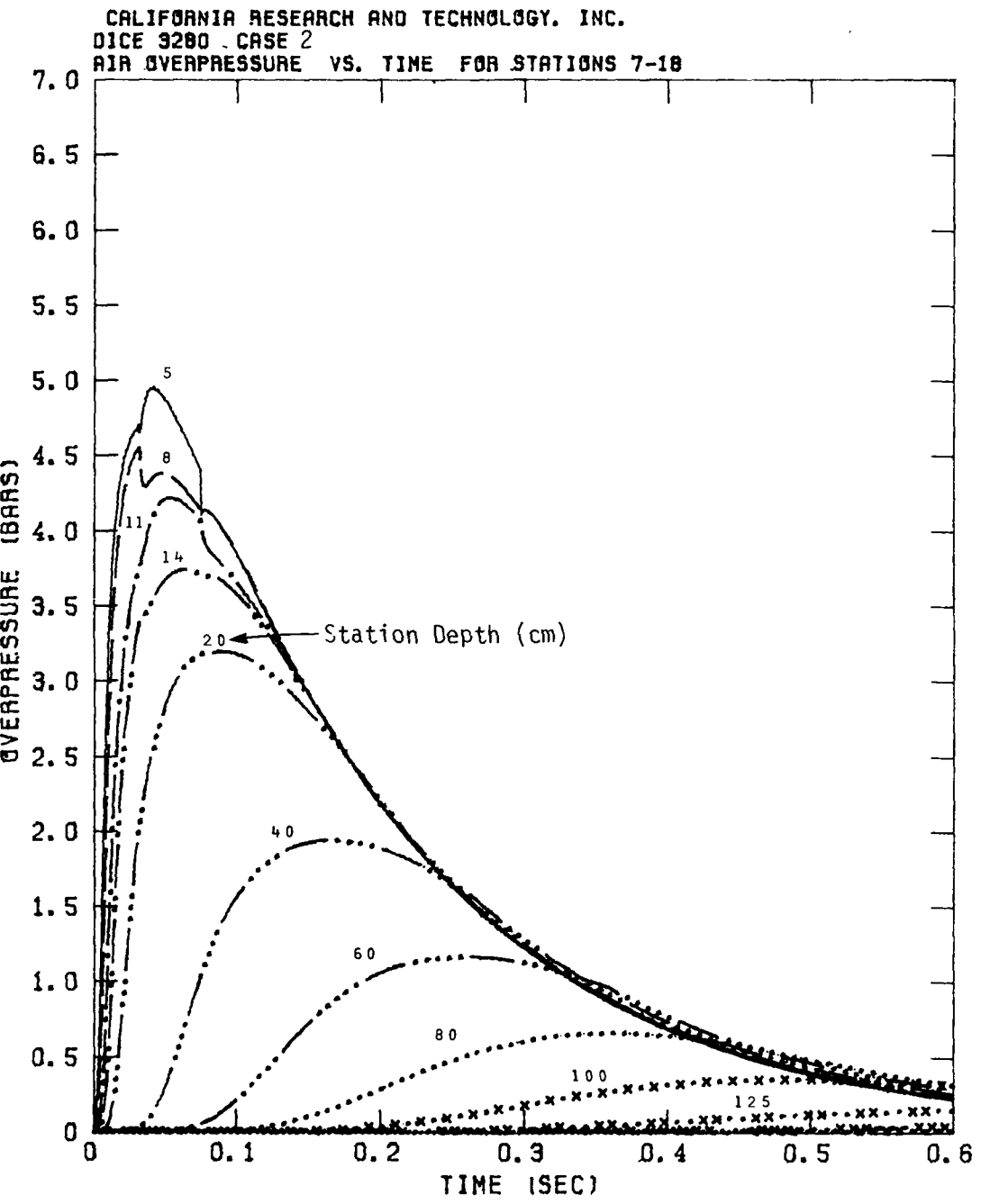


Figure 3.24. Air Overpressure Versus Time at Various Station Depths for Case 2 ($D_p = 0.05$ cm).

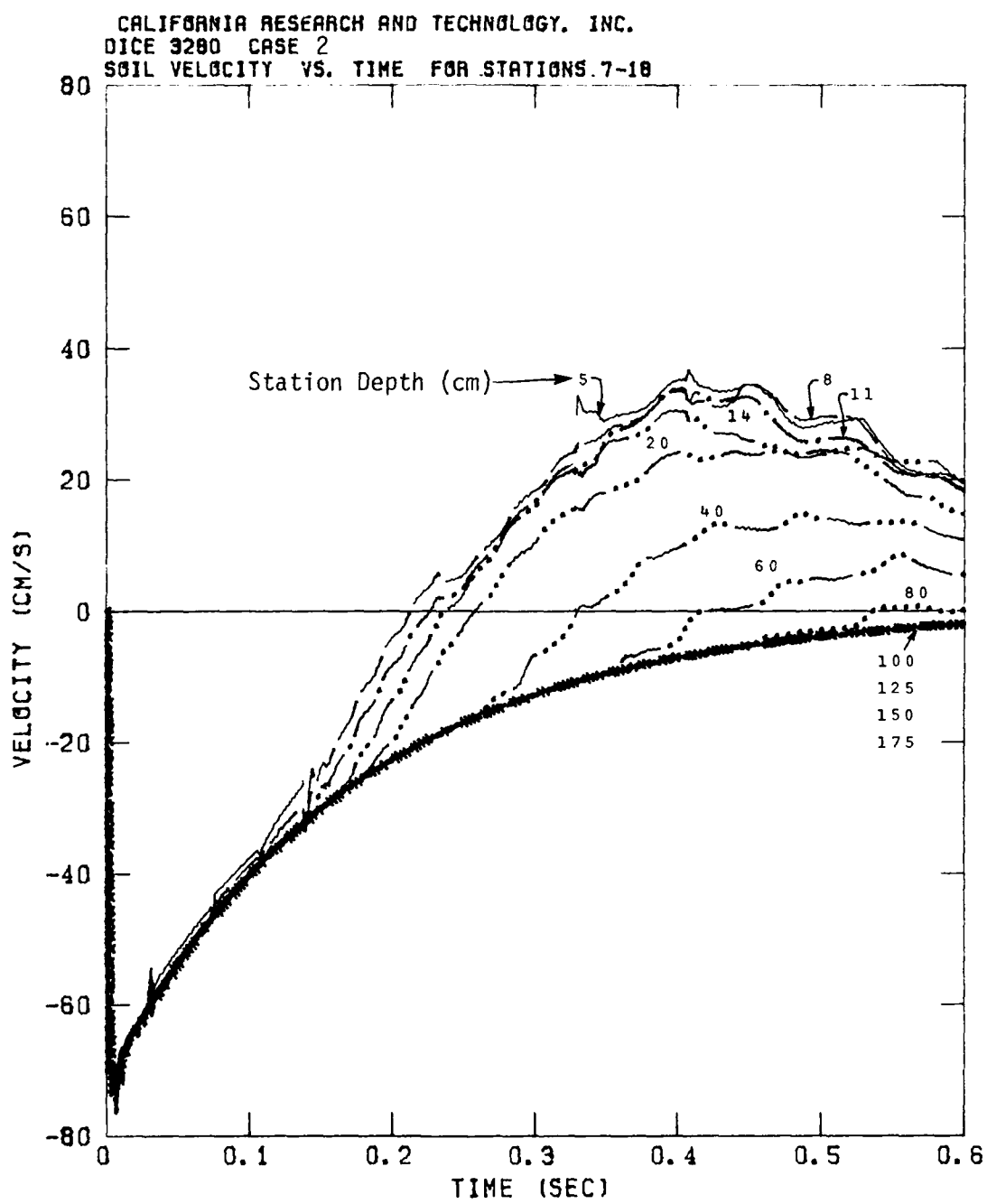


Figure 3.25. Soil Velocity Versus Time At Various Station Depths for Case 2 ($D_p = 0.05$ cm).

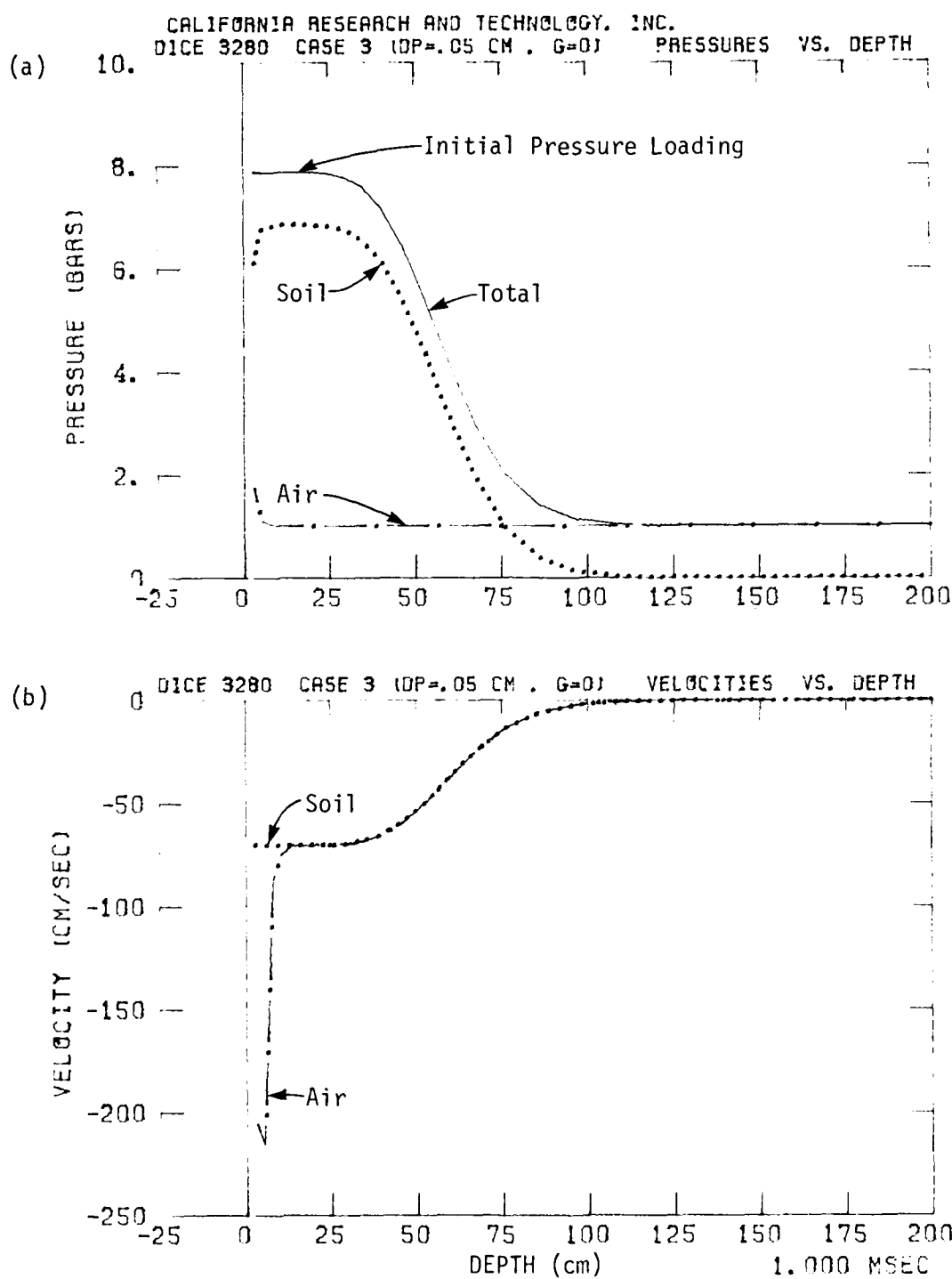
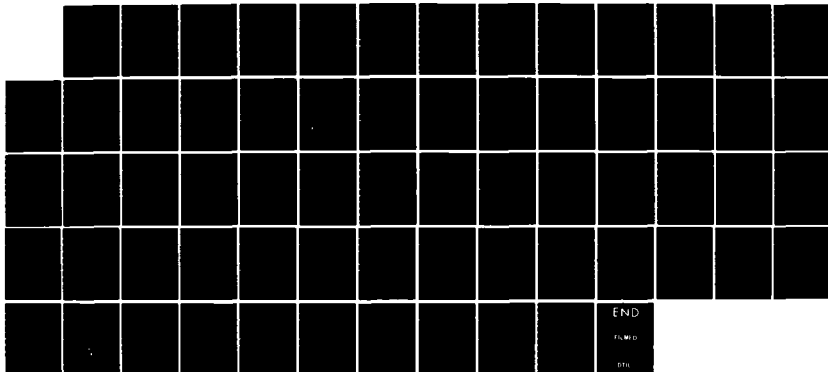


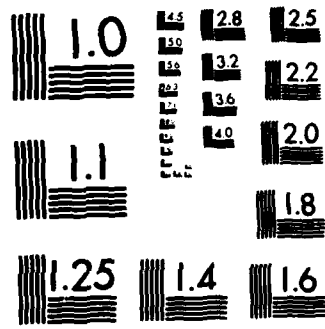
Figure 3.26. (a) Soil, Air and Total Stress Versus Depth, and
(b) Soil and Air Velocity Versus Depth at
 $t = .001$ Seconds for Case 3 ($D_p = 0.05$ cm).

AD-A154 326 SOIL-AIR INTERACTIONS DURING AIRBLAST-INDUCED GROUND MOTIONS(U) CALIFORNIA RESEARCH AND TECHNOLOGY INC
CHATSWORTH M ROSENBLATT ET AL. 01 JAN 82 CRT-3470F

UNCLASSIFIED DNA-TR-81-103 DNA001-81-C-0247 F/G 8/7 NL

2/2





MICROCOPY RESOLUTION TEST CHART
NATIONAL BUREAU OF STANDARDS-1963-A

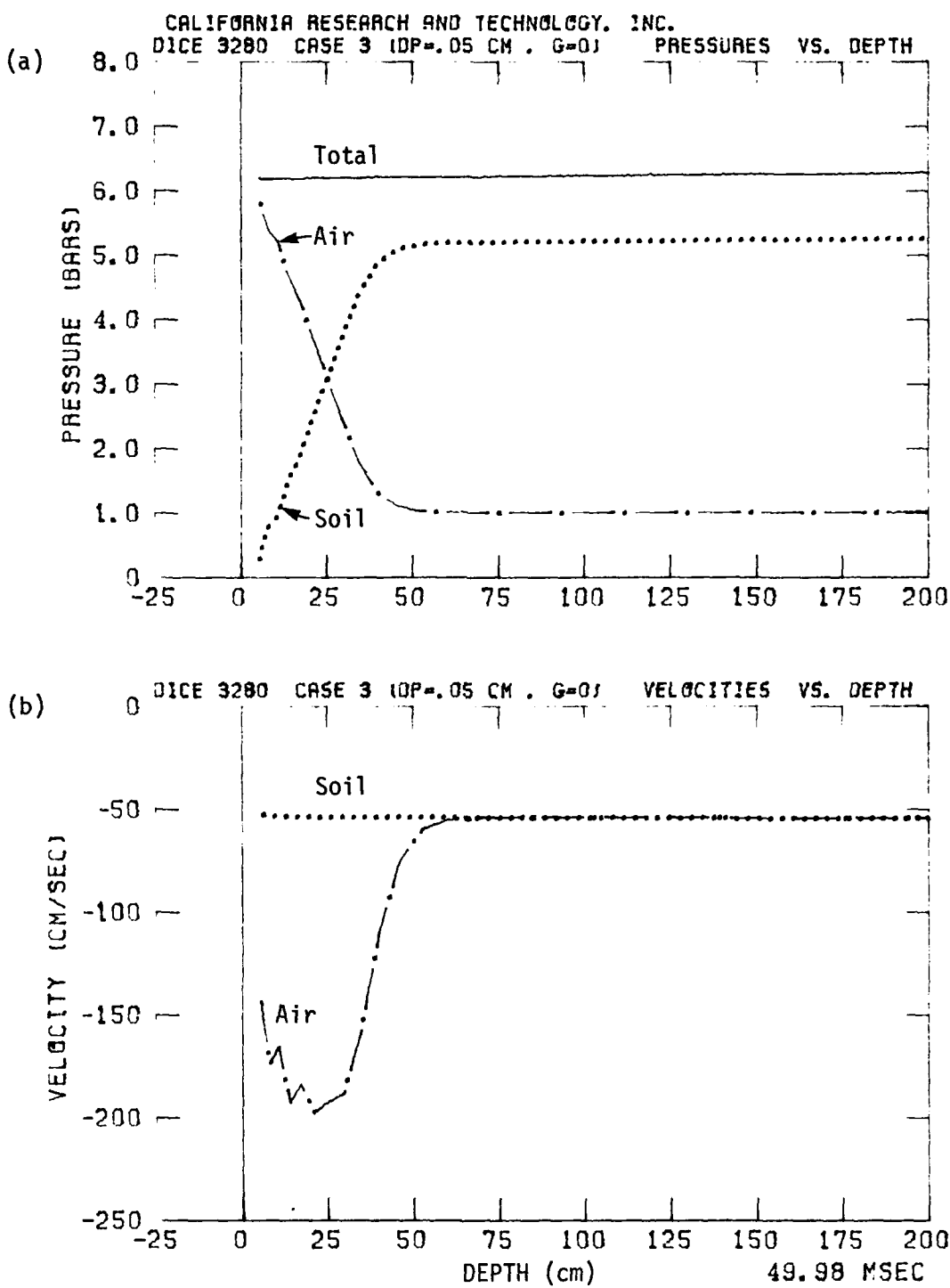


Figure 3.27. (a) Soil, Air and Total Stress Versus Depth, and
 (b) Soil and Air Velocity Versus Depth at
 $t = .050$ Seconds for Case 3 ($D_p = 0.05$ cm).

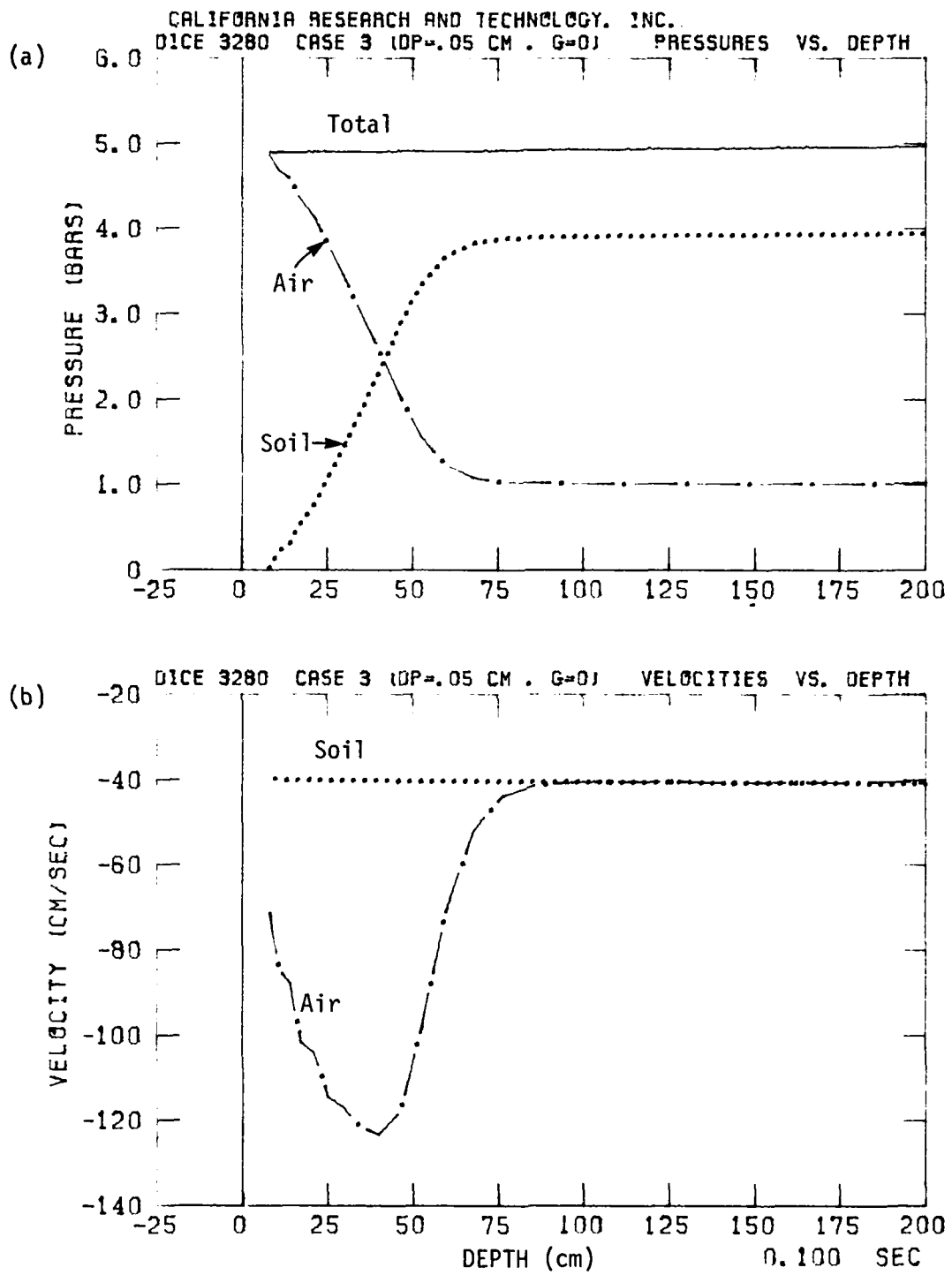


Figure 3.28. (a) Soil, Air and Total Stress Versus Depth, and
(b) Soil and Air Velocity Versus Depth at
 $t = .100$ Seconds for Case 3 ($D_p = .05$ cm).

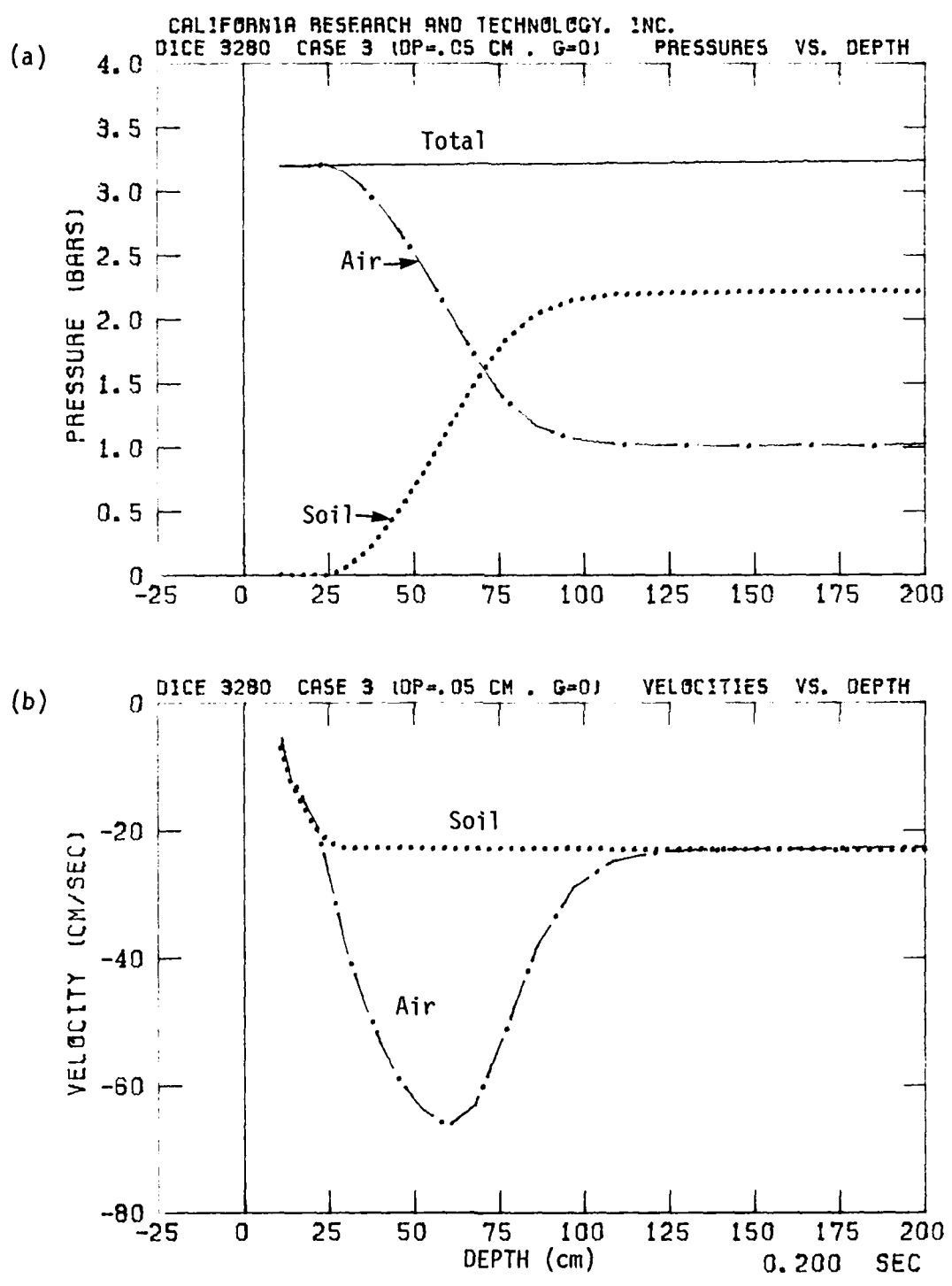


Figure 3.29. (a) Soil, Air and Total Stress Versus Depth, and
 (b) Soil and Air Velocity Versus Depth at
 $t = .200$ Seconds for Case 3 ($D_p = 0.05$ cm).

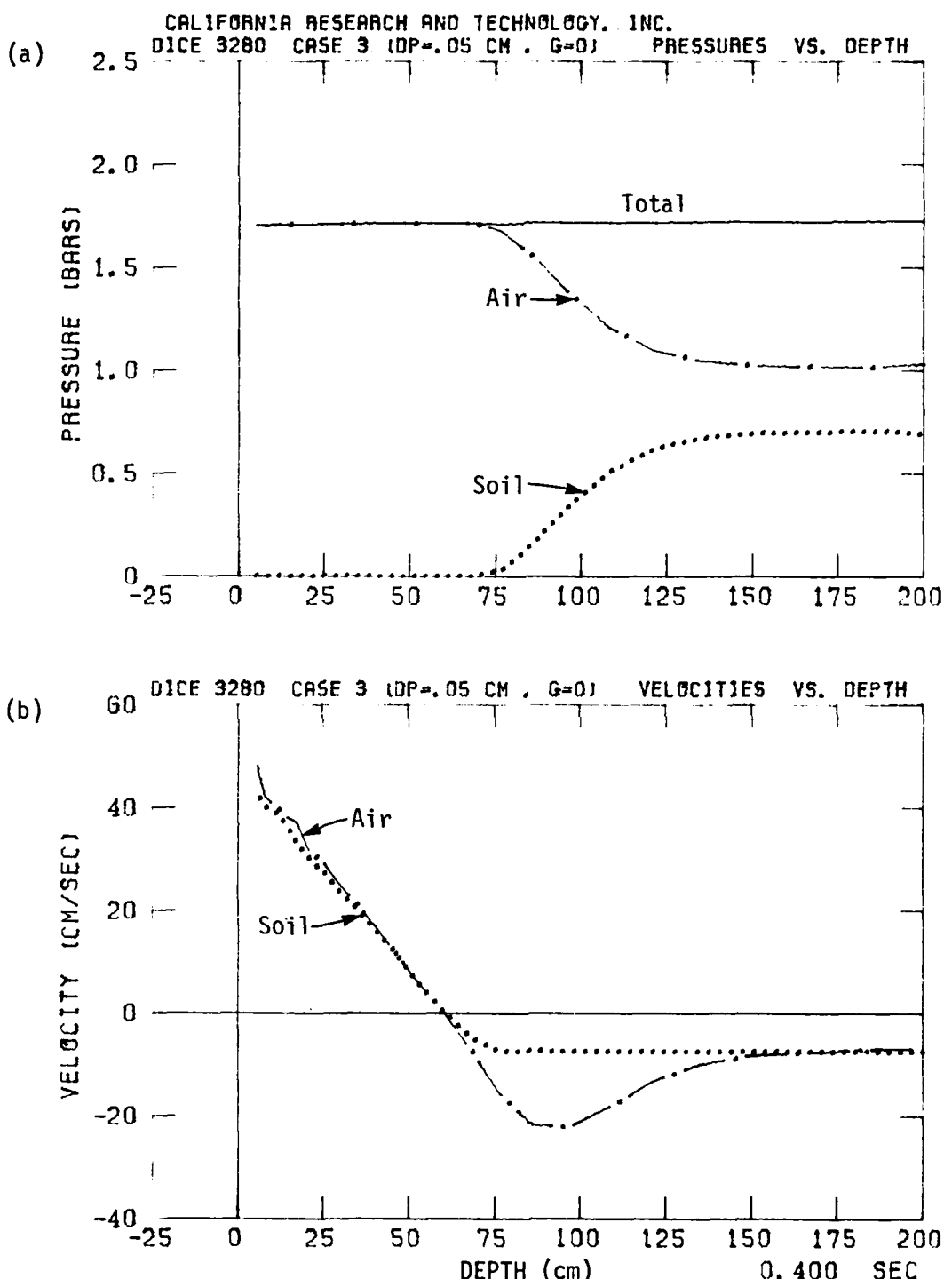


Figure 3.30. (a) Soil, Air and Total Stress Versus Depth, and
 (b) Soil and Air Velocity Versus Depth at
 $t = .400$ Seconds for Case 3 ($D_p = 0.05$ cm).

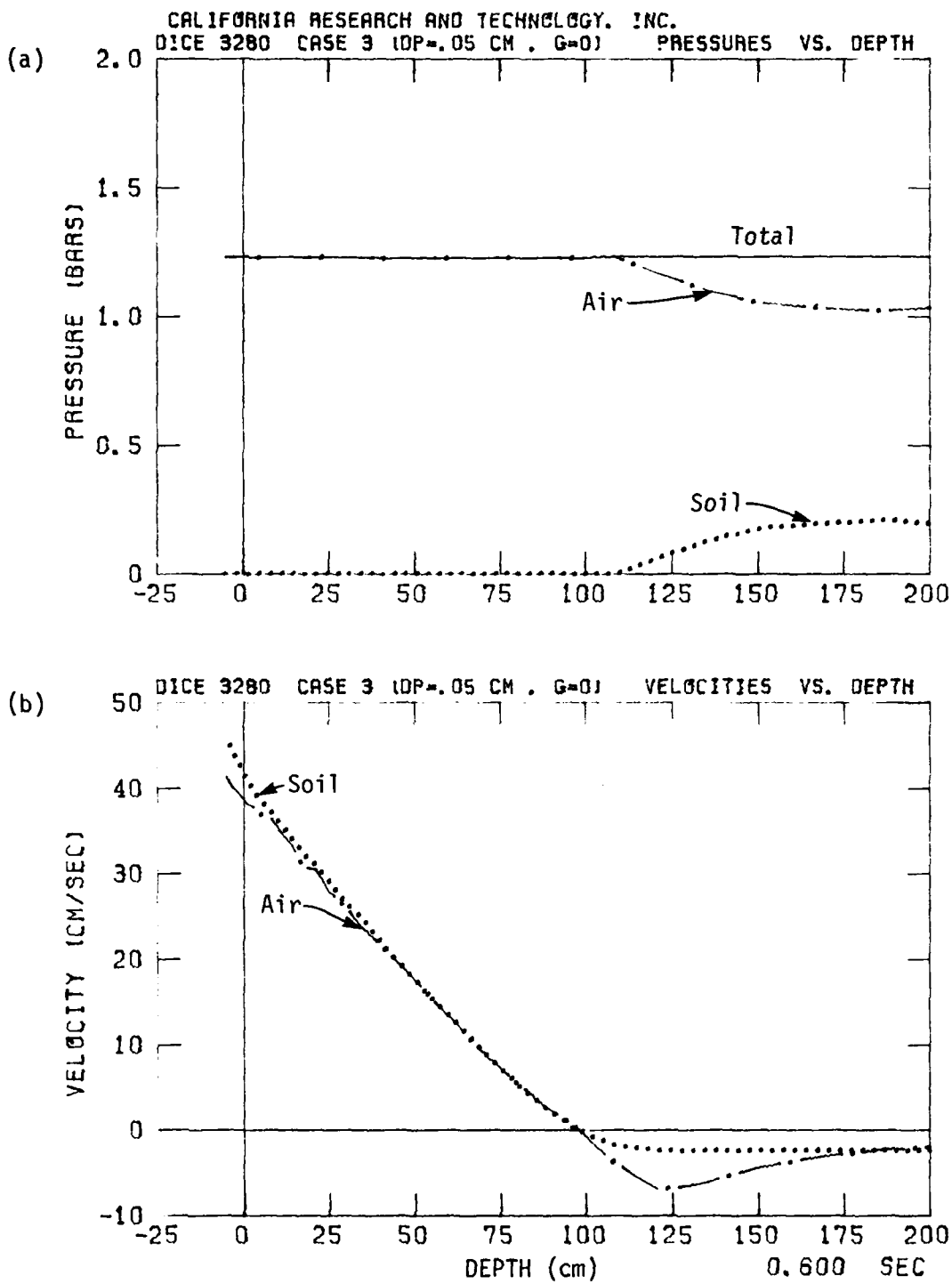


Figure 3.31. (a) Soil, Air and Total Stress Versus Depth, and
 (b) Soil and Air Velocity Versus Depth at
 $t = .600$ Seconds for Case 3 ($D_p = 0.05$ cm).

soil and air velocity distributions are essentially the same as those of Case 2. The soil pressure differences reflect the initial lithostatic pressure field imposed in Case 2.

By $t = .200$ s the soil is fluidized to ~25 cm depth for both Case 3 and Case 2. For Case 3 the relative velocity between the air and soil in this region is almost zero, the air being slightly larger in the upward direction. The relative velocity is larger for Case 2 due to gravity, which accelerates the soil downward in the opposite direction from the upward accelerating air. Internal interaction forces will influence the motion until there is no relative velocity between the soil and air.

By $t = .400$ s, the soil is fluidized to ~75 cm depth for Case 3 compared to ~70 cm depth for Case 2. The difference becomes larger with increasing depth because for Case 2, the air pressure at a particular depth must overcome the initial lithostatic pressure as well as the pressure in the soil resulting from the surface pressure loading before the soil becomes fluidized.

The upward velocity of the air in the fluidized region is approximately the same for both cases at $t = .400$ s and $t = .600$ s. But again, the relative velocity is larger for Case 2 as gravity acts on the soil. By $t = .600$ s the soil particles are in fact moving upward faster than the air for Case 3.

Figure 3.32 shows the air overpressure time histories at various station depths for Case 3. When compared to Case 2 (Figure 3.23) they appear almost identical. However, for Case 3 the overpressures all fall along the same decay path once the soil has been fluidized at the various depths. In Case 2, each

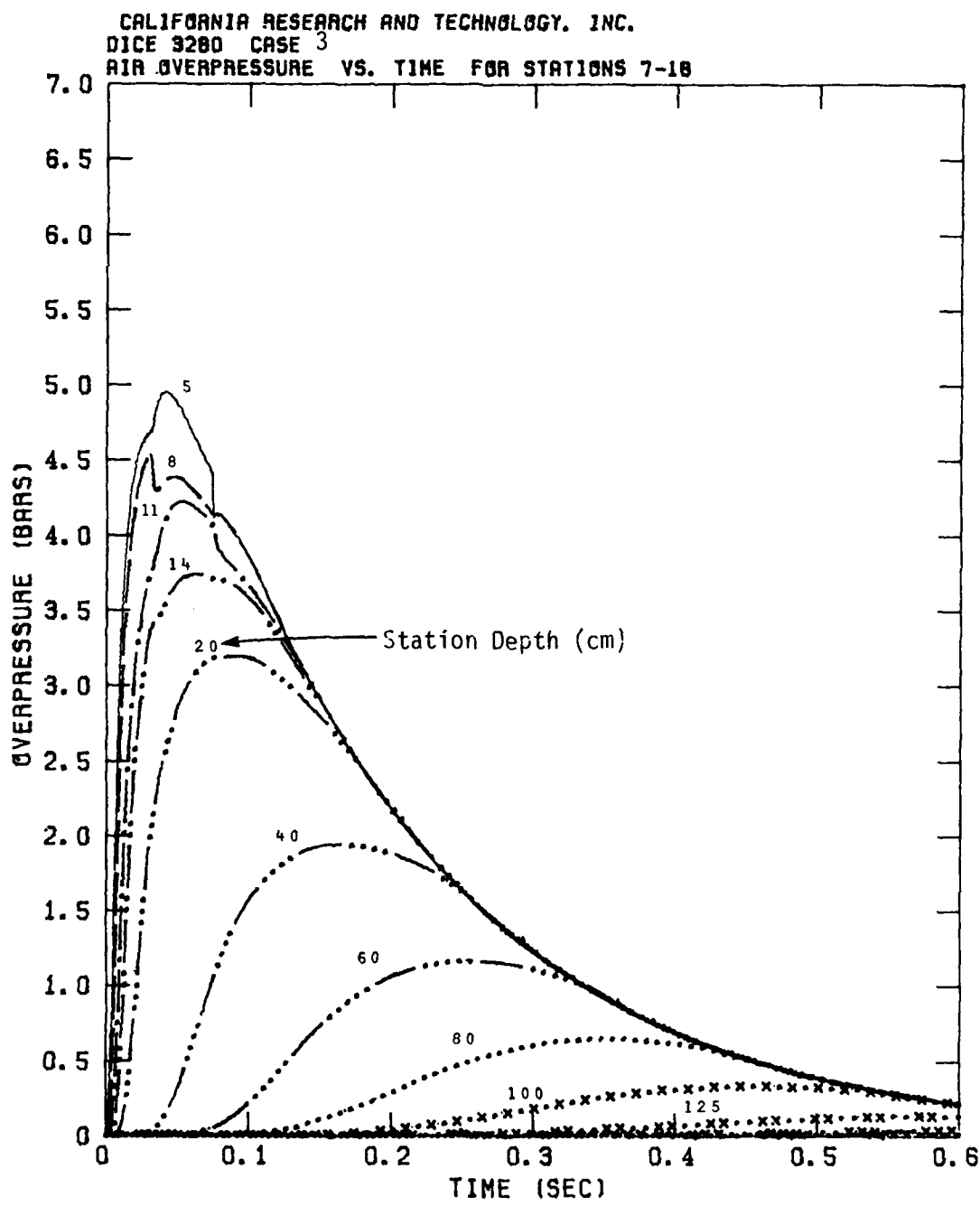


Figure 3.32. Air Overpressure Versus Time at Various Station Depths for Case 3 ($D_p = 0.05$ cm).

successively deeper station required a larger air overpressure to fluidize the soil, due to the initial lithostatic field.

Figure 3.33 shows the soil velocity time histories at various station depths for Case 3. The fluidized soil velocities are larger than in Case 2, again due to the lack of gravity in Case 3. The peak soil velocity for the 5 cm station depth is ~45 cm/s in Case 3 compared to ~35 cm/s in Case 2.

3.2.4 Case 4 ($D_p = 0.142$ cm, $g = 0$)

The effect of increased permeability of the soil column without the effects of gravity is examined in Case 4 by using a characteristic particle size diameter of $D_p = 0.142$ cm. For a given porosity, the permeability model described in Section 2 yields a soil permeability in Case 4 which is over eight times larger than in Case 3.

Figures 3.34 through 3.39 show the pressure and velocity distributions for soil and air from time $t = .001$ s to $t = .400$ s for Case 4. The increase in permeability is seen immediately at $t = .001$ sec. Air is flowing down through the soil at almost 5000 cm/s compared to ~200 cm/s for Case 3. Air is supporting at least part of the pressure loading down to ~20 cm depth for Case 4, compared to ~5 cm for Case 3.

By $t = .050$ s (Figure 3.35) the peak downward velocity of ~450 cm/s is at a depth of 75 cm for Case 4, faster and deeper than the ~200 cm/s peak at 25 cm depth for Case 3. The air pressure also indicates the increase in permeation of the soil; the air is supporting at least part of the pressure loading down to over 125 cm depth for Case 4, but only to 50 cm for Case 3.

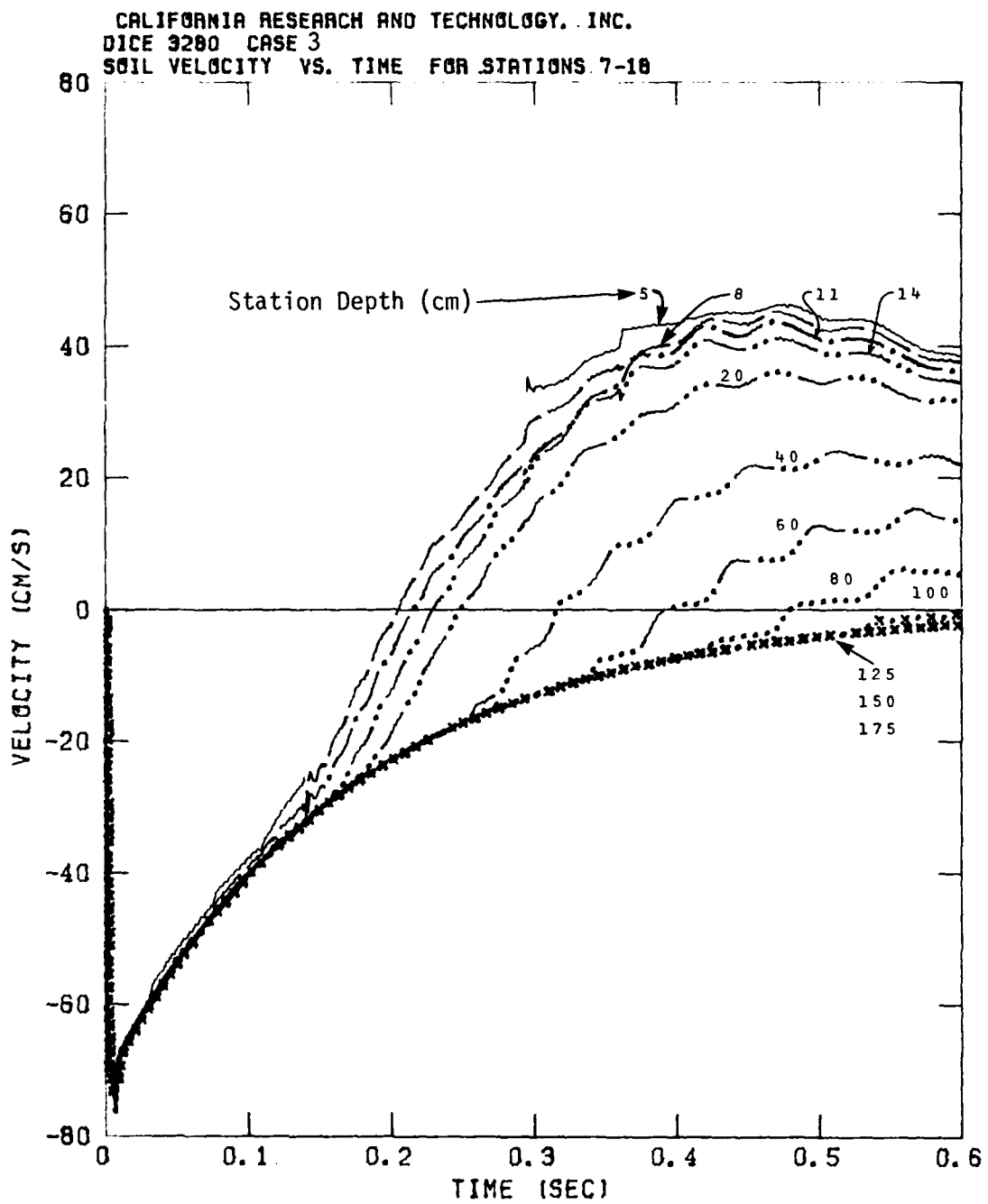


Figure 3.33. Soil Velocity Versus Time at Various Station Depths for Case 3 ($D_p = 0.05$ cm).

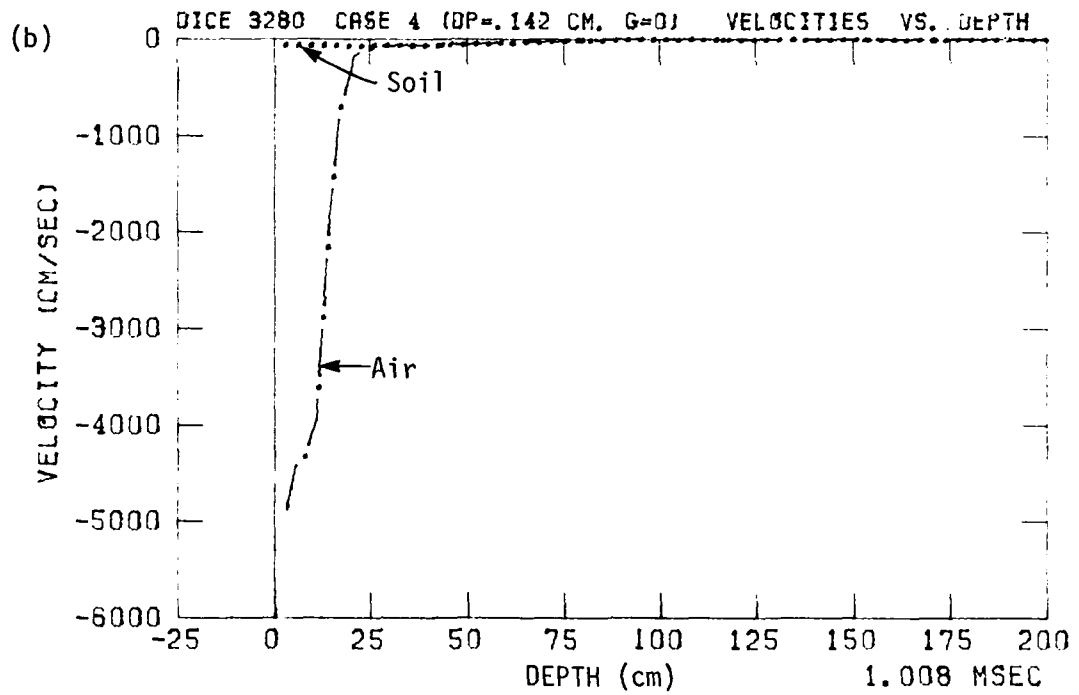
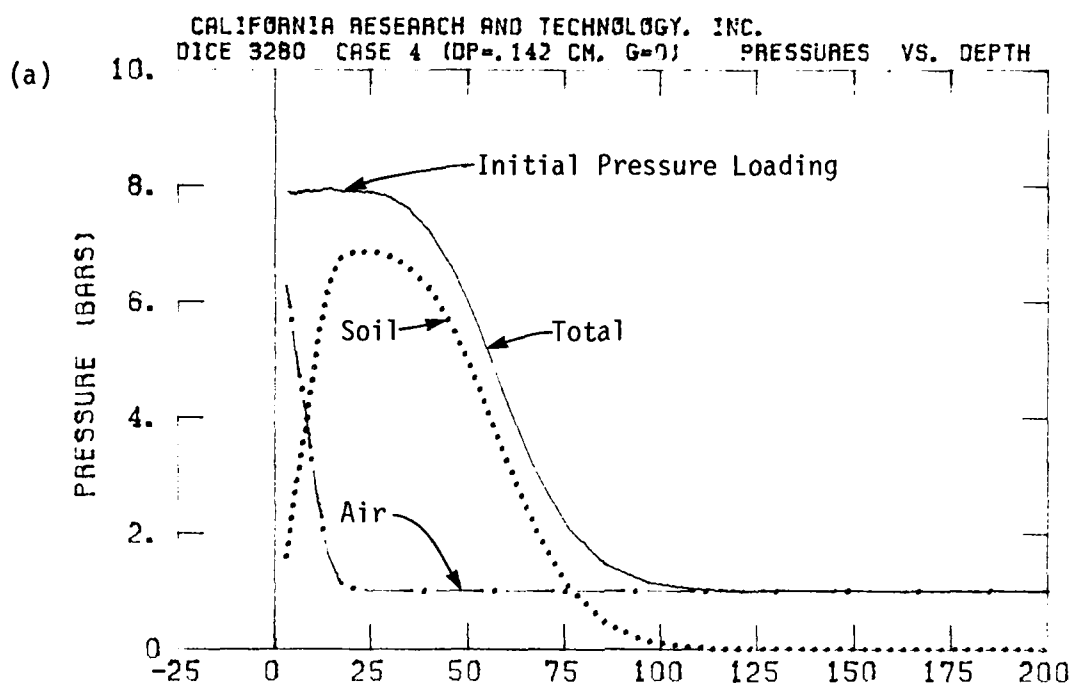


Figure 3.34. (a) Soil, Air and Total Stress Versus Depth, and
(b) Soil and Air Velocity Versus Depth at
 $t = .001$ Seconds for Case 4 ($D_p = 0.142$ cm).

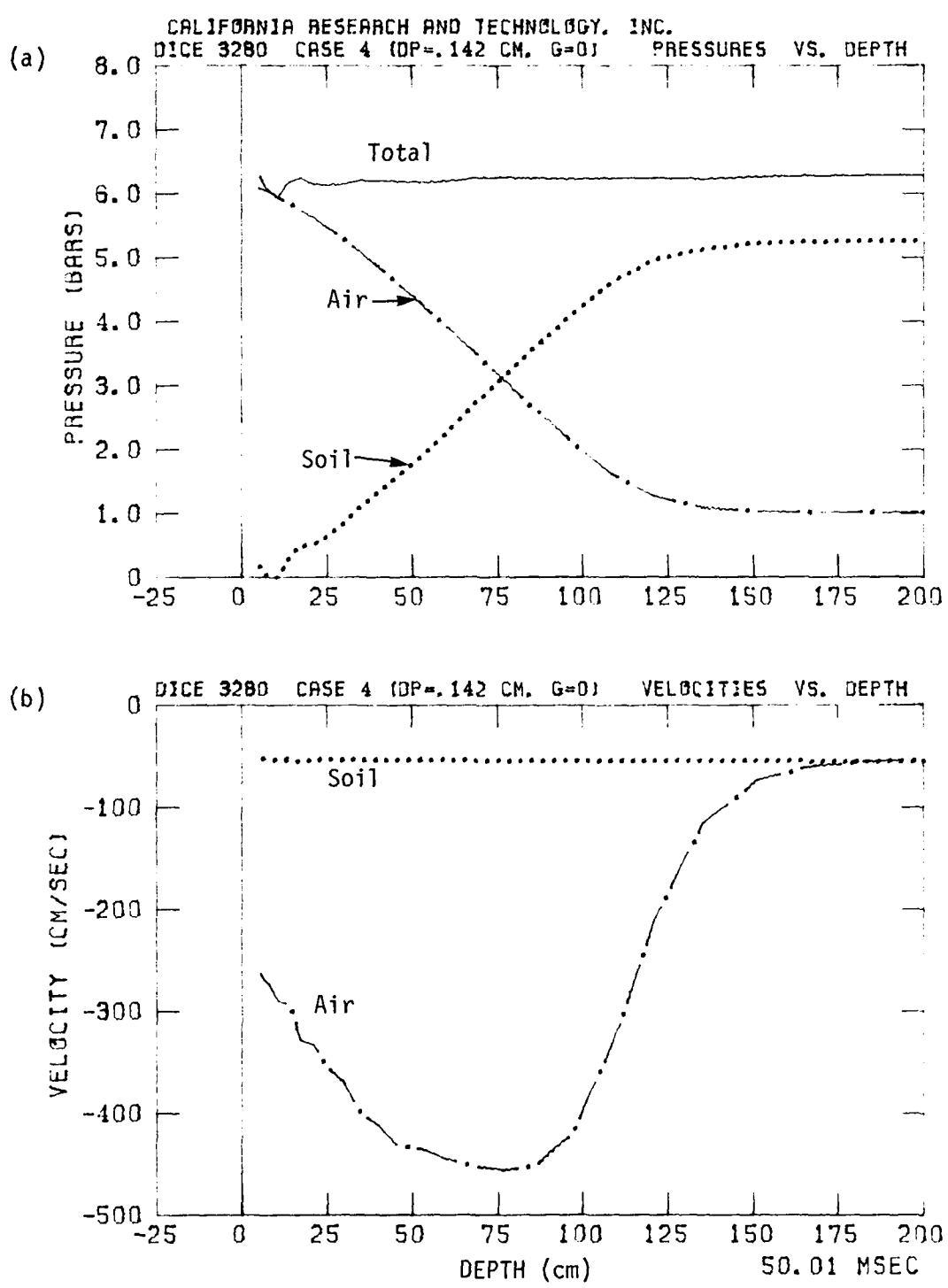


Figure 3.35. (a) Soil, Air and Total Stress Versus Depth, and
 (b) Soil and Air Velocity Versus Depth at
 $t = .050$ Seconds for Case 4 ($D_p = 0.142$ cm).

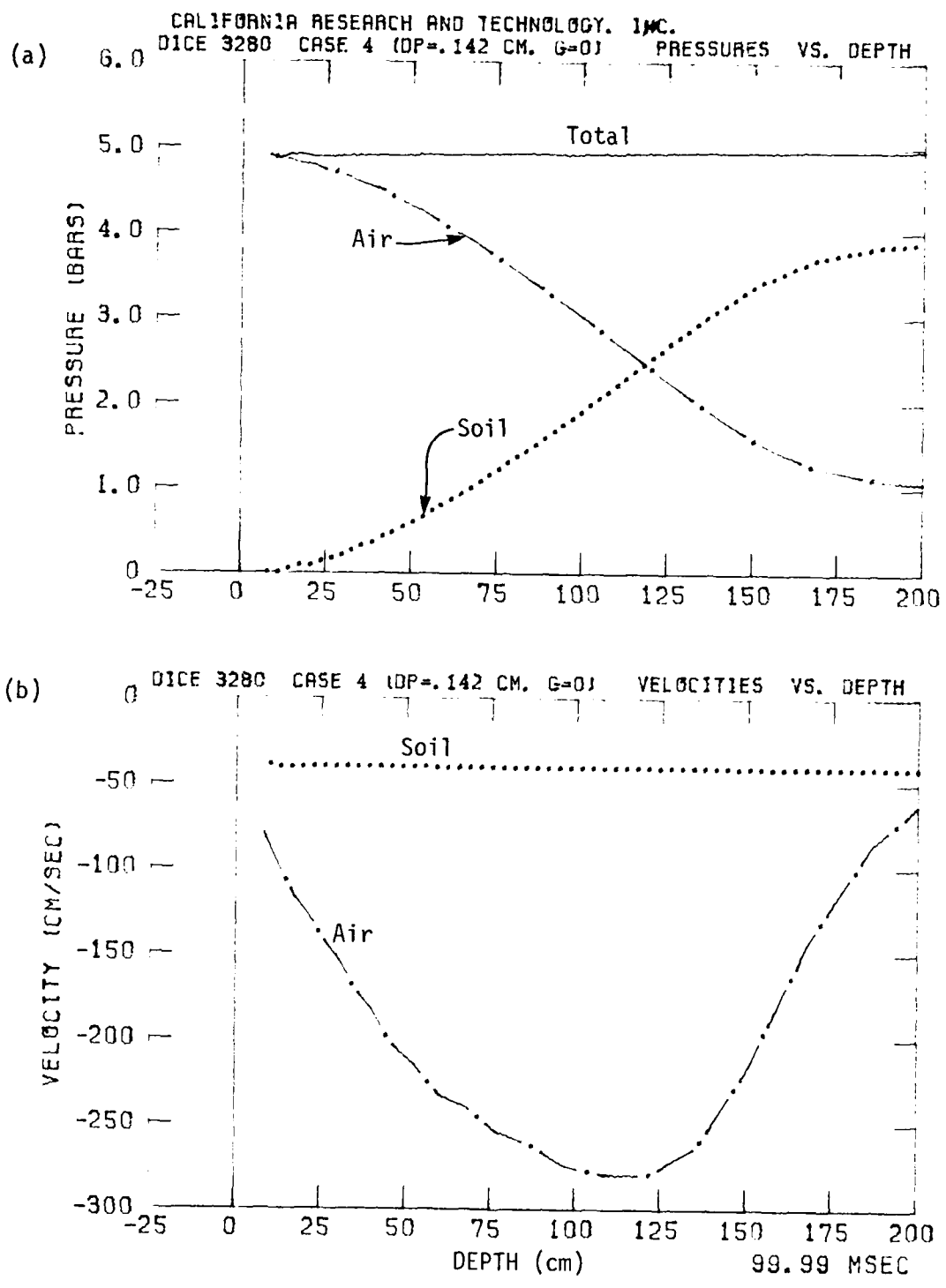


Figure 3.36. (a) Soil, Air and Total Stress Versus Depth, and
 (b) Soil and Air Velocity Versus Depth at
 $t = .100$ Seconds for Case 4 ($D_p = 0.142$ cm).

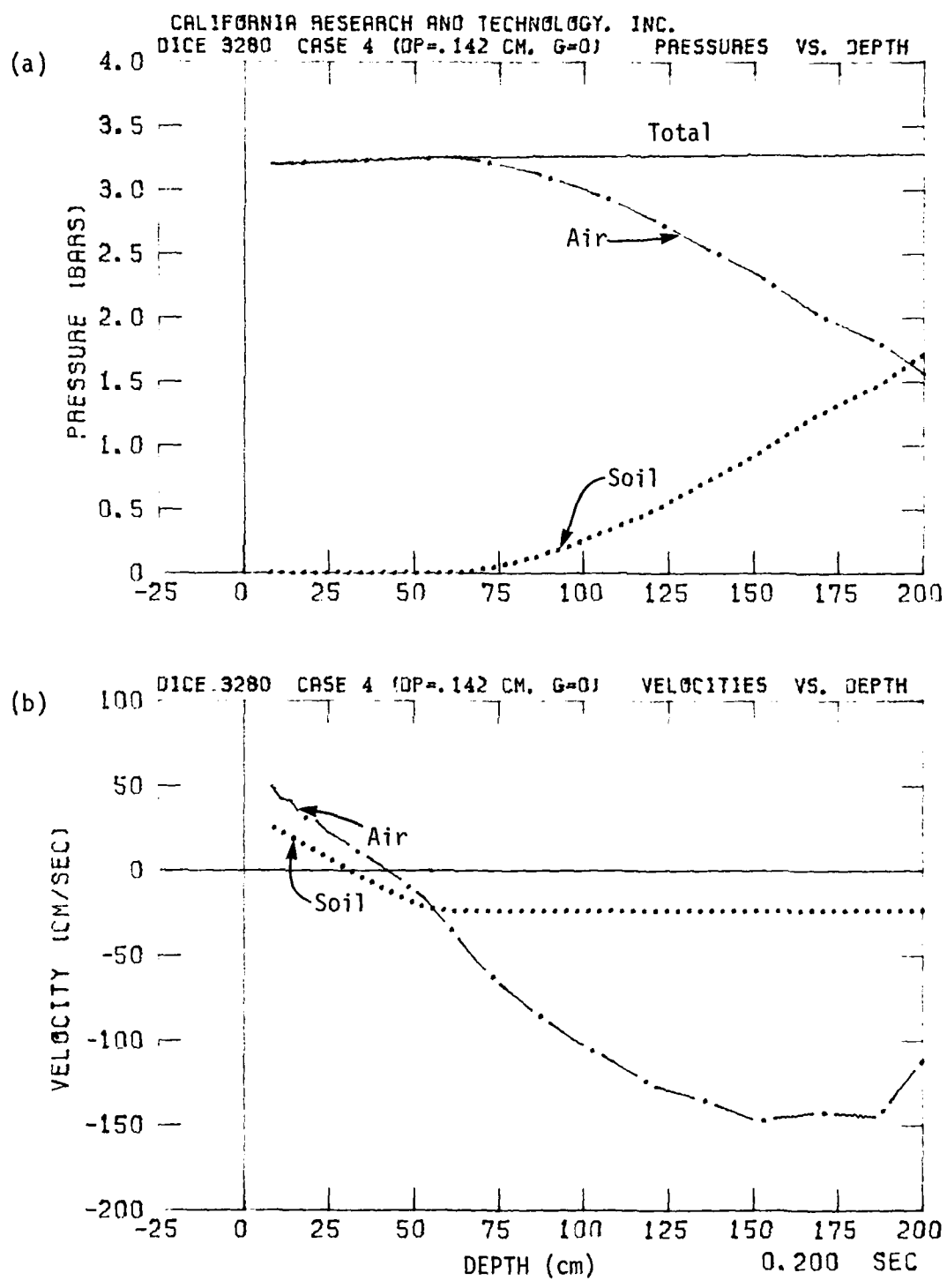


Figure 3.37. (a) Soil, Air and Total Stress Versus Depth, and
(b) Soil and Air Velocity Versus Depth at
 $t = .200$ Seconds for Case 4 ($D_p = 0.142$ cm).

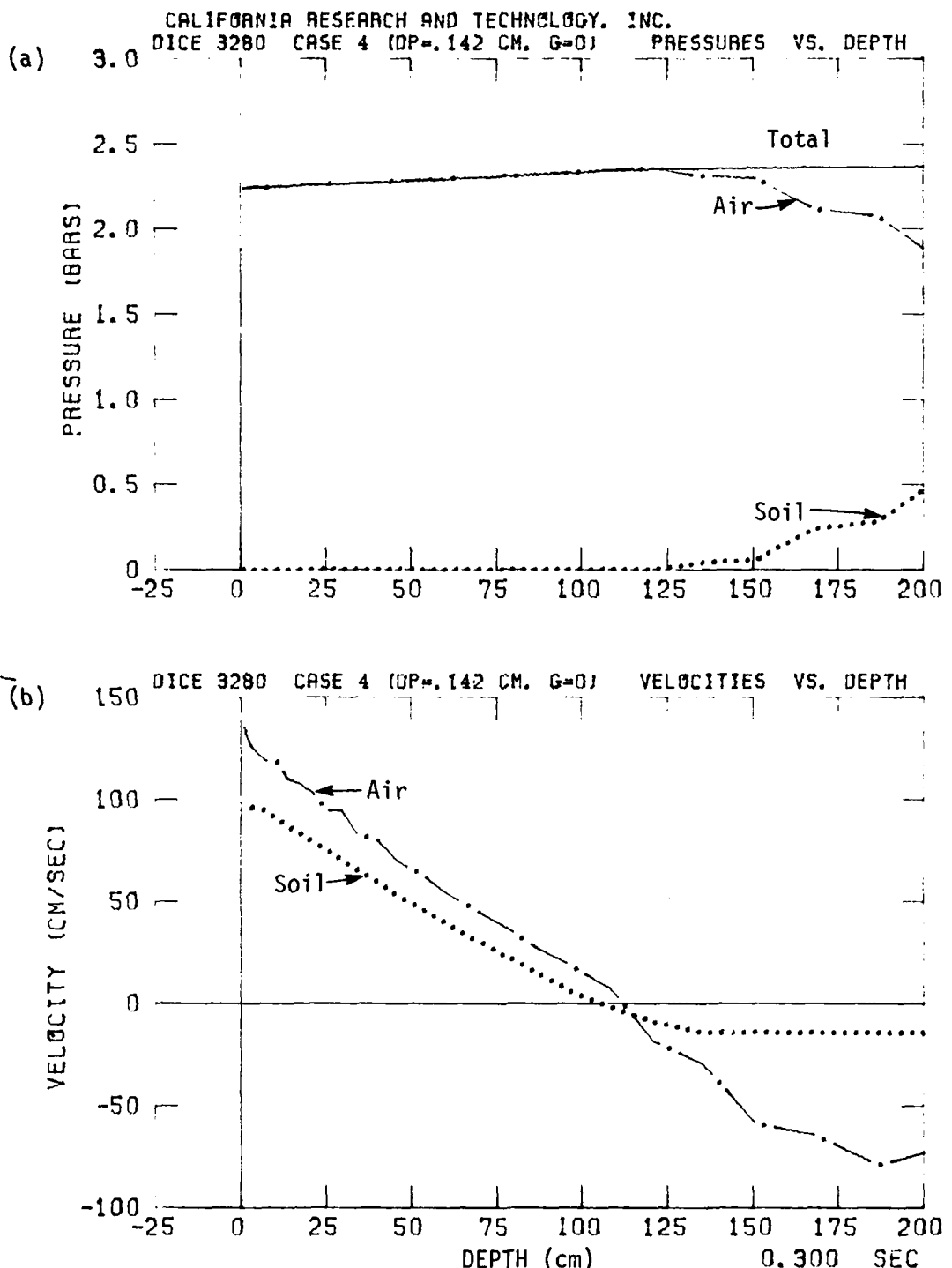


Figure 3.38. (a) Soil, Air and Total Stress Versus Depth, and
 (b) Soil and Air Velocity Versus Depth at
 $t = .300$ Seconds for Case 4 ($D_p = 0.142$ cm).

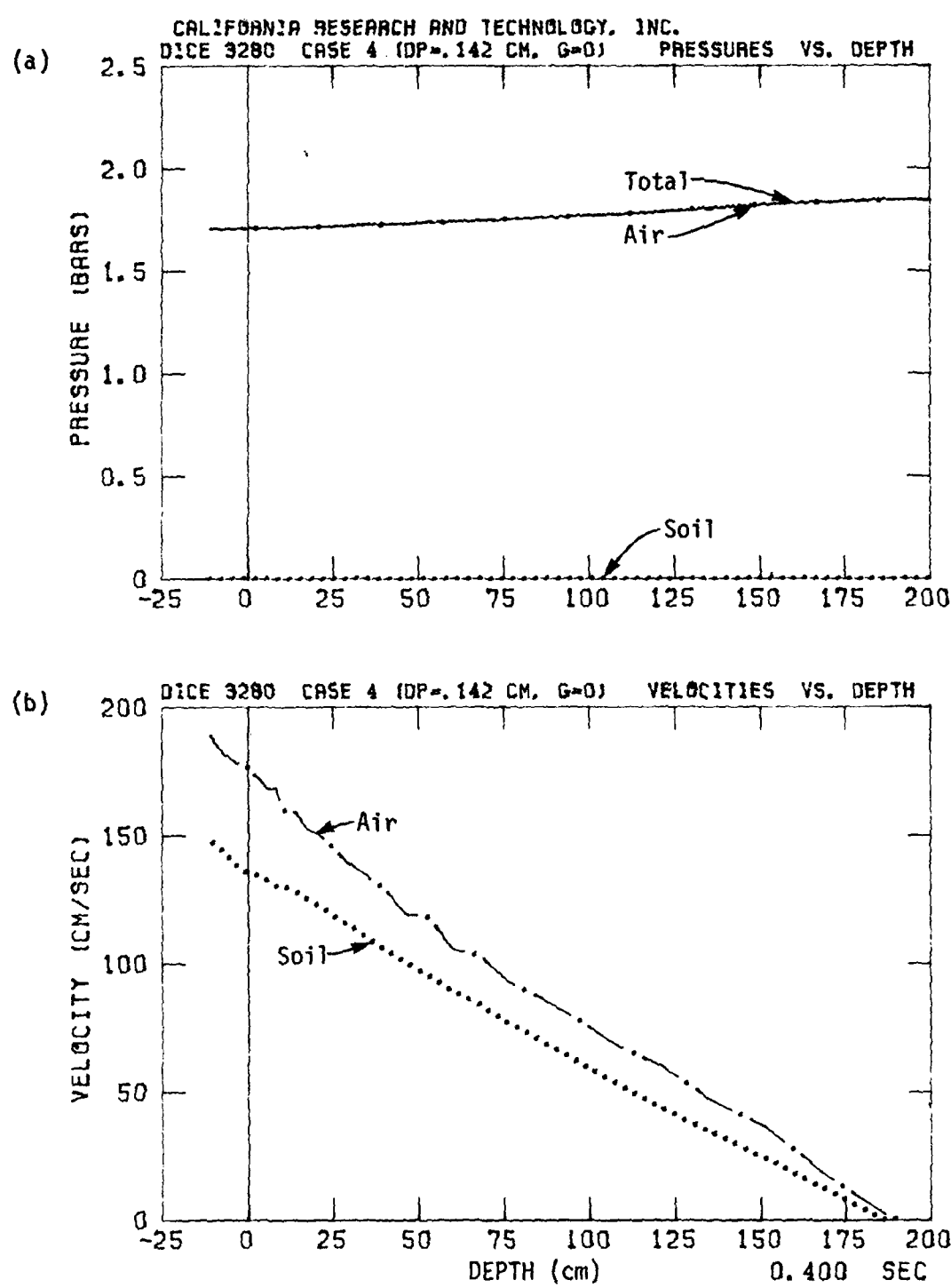


Figure 3.39. (a) Soil, Air and Total Stress Versus Depth, and
(b) Soil and Air Velocity Versus Depth at
 $t = .400$ Seconds for Case 4 ($D_p = 0.142$ cm).

By $t = .100$ s pore air pressure has increased to over 175 cm depth compared to ~75 cm depth for Case 3.

Figure 3.37 shows that by $t = .200$ s fluidization of the soil has occurred to ~60 cm depth for Case 4 compared to only ~25 cm depth for Case 3. By $t = .300$ s Figure 3.38 shows fluidization down to almost 140 cm depth.

At $t = .400$ s the entire 200 cm depth column is fluidized in Case 4, compared to ~70 cm for Case 3. Figure 3.39 shows that air is supporting the entire load; the entire fluidized column is moving upward, with peak velocity at the surface of ~190 cm/s for the air and almost 150 cm/s for the soil particles. For Case 3 both the air and soil is moving upward at ~40 cm/s at the surface.

Figure 3.40 shows the air overpressure time histories at various station depths for Case 4. Each station realizes higher peak air overpressures than in Case 3, and at earlier times. The larger particle size (and thus increased permeability) in Case 4 allows the air to permeate the soil faster and to greater depths for the same surface pressure loading. This allows the soil to be fluidized at earlier times, which is seen in the soil velocity time histories in Figure 3.41. Equation 3.2 indicates that the earlier time leads to a stronger upward pressure force at that depth for the fluidized soil in Case 4. The resulting upward soil velocities are over three times larger than calculated in Case 3.

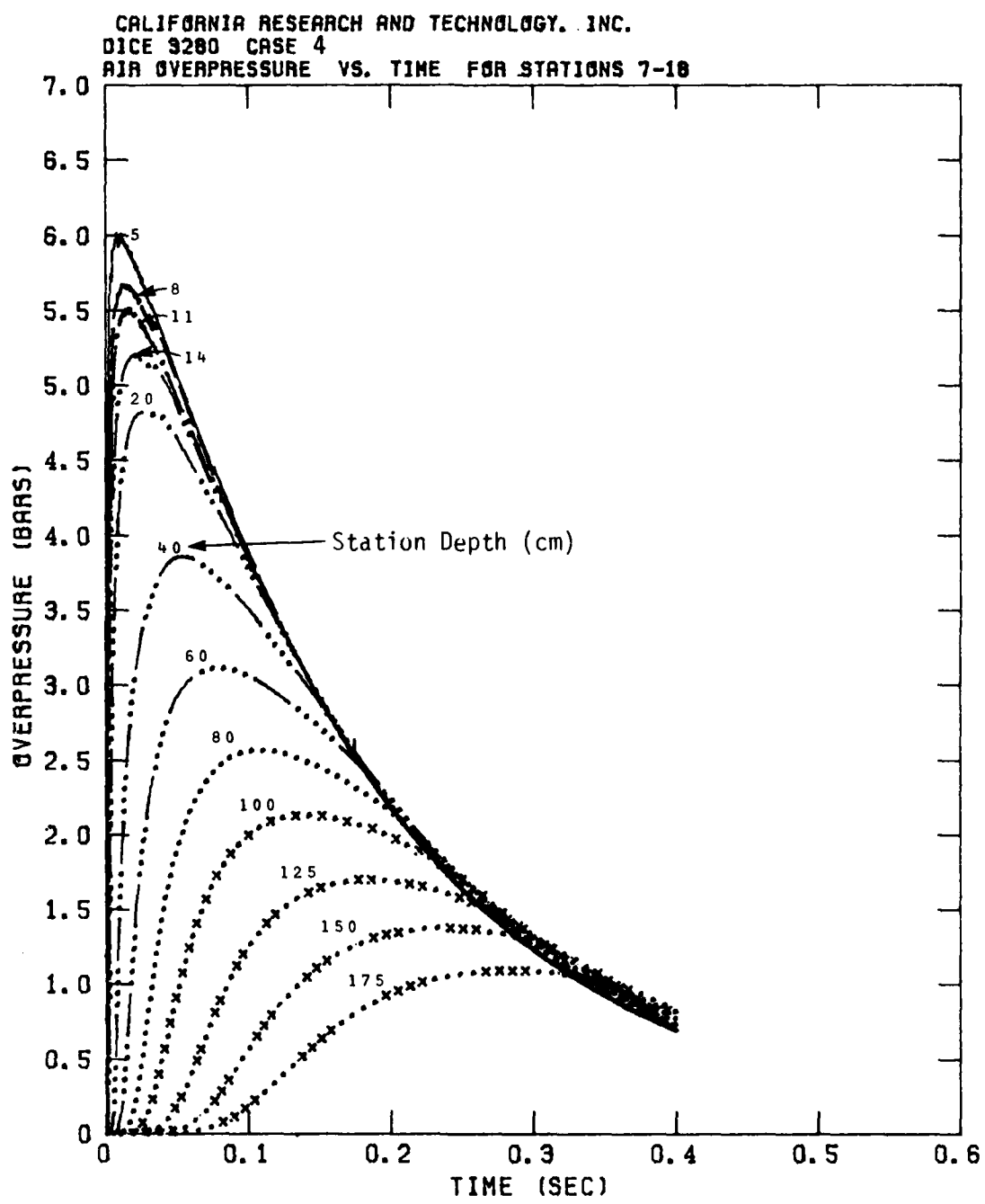


Figure 3.40. Air Overpressure Versus Time at Various Station Depths for Case 4 ($D_p = 0.142$ cm).

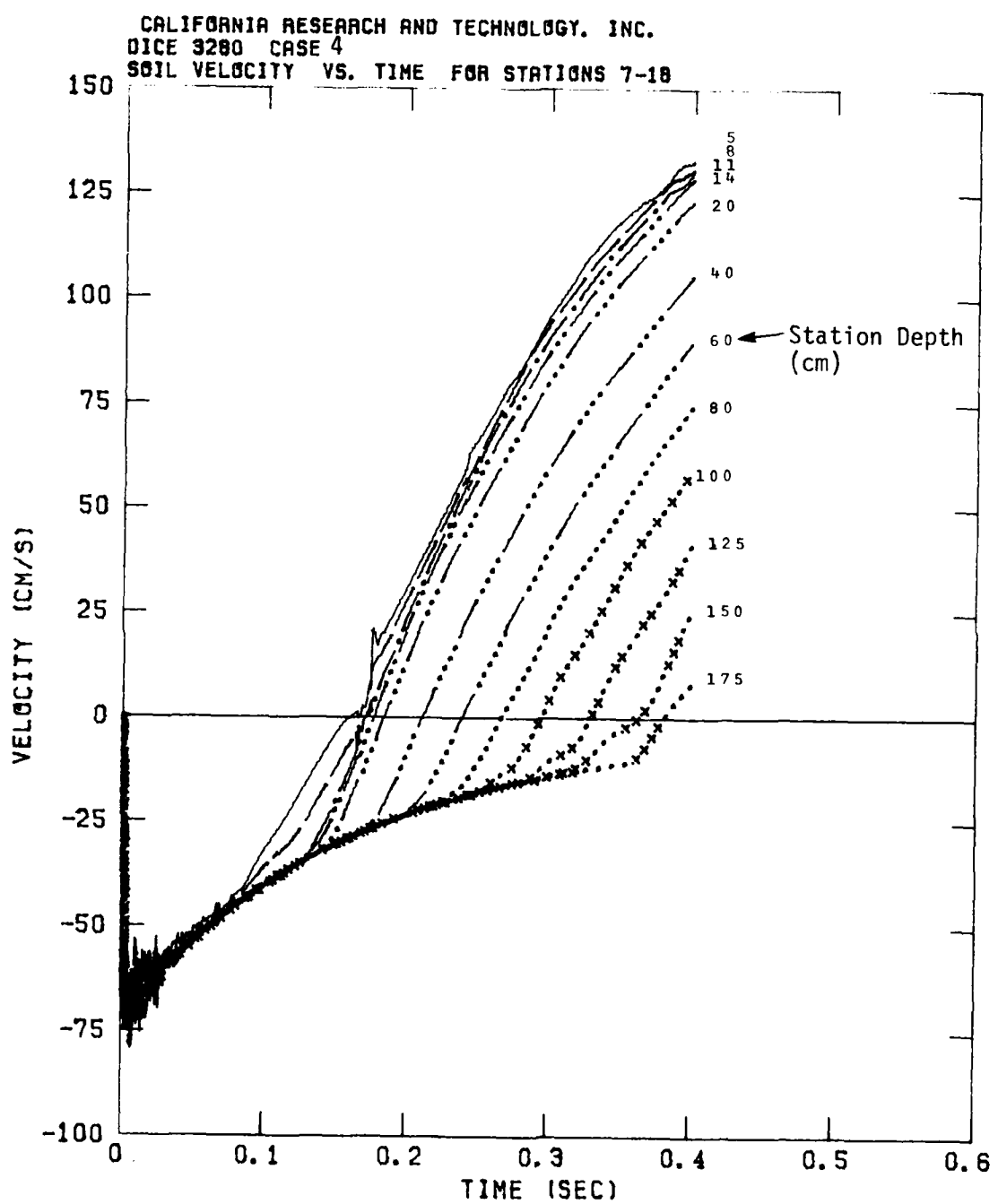


Figure 3.41. Soil Velocity Versus Time at Various Station Depths for Case 4 ($D_p = 0.142$ cm).

3.3 COMPARISON OF NUMERICAL SIMULATIONS WITH EXPERIMENTS

Although the DICE simulations were not performed in order to duplicate the laboratory experiments of Zernow *et al.*³, qualitative comparisons can be made. Both are one-dimensional in nature with similar pressure loading characteristics at the soil/sand surface.

Figure 3.2 shows the observed surface load overpressure time histories used for the two types of laboratory experiments and the overpressure loading function used in Cases 1 to 4. While the initial peak overpressure is 6.89 bars for all three, the decay in time varies. The exponential decay function used in the numerical simulation has a decay rate which puts it between the 1.36" diameter orifice experiments and the 1.78" experiments up to time $t = .600$ s. The 1.78" experiments have the fastest decay rate with a positive phase duration of ~.450 s.

In the laboratory experiments, the bottom of the sand column (~6 ft) was restricted from moving downward. In the numerical simulation a continuum boundary condition is imposed at the grid bottom (~200 cm), allowing soil and air to flow through the bottom. Case 1 showed that the unfluidized soil essentially moves downward as a rigid body (see Figure 3.17). The fluidized soil can then be thought of as moving upward relative to the unfluidized soil.

Figure 3.42a shows the time histories of the positions (or trace) of various soil marker points for Case 1. These tracer points move with the local soil velocity at any given time. Up to $t = .200$ s there is an apparent uniform downward translation of the tracer points throughout the column. The actual soil

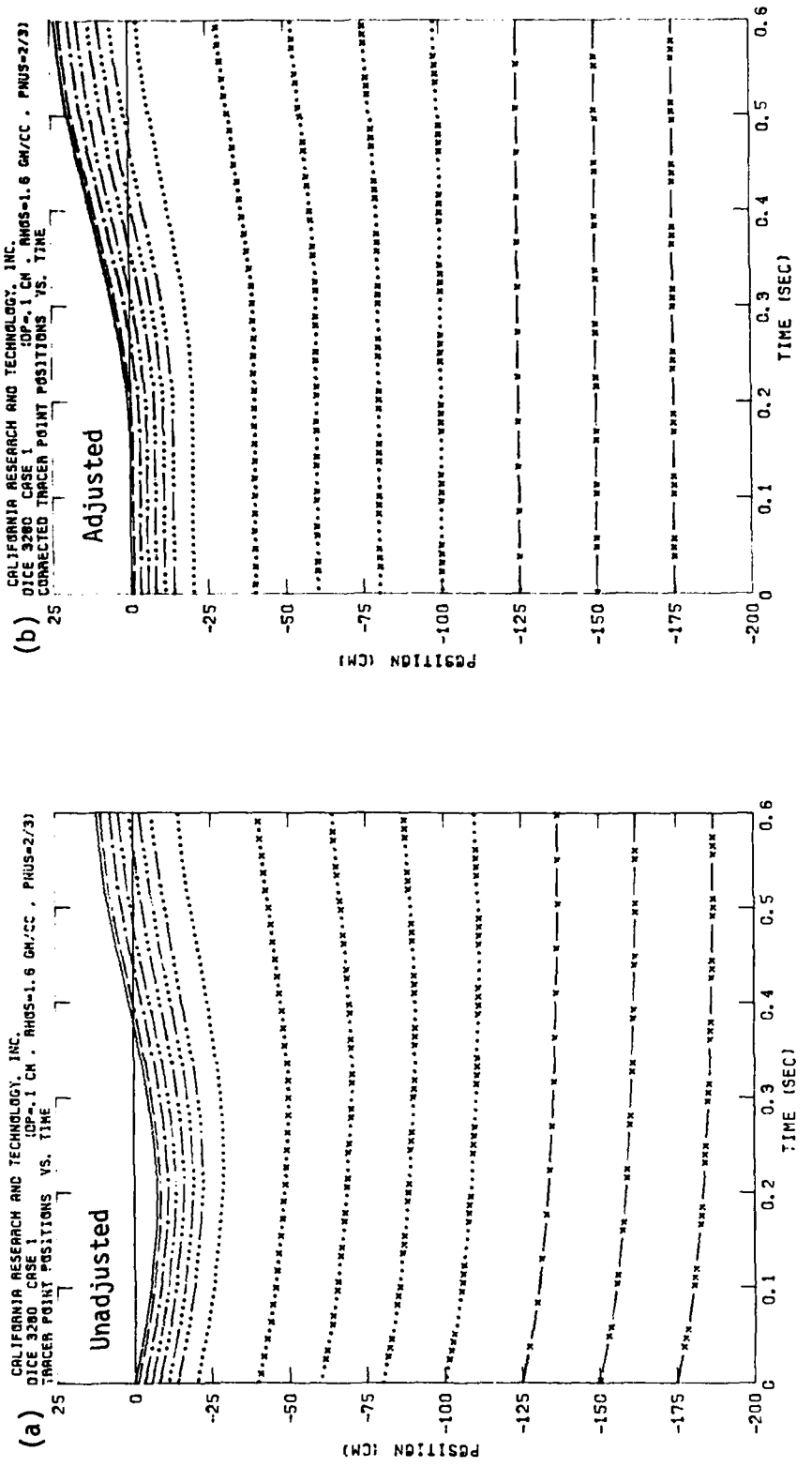


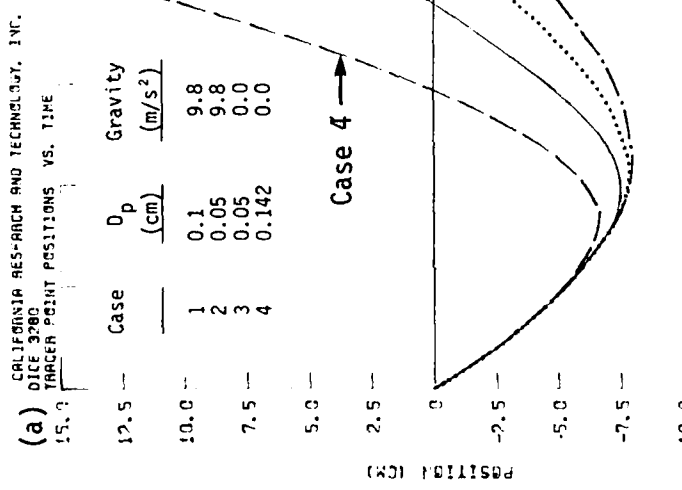
Figure 3.42. Tracer Point Positions Versus Time for DICE Case 1
($D_p = 0.1$ cm), (a) Unadjusted and (b) Adjusted, based
on -175 cm Tracer Position.

surface (represented by the tracer initially at 0 cm depth) is depressed 7.5 cm by $t = .200$ s. The depth of fluidization is 40 cm at this time; below 40 cm all tracer points have moved 8.4 cm indicating that the unfluidized soil behaves uniformly at the modeled depths.

A measure of the fluidized soil motion with respect to the unfluidized soil can be obtained by measuring the tracer point positions against the tracer point which started at 175 cm depth (and remains in essentially unfluidized soil). Figure 3.42b shows the tracer positions with the adjustment made to all tracer points. The depth to which significant motion due to fluidization occurs is now seen more clearly. The surface tracer point moves up almost 25 cm with respect to the unfluidized soil; the tracer point initially at 100 cm depth moves up ~ 2 cm.

Figure 3.43 shows the unadjusted and adjusted surface tracer point positions versus time for Cases 1 to 4. The same adjustment made in Case 1 is also made in Cases 2 and 3. For Case 4 there was no adjustment made because by $t = .400$ s the entire modeled soil column was fluidized. Figure 3.43 reveals the essential differences between the DICE cases. Increased soil permeability (due to increased characteristic particle size diameter) results in larger surface displacements due to the pore air phenomena. In the absence of gravity (Case 3) there is also increased surface displacement for a given permeability.

The adjustment of the tracer positions allows comparison of the relative motion of the fluidized soil in the calculations to the motion of the soil observed in the experiments. Figure 3.44 compares the surface displacement observed in the experiments with the adjusted surface positions calculated in Cases 1 and 2.



CALIFORNIA RESEARCH AND TECHNOLOGY, INC.
DICE 3280
CORRECTED TRACER POINT POSITIONS VS. TIME

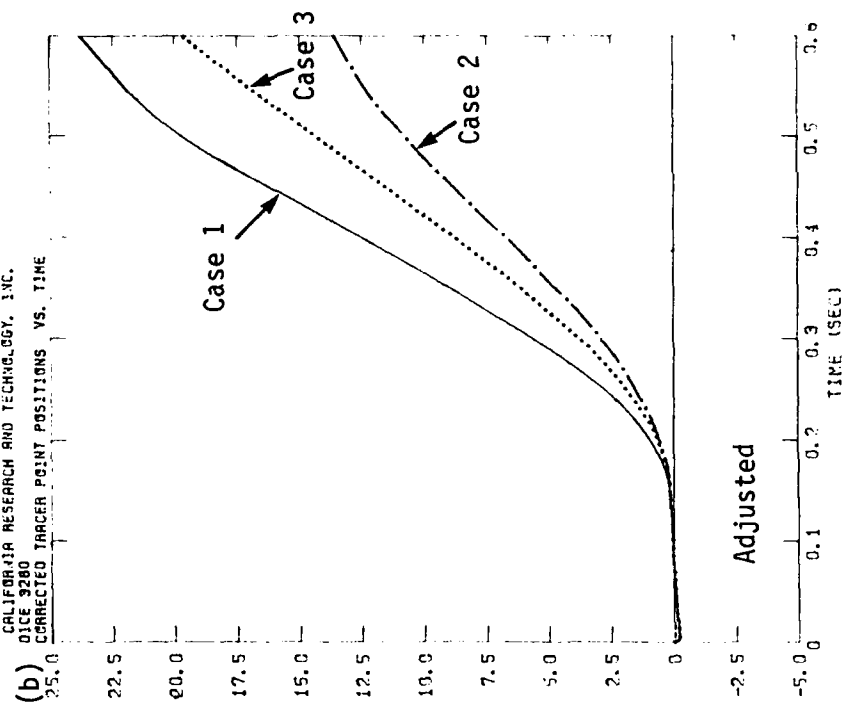


Figure 3.43. Main Surface Displacement Versus Time for DICE Cases 1 to 4, (a) Unadjusted and (b) Adjusted.

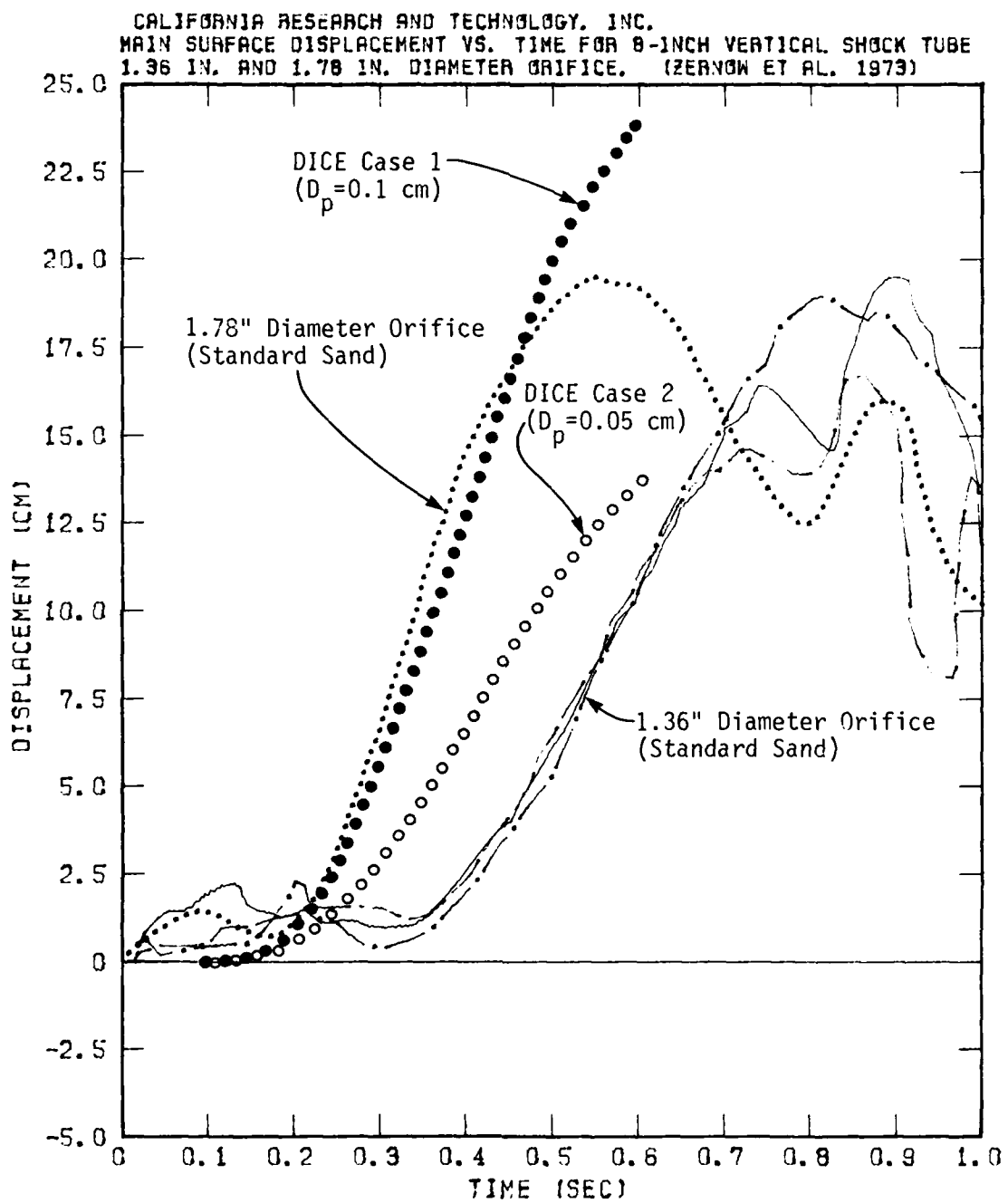


Figure 3.44. Main Surface Displacement Versus Time Observed in Experiments (Zernow et al., 1973) and Calculated by DICE (Cases 1 and 2).

Case 1 is remarkably similar to the 1.78" test. Both surfaces start to move upward at $t \sim .200$ s and maintain an approximately constant upward velocity until $t \sim .400$ s. By $t = .450$ s the 1.78" tests no longer have any surface pressure loading (see Figure 3.2). Since there is no longer a decrease in pressure at the surface, the upward pressure force is no longer sustained since the upward moving pore air serves to balance out the pore air pressure differential. Eventually the sand motion is dominated by gravity as the air can no longer drag the fluidized sand with it. By $t \sim .550$ s the sand starts to fall back. On the other hand, the surface pressure loading in Case 1 is still decaying with time having not decayed quite as rapidly at the 1.78" experiments up to $t \sim .400$ s. Thus, there is still an upward pressure force experienced by the air to at least $t \sim .600$ s.

The surface tracer for Case 2 also started to rise at $t \sim .200$ s, but maintained a smaller constant upward velocity to $t \sim .500$ s. However, the smaller displacements and velocities compared to Case 1 are indicative of a smaller sustained upward pressure force resulting from the permeability dependence of the pore-air phenomena.

The surface displacements for the 1.36" experiments do not start to rise significantly until nearly $t \sim .400$ s due to the slower rate of decay of the surface pressure loading than in the 1.78" experiments. However, the 1.36" experiments also exhibit a constant upward velocity for a substantial length of time due to the pore-air phenomena.

Figure 3.45 shows the position of the near-surface marked sand layers in time for the 1.78" experiments compared to the

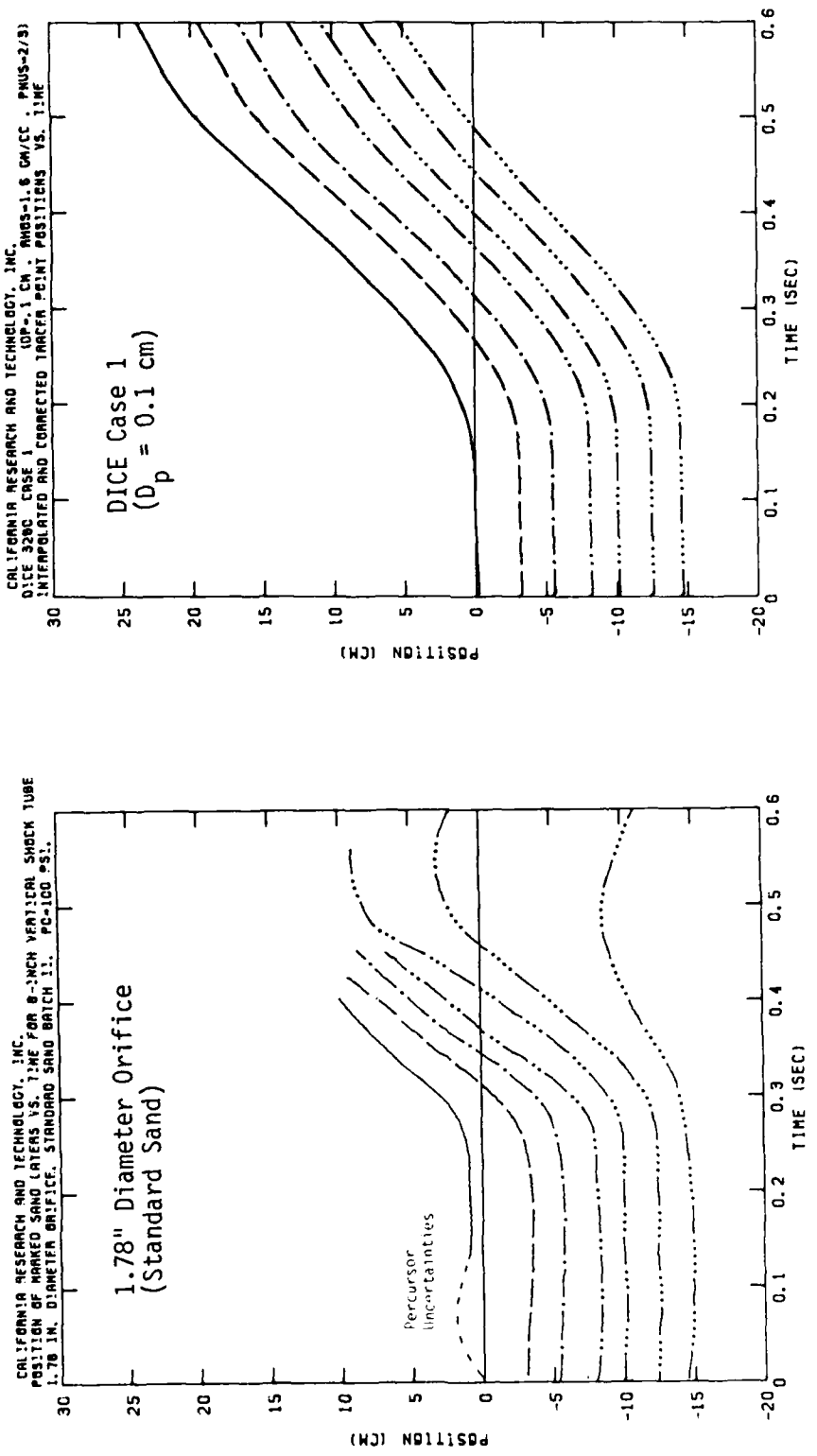


Figure 3.45. Comparison of Near-Surface Marked Sand Layer Positions Versus Time Observed in Experiments (Zernow *et al.*, 1973) and Adjusted Near-Surface Tracer Point Positions for DICE Case 1 (D_p = 0.1 cm).

equivalent adjusted soil tracer positions for Case 1. Again, there are similarities between the two sets of curves. There is a uniform rise of the near-surface layers beginning after $t = .200$ s and continuing beyond $t = .400$ s. In the 1.78" experiments the sand starts to move upward more abruptly and faster than in Case 1, probably due to the more rapid decay rate of the surface pressure loading. The deeper layers for both appear to start moving upward at slightly later times than those at the surface, indicating the downward progression of fluidization. After $t = .500$ s the soil is continuing to rise for Case 1, although decelerating, whereas in the 1.78" tests the sand is beginning to fall downward due to the end of any surface pressure loading at $t \sim .450$ s.

Figure 3.46 compares the adjusted near-surface soil tracer positions of Cases 1 and 2. Evident is the slower rise of the soil in Case 2. The surface tracers begin to move upward just after $t \sim .150$ s for both cases, while the tracer originally near 15 cm depth starts moving upward near $t \sim .200$ s for Case 1 and $t \sim .300$ s for Case 2, indicating a slower downward progression of fluidization in Case 2.

Figure 3.47 shows the time of fluidization at various depths for Cases 1 to 4. Fluidization as defined here occurs when the soil particles are supported entirely by air, i.e., the pressure associated with the particles supporting each other is zero. For Case 1 the "fluidization front" moves down through the soil at ~ 4 m/s. The fluidization front moves more slowly at ~ 2 m/s for the less permeable soil modeled in Cases 2 and 3. In Case 3, the soil at a given depth is fluidized earlier than in Case 2 because there is no initial lithostatic pressure distribution in the soil

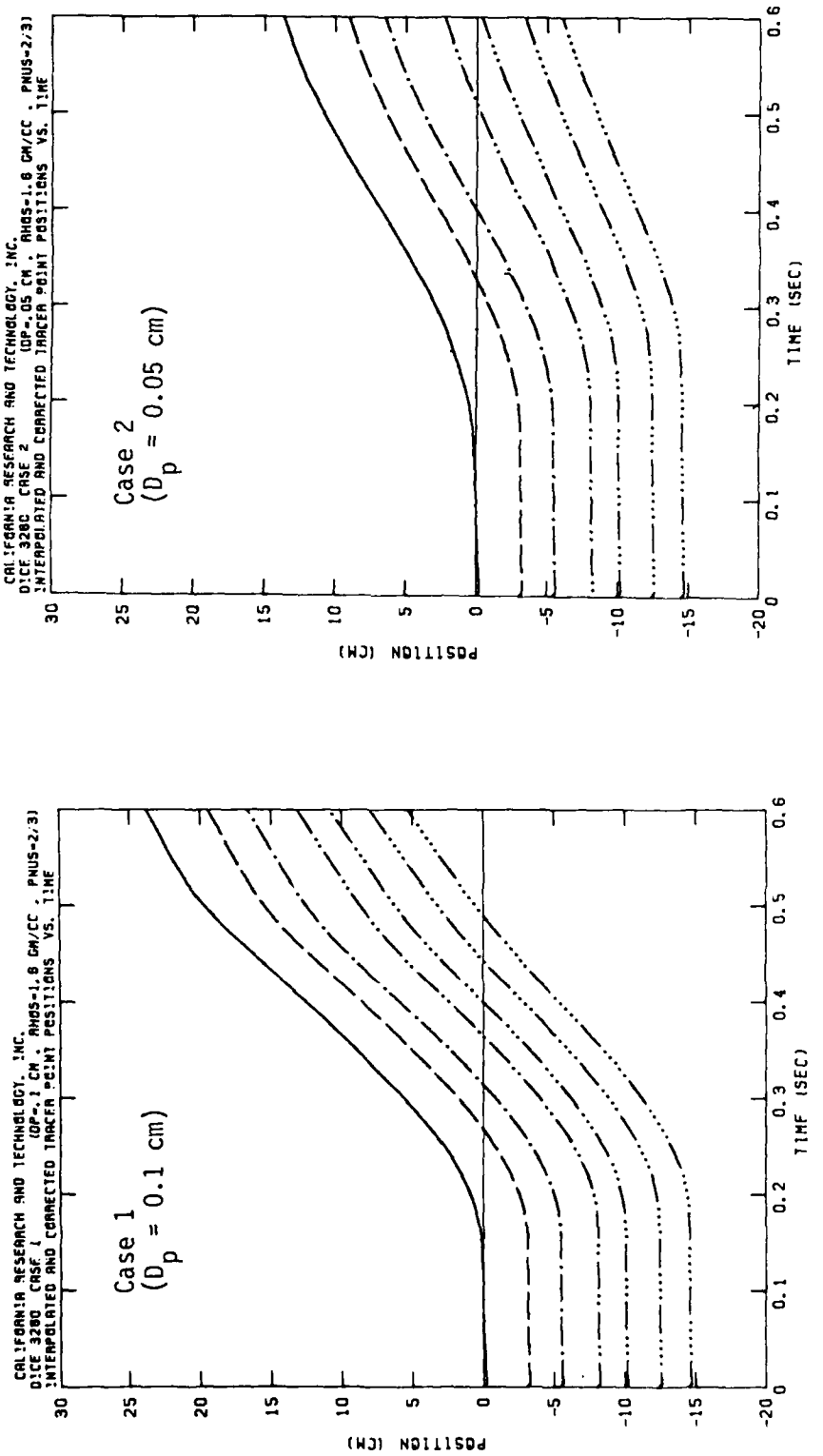


Figure 3.46. Adjusted Near-Surface Tracer Point Positions Versus Time for DICE Case 1 ($D_p = 0.1$ cm) and Case 2 ($D_p = 0.05$ cm).

CALIFORNIA RESEARCH AND TECHNOLOGY, INC.
DICE 3200 1-0 CASES 1 TO 4

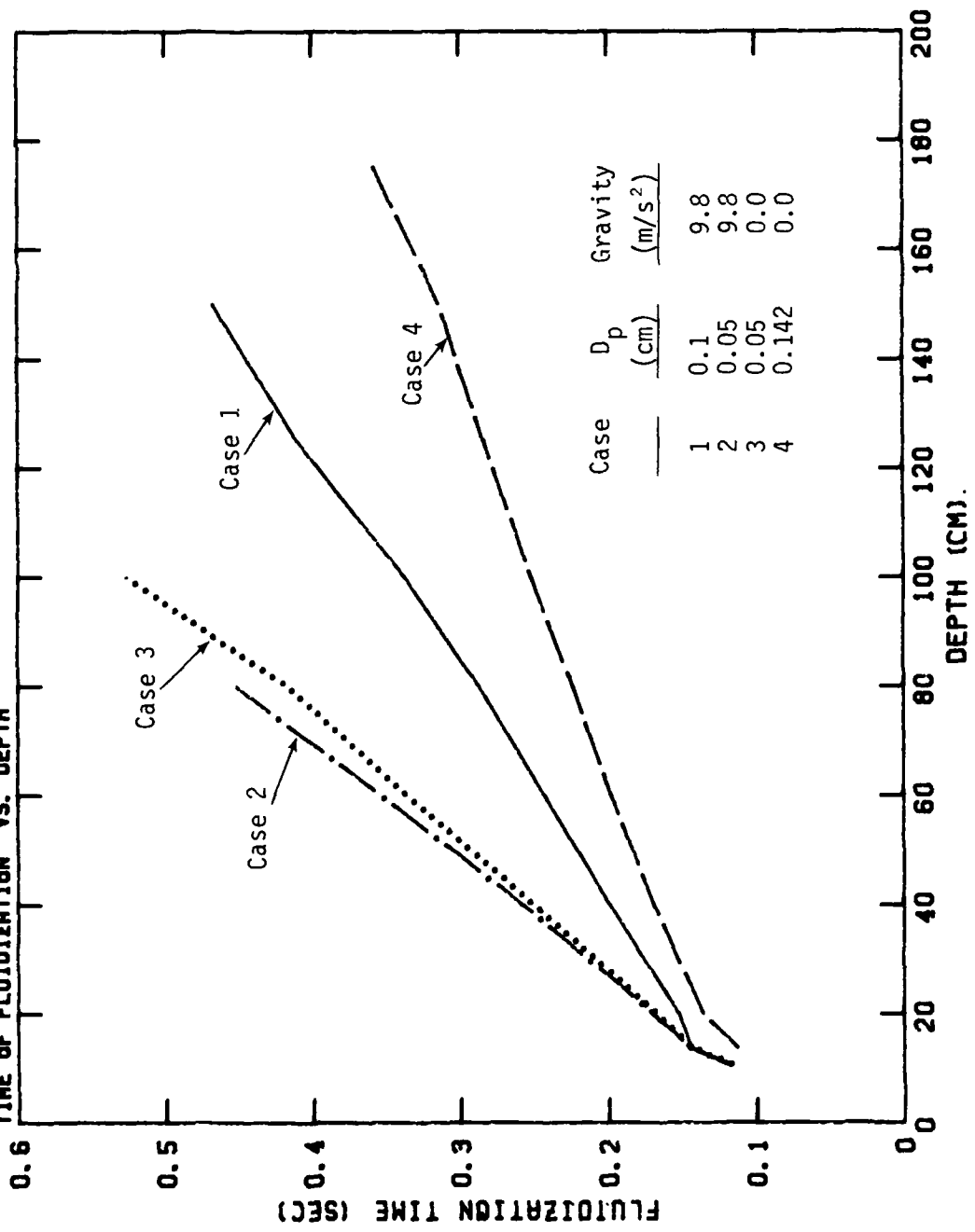


Figure 3.47. Time of Fluidization Versus Depth for DICE Cases 1 to 4.

to be overcome by the air before fluidization occurs. The highly permeable Case 4 yields a fluidization front velocity of ~7 m/s.

Some measurements of overpressure time histories were obtained at selected depths in the sand column for the laboratory experiments. The available data is summarized in Table 3.1. These can be compared with similar data from Cases 1 to 4.

Figure 3.48 shows the calculated peak air overpressures versus depth for Cases 1 to 4 compared to the observed experimental data. The more permeable modeled soils (larger particle size) allow more air to penetrate to a given depth, yielding higher overpressures. All cases display an exponential decay with depth of the peak overpressure related to the decay of the surface loading. The less permeable modeled soils yield more rapid decay rates with depth. The Case 2 and Case 3 curves indicate that down to 200 cm depth there is essentially no gravity dependence on the peak pore-air overpressure attained at a particular depth.

The 1.36" standard sand tests appear to exhibit a decay in peak overpressure similar to that of Case 1; the observed peak overpressures are slightly lower than calculated for Case 1. The observed peak overpressure for the 1.78" tests at 152 cm depth is comparatively lower than for the 1.36" standard sand tests at 146 cm depth. With the more rapid decay (and thus shorter duration) of the surface pressure loading for the 1.78" tests, less air is forced into the sand column than for the longer duration 1.36" tests over an equivalent length of time. Less air will result in lower peak air overpressures at a given depth for sands of equivalent permeability and porosity.

CALIFORNIA RESEARCH AND TECHNOLOGY, INC.

DICE 9280
PEAK OVERPRESSURE VS. DEPTH

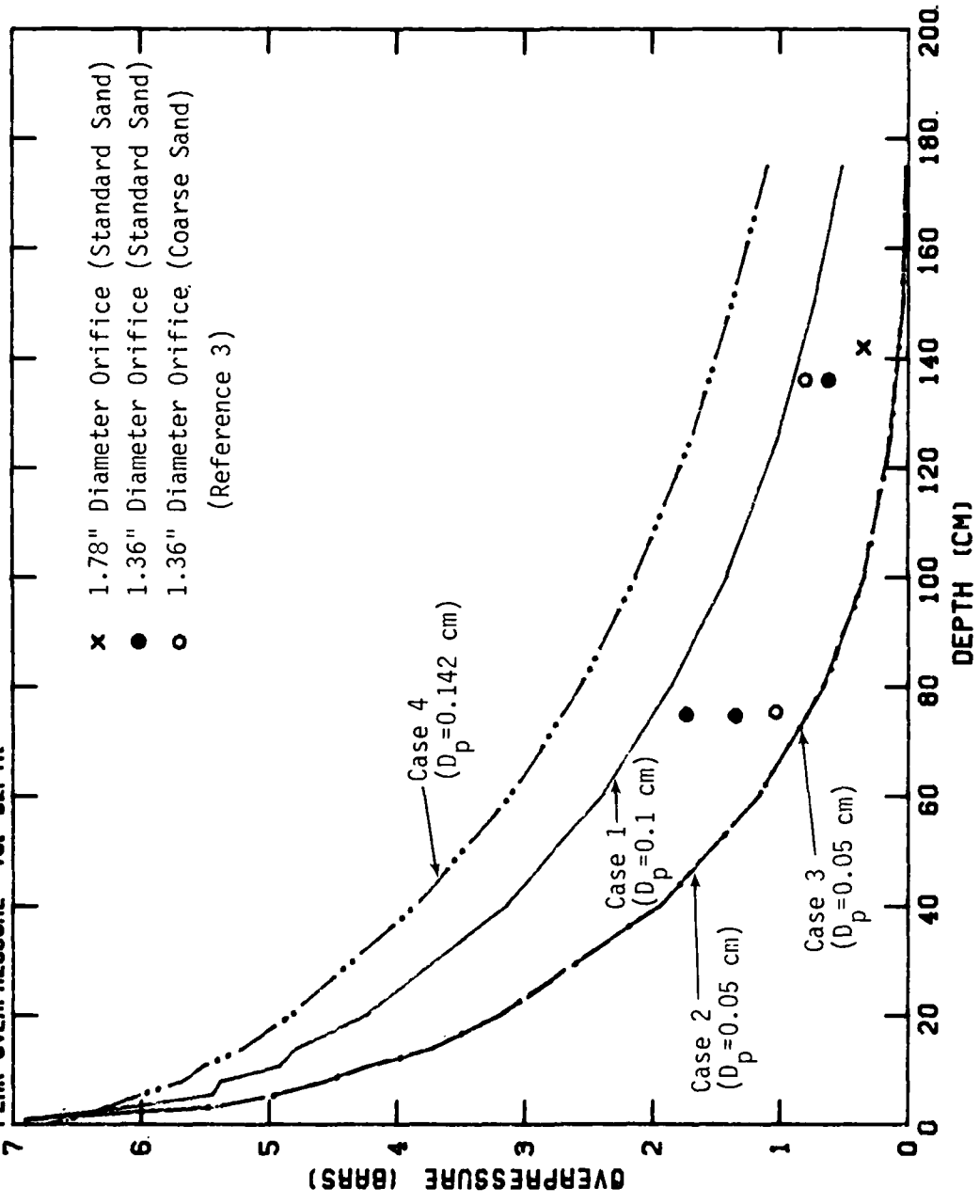


Figure 3.48. Comparison of Calculated (DICE Cases 1 to 4) and Observed (Zernow *et al.*, 1973) Peak Overpressure at Various Depths in the Sand Column.

For the same surface pressure loading the peak air overpressures are expected to be larger for the more permeable coarse sand than for the standard sand. At the 146 cm depth this is true. The 83 cm depth data point for coarse sand appears to be anomalous in this regard, and is left unexplained by Zernow *et al.*³

Related to this anomaly could be the drastically reduced main surface displacement for the coarse sand experiment when compared to the standard sand (see Figure 3.4). The DICE calculations assume homogeneous soil mixtures whose permeabilities are determined by the soil porosity and the characteristic particle size diameter. The calculations showed that increased permeabilities result in increased surface lofting as well as higher peak pore-air overpressures at a given depth. In the coarse sand experiments, however, a breakdown in the homogeneous sand lattice during the surface pressure loading or during subsequent soil expansion could cause relatively large diameter air channels to develop. This would allow the pore-air to vent more readily and directly upward through the channels. Thus, there would be a decrease in the sustained upward internal force (drag) available to loft the sand upward.

Figure 3.49 shows the calculated peak air overpressure arrival times versus depth for Cases 1 to 4 and the observed experimental data from Table 3.1. Figure 3.50 compares the times at which the air overpressure first achieves 10% of its peak at a particular depth. The more permeable modeled soils allow air to travel faster down through the soil, yielding earlier arrival times for both the peak overpressure and 10% level. The slope of the peak arrival time versus depth for each case is remarkably similar to those in Figure 3.47 which shows the soil fluidization

CALIFORNIA RESEARCH AND TECHNOLOGY, INC.

DICE 3200

TIME OF ARRIVAL OF PEAK OVERPRESSURE VS. DEPTH

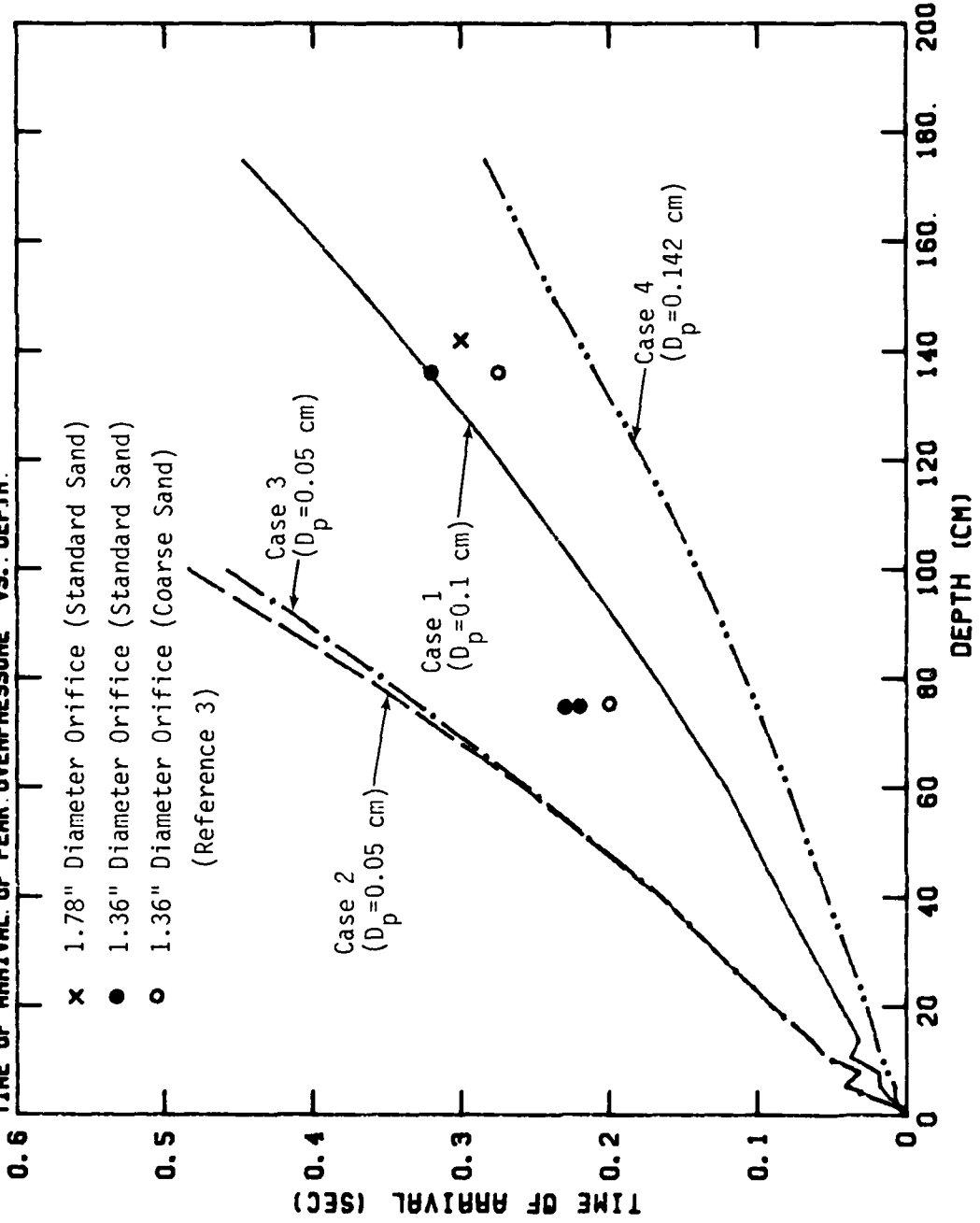


Figure 3.49. Comparison of Calculated (DICE Cases 1 to 4) and Observed (Zernow *et al.*, 1973) Time of Arrival of Peak Overpressure at Various Depths in the Sand Column.

Table 3.1. Summary of Overpressure Versus Time Data
at Selected Depths for 8" Diameter Shock
Tube Experiments (Zernow *et al.*, 1973)

| Experiment Type | Depth (cm) | Peak Overpressure (bars) | Peak Arrival Time (sec) | Arrival Time of 10% of Peak (sec) |
|-------------------------------|------------|--------------------------|-------------------------|-----------------------------------|
| 1.78" Orifice (Standard Sand) | 152.4 | .34 | .30 | .140 |
| 1.36" Orifice (Standard Sand) | 83.8 | 1.35 | .23 | .057 |
| | 83.8 | 1.73 | .22 | .065 |
| | 146.3 | .62 | .32 | .120 |
| 1.36" Orifice (Coarse Sand) | 83.8 | 1.03 | .20 | .056 |
| | 146.3 | .81 | .275 | .100 |

CALIFORNIA RESEARCH AND TECHNOLOGY, INC.

DICE 9280

TIME OF ARRIVAL OF 10% PEAK OVERPRESSURE VS. DEPTH

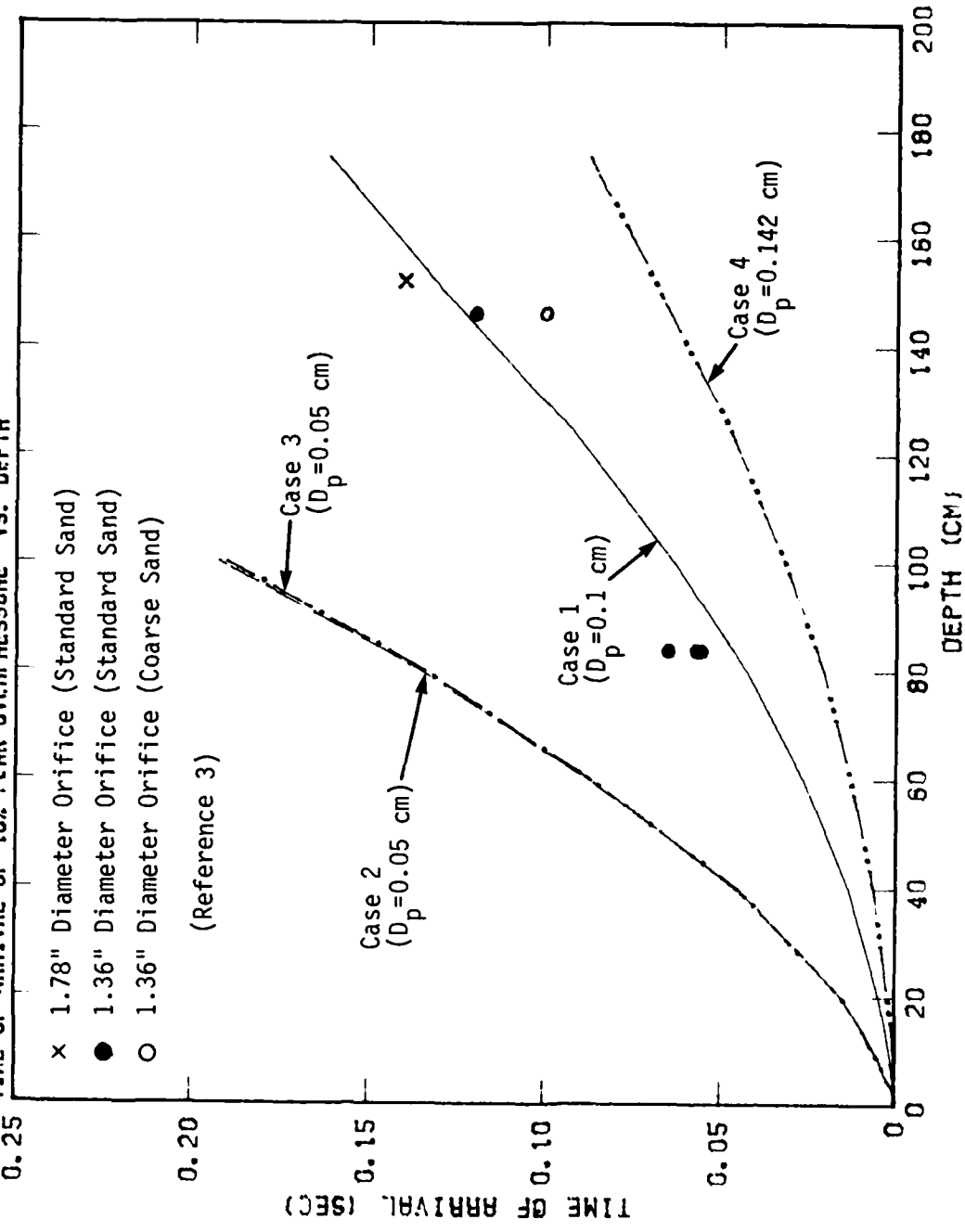


Figure 3.50. Comparison of Calculated (DICE Cases 1 to 4) and Observed (Zernow et al., 1973) Time of Arrival of 10% Level of Peak Overpressure at Various Depths in the Sand Column.

time versus depth. For Case 1 the peak air overpressure appears to move down through the soil at ~4 m/s. The less permeable soils of Cases 2 and 3 yield ~2 m/s, while the highly permeable Case 4 yields ~6 to 7 m/s. For each case there is also a delay of ~.080 to .120 s after the arrival of the peak overpressure at a given depth until soil fluidization begins at that depth. The 1.36" experiments also yield earlier arrival times for the more permeable coarse sand as compared to the standard sand. The data fall around the curves for Case 1 but the slopes of lines through the data would indicate faster velocities for the peak overpressure and 10% level.

SECTION 4
MISERS BLUFF II-2

4.1 EXPERIMENTAL RESULTS

The MISERS BLUFF II-2 experiment involved the simultaneous detonation of six high-explosive charges (120 ton) forming a hexagon 100 m on a side. Figure 4.1 shows the experimental configuration and the measurement gauge locations for data used in this report. Details of the experiment can be found in Reference 1.

Figure 4.2 shows the overpressure time history (after detonation) measured at various azimuthal angles, all 25 m from the center of the hexagon. Three separate peaks are evident at each angle, although not as distinct at 0° . The time histories for the two gauges at 30° and 210° are very similar. By $t = .150$ s the positive phase has ended for each, and a small negative phase is sustained until $t \sim .400$ s.

Figure 4.3 shows various vertical velocity time histories of ground motion gauges originally at 0.5 m depth and 25 m radius. The azimuthal angles are different from those for the overpressure time histories. Figure 4.4 shows the corresponding vertical displacement of each gauge as a function of time. The velocities and displacements are very similar for each gauge. Up to $t \sim .125$ s the ground motion is downward, corresponding to the airblast pressure load pushing down at the surface. Peak downward velocities are 5 to 10 m/s. From $t \sim .125$ s to $t \sim .450$ s the ground motion is upward, with peak velocities of ~ 5 m/s at $t \sim .300$ s. Peak upward displacements of ~ 1 m are achieved. This

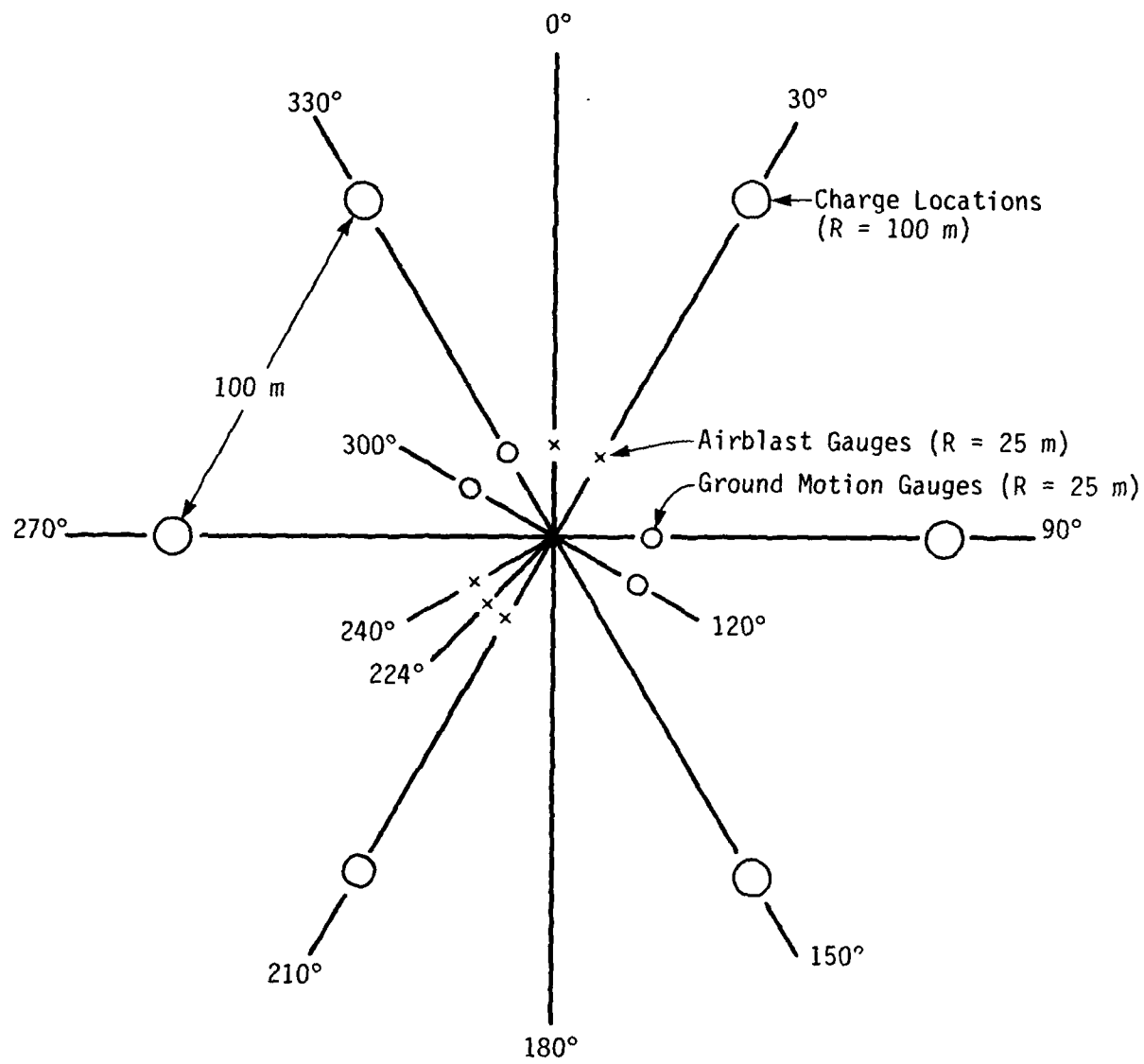


Figure 4.1. Location of Charges and Various Measurement Gauges in MISERS BLUFF II-2.

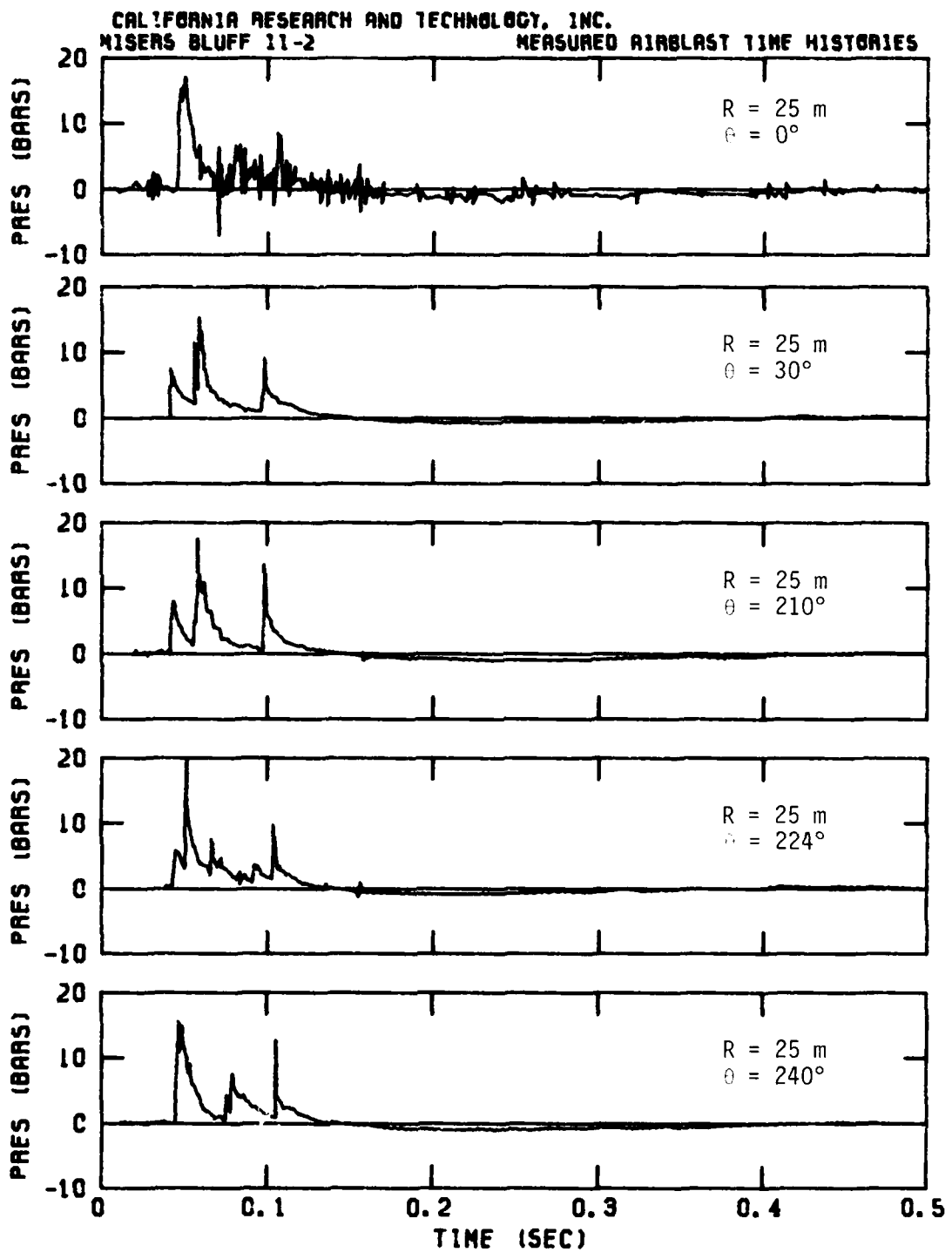


Figure 4.2. Airblast Time Histories Measured at 25 m Radius
in MISERS BLUFF II-2.

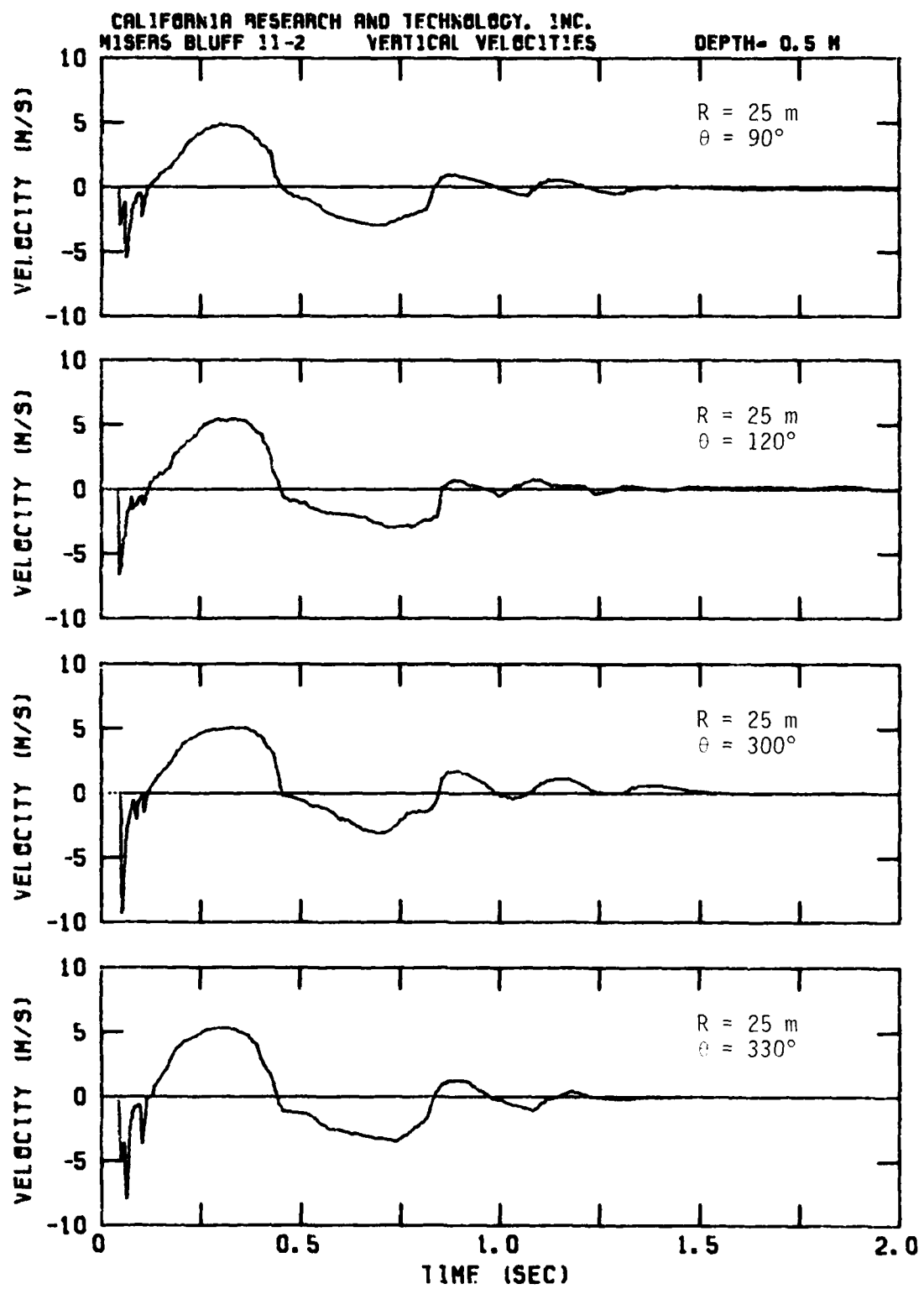


Figure 4.3. Vertical Velocities Measured in MISERS BLUFF II-2 from Ground Motion Gauges Originally at 0.5 m Depth.

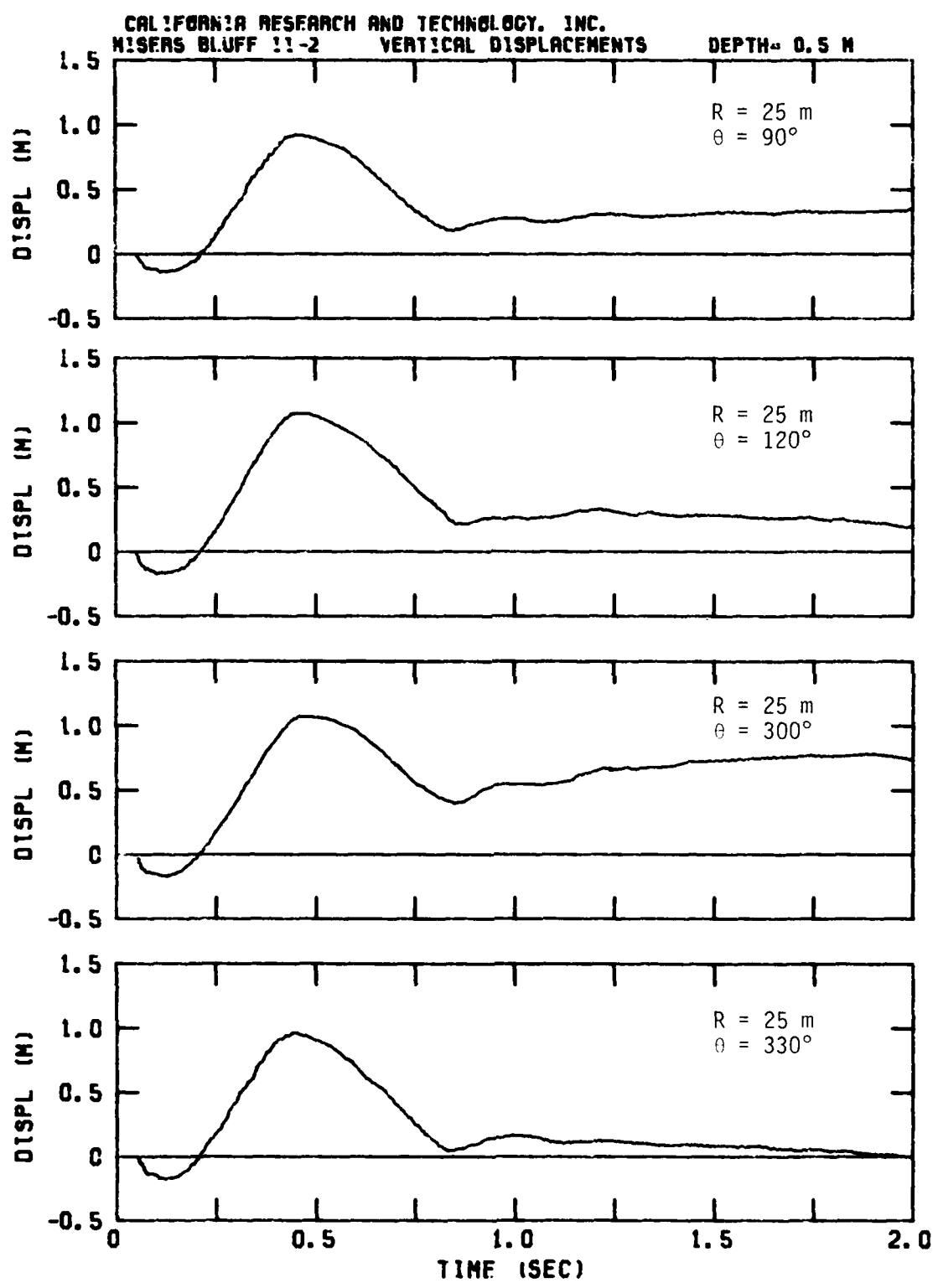


Figure 4.4. Vertical Displacements Measured in MISERS BLUFF II-2 from Ground Motion Gauges Originally at 0.5 m Depth.

sustained upward motion is similar to the motion seen in the laboratory experiments described in Section 3; however, now the upward velocities are associated with negative pressures. From $t \sim .450$ s to $t \sim .850$ s the ground motion is again downward, after which time the velocities oscillate about zero.

4.2 NUMERICAL SIMULATION

A numerical calculation (Case 5) was performed with the multiphase DICE code in order to examine the apparent pore-air phenomenology seen in the ground motion data of MISERS BLUFF II-2. The calculation was designed using one-dimensional (1-D) planar geometry in the vertical direction, with a surface overpressure loading function defined by an approximation to the airblast measured at 25 m radius from the center of the array.

Figure 4.5 shows the overpressure loading function used in Case 5, along with the airblast measured at 30° and 210° for comparison. There are three distinct peaks which occur in the loading function before $t \sim .110$ s after detonation; the magnitudes are 6.5 bars at $t = .045$ s, 12.8 bars at $t = .063$ s, and 7.7 bars at $t = .102$ s. The measurements showed larger peaks occurring a couple of milliseconds earlier than the assumed loading function. A negative phase occurs after $t \sim .150$ s with overpressures reaching -0.8 bars. By $t \sim .400$ s the overpressure loading function becomes zero.

Figure 4.6 shows the recommended calculational soil profiles from Reference 11 developed to characterize the subsurface layering beneath the 120° and 300° radials of MISERS BLUFF II-2. Figure 4.7 shows the same for the single charge event MISERS BLUFF II-1, held ~400 m away from event 2. It is this profile

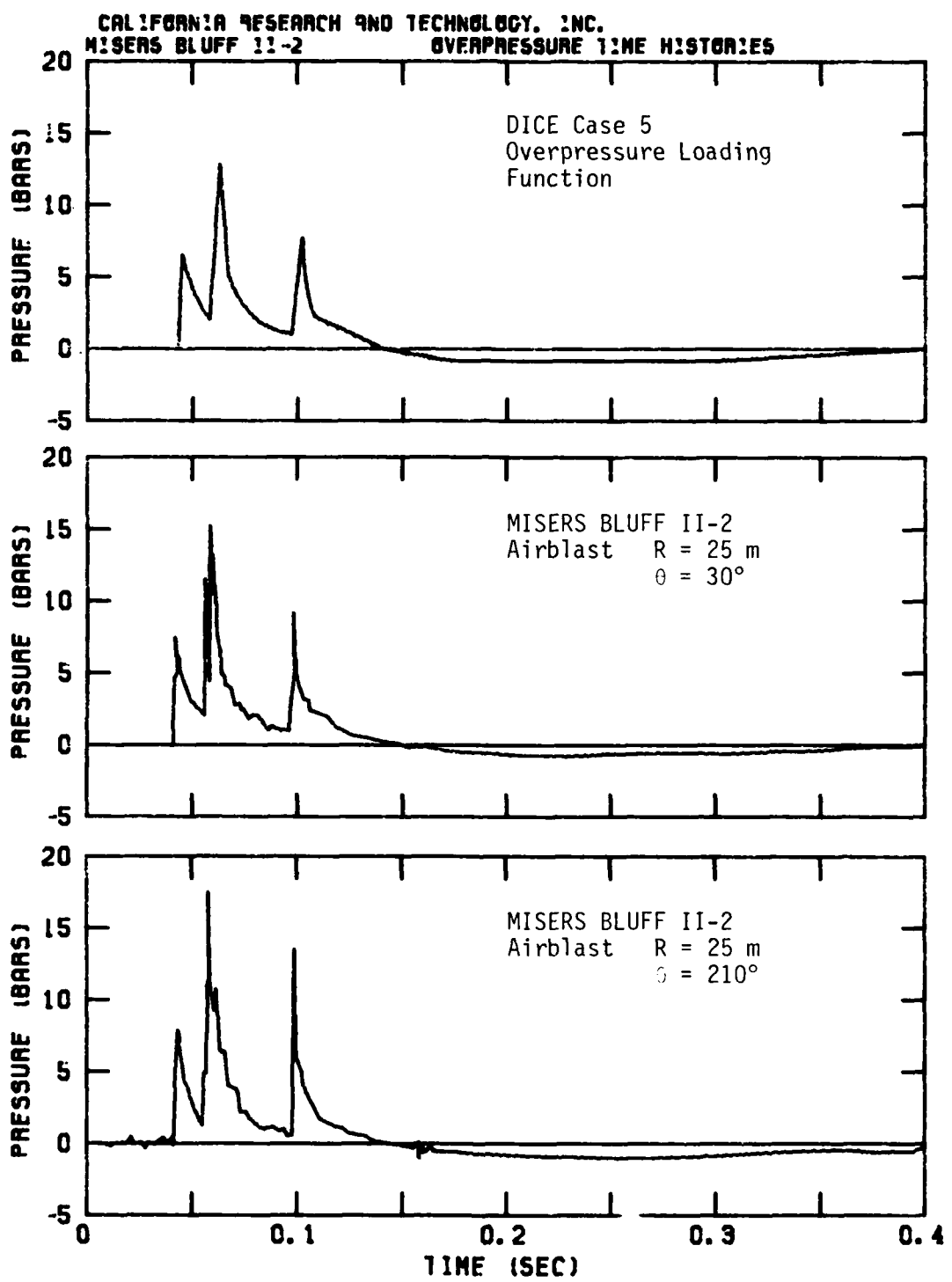
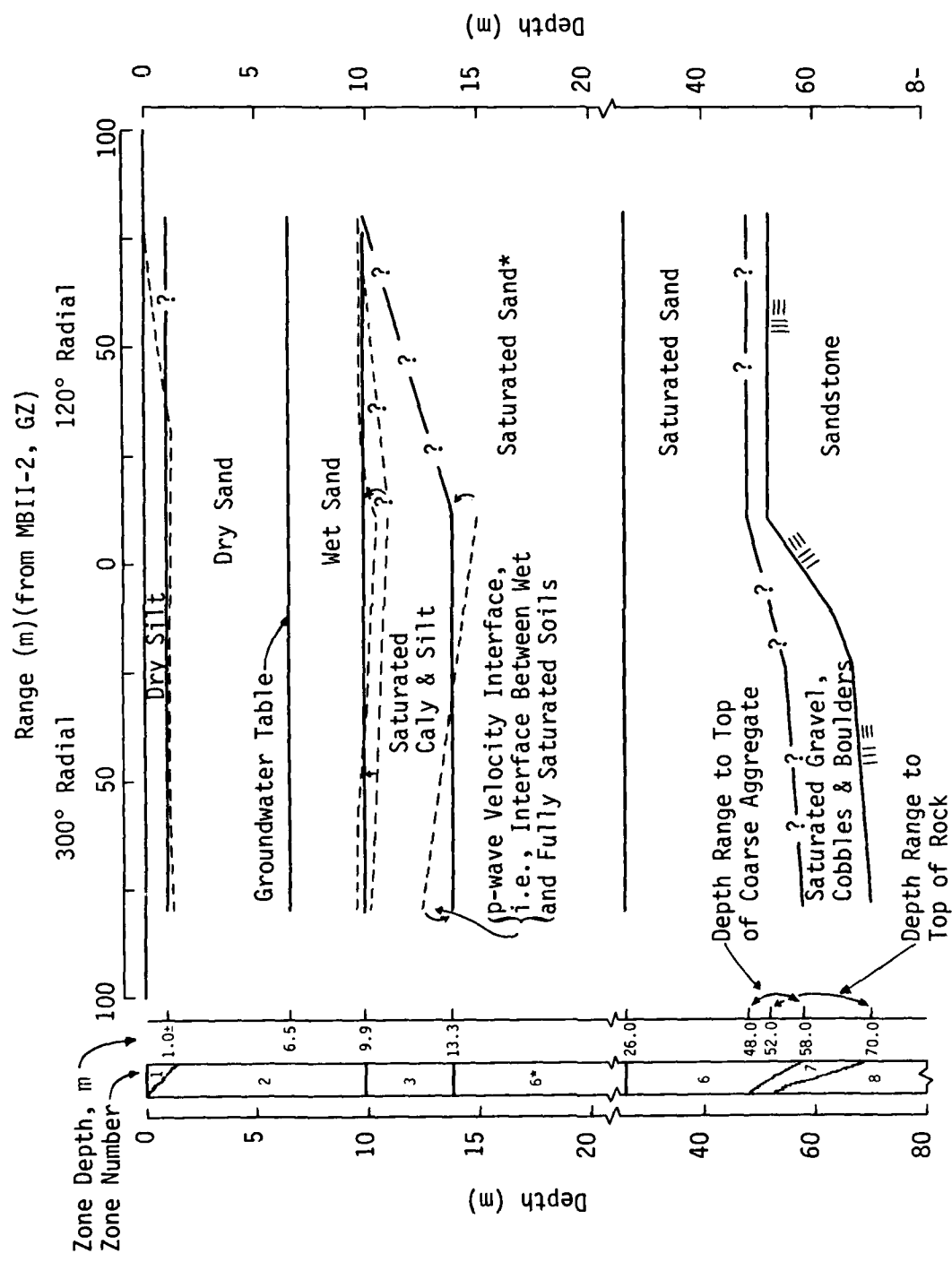


Figure 4.5. Overpressure Loading Function Versus Time Used in DICE Case 5 and Airblast Time Histories Observed in MISERS BLUFF II-2.



*Seismic (and uniaxial compressibility) properties of Zone 5; strength properties of Zone 6.

Figure 4.6. Calculational Profile for the 120° and 300° Radials at MISERS BLUFF II-2 (Reference 11).

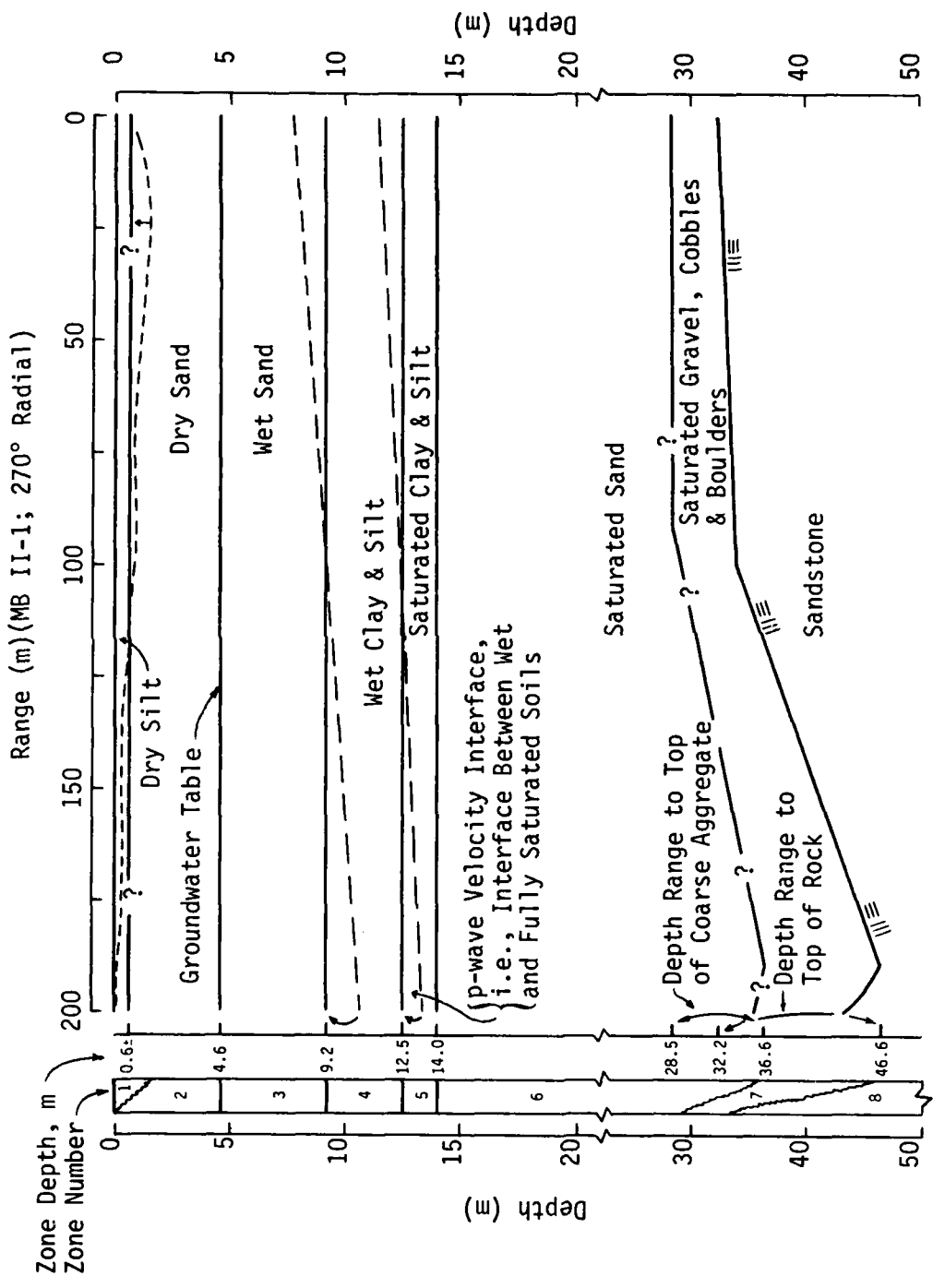


Figure 4.7. Calculational Profile for the 270° Radial at MISERS BLUFF III-1 (Reference 11).

which was used in determining the soil layer thicknesses used in Case 5.

Figure 4.8 shows the 1-D grid used in the calculation. Three soil layers are used to model the site. The top soil layer consists of five 0.12 m cells. Each subsequent cell in Layer 2 is 10% larger than the cell above it, down to 7.35 m depth. Thereafter the cells are uniform (0.73 m) down through Layer 3.

Table 4.1 defines the MISERS BLUFF II-2 material properties used to model each of the three soil layers. Each soil layer is modeled using only one characteristic particle size, which is estimated from data found in Reference 12. The permeability model discussed in Section 2.3 yields permeability as a function of porosity and particle size. The remaining material properties are from Reference 11. The initial densities increase with depth, with the corresponding initial porosities decreasing with depth from 44% to 1%. In addition, hysteresis effects are included and the modeling is described on Table 4.1. The loading and unloading constrained moduli for each layer were determined from the stress-strain curves in Reference 11.

The initial modeled permeabilities for Case 5 are much smaller than in Cases 1 to 4. In Cases 1 to 4 the initial permeabilities were in the 10^2 - 10^3 Darcy range. In Case 5, the initial permeabilities are different in each modeled soil layer - $k \sim .04$ Darcy for the top layer, $k \sim 70$ Darcy for Layer 2 and $k \sim .003$ Darcy for Layer 3. One of the results of a decrease in permeability was seen in the Case 3 and Case 4 comparison, which demonstrated that the air would permeate the soil slower and to shallower depths for the same surface pressure loading and equivalent porosities. In effect, the internal interaction

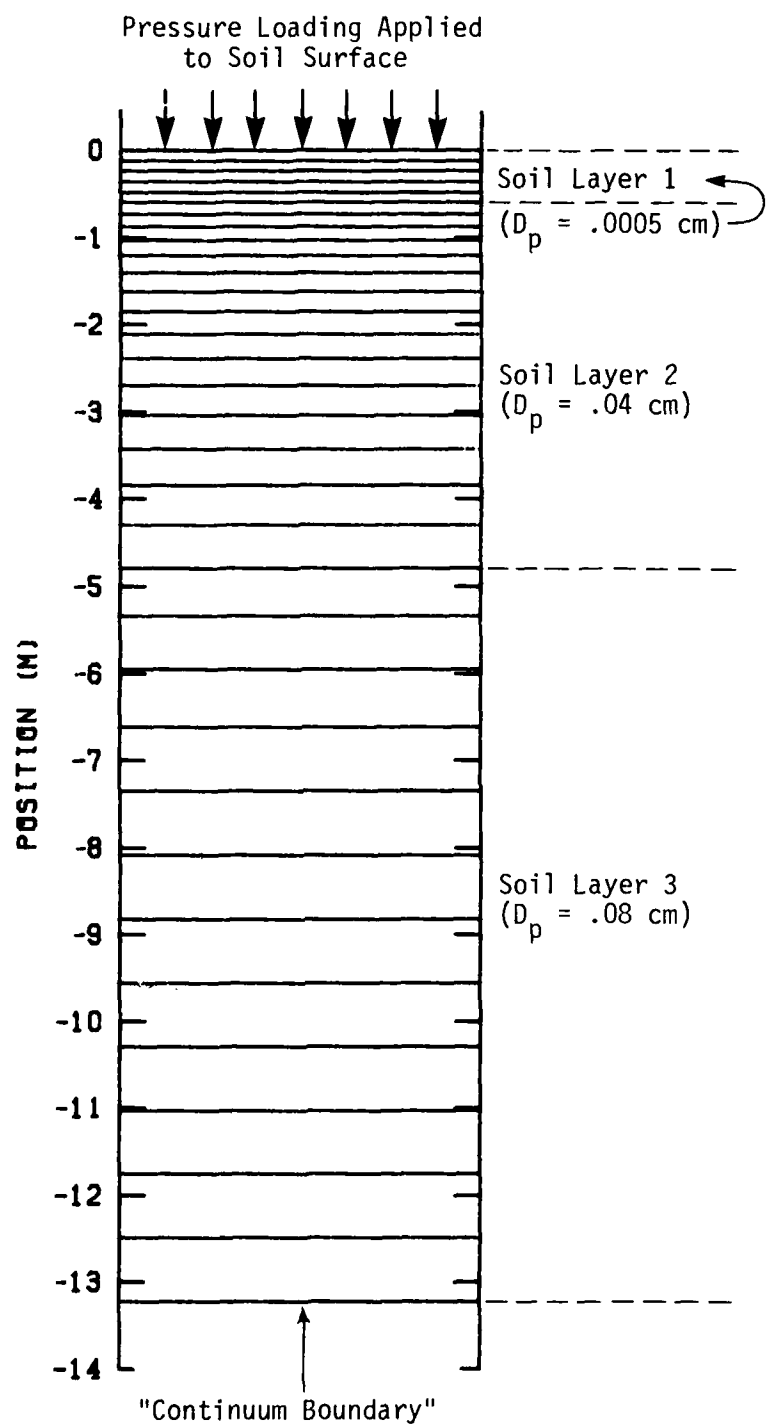


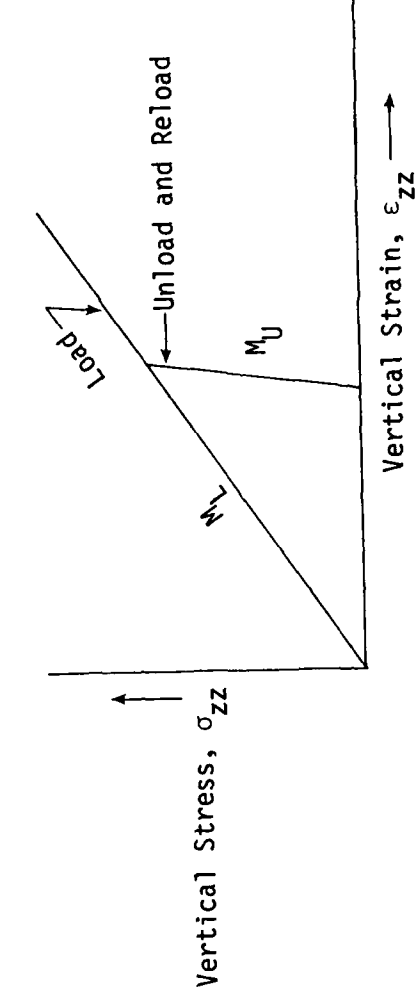
Figure 4.8. Grid Used for DICE 1-D MISERS BLUFF II-2 Calculation, Case 5.

Table 4.1. MISERS BLUFF II-2 Material Properties.

| Depth (m) | Region | Wet Density ρ_o (gm/cm ³) | Grain Density ρ_g (gm/cm ³) | Porosity ν_a (%) | Seismic Constrained Modulus | | Wave Speeds C_L (m/s) | Characteristic Particle Size D_p (cm) | Permeability k (Darcy) |
|--------------|--------|--|--|----------------------------|-----------------------------|-----------------|-------------------------------|---|------------------------------|
| | | | | | M_L (kbar) | M_U (kbar) | | | |
| 0 | 1 | 1.32 | 2.36 | 44.0 | 0.2 | 33.3 | 123 | 1590 | .0005 |
| 0.60 | 2 | 1.75 | 2.60 | 32.6 | 1.2 | 27.8 | 262 | 1261 | .04 |
| 4.79 | 3 | 2.06 | 2.08 | 1.0 | 0.3** | 90.0 | 197 | 2090 | .08 |
| 13.22 | | | | | | | | | .0032 |

*1 Darcy = 9.87×10^{-9} cm²

**Quadratic loading above $\sigma = 6$ bars.



forces between the air and soil particles (i.e., drag) are increased with a decrease in permeability, so that the relative velocities will be smaller.

Case 5 includes the effects of a uniform gravitational field ($g = 980 \text{ cm/s}^2$). This requires an initial lithostatic soil pressure at depth to support the weight of the total amount of soil above that depth. The initial pore-air pressure was taken to be 1 atm, uniform in each layer.

Figure 4.9 to 4.13 shows the pressure and velocity distributions for soil and air from $t = .047 \text{ s}$ after detonation to $t = .600 \text{ s}$. The first airblast peak (6.5 bars overpressure) in the loading function occurs at $t = .043 \text{ s}$. Figure 4.9 shows that the relative velocity between the soil and air is essentially zero, due to the low permeability of the top soil layer. This contrasts with the large relative velocities seen in Case 1 (see Figure 3.9) shortly after the initial application of the surface pressure load. For Case 5, the soil is supporting virtually all of the overpressure load, except for a small amount supported by the air which has barely begun to permeate the soil near the surface.

Figure 4.10 shows that by $t = .101 \text{ s}$ all modeled soil layers have been affected by the airblast, which is at its third and final peak of the positive phase. The soil and air are moving downward together - almost 1 m/s at the surface and ~0.4 m/s at 13 m depth. At the interfaces between each soil layer (~0.6 m and ~4.8 m depths) discontinuities in the material properties cause propagation of reflected/transmitted pressure and velocity waves.

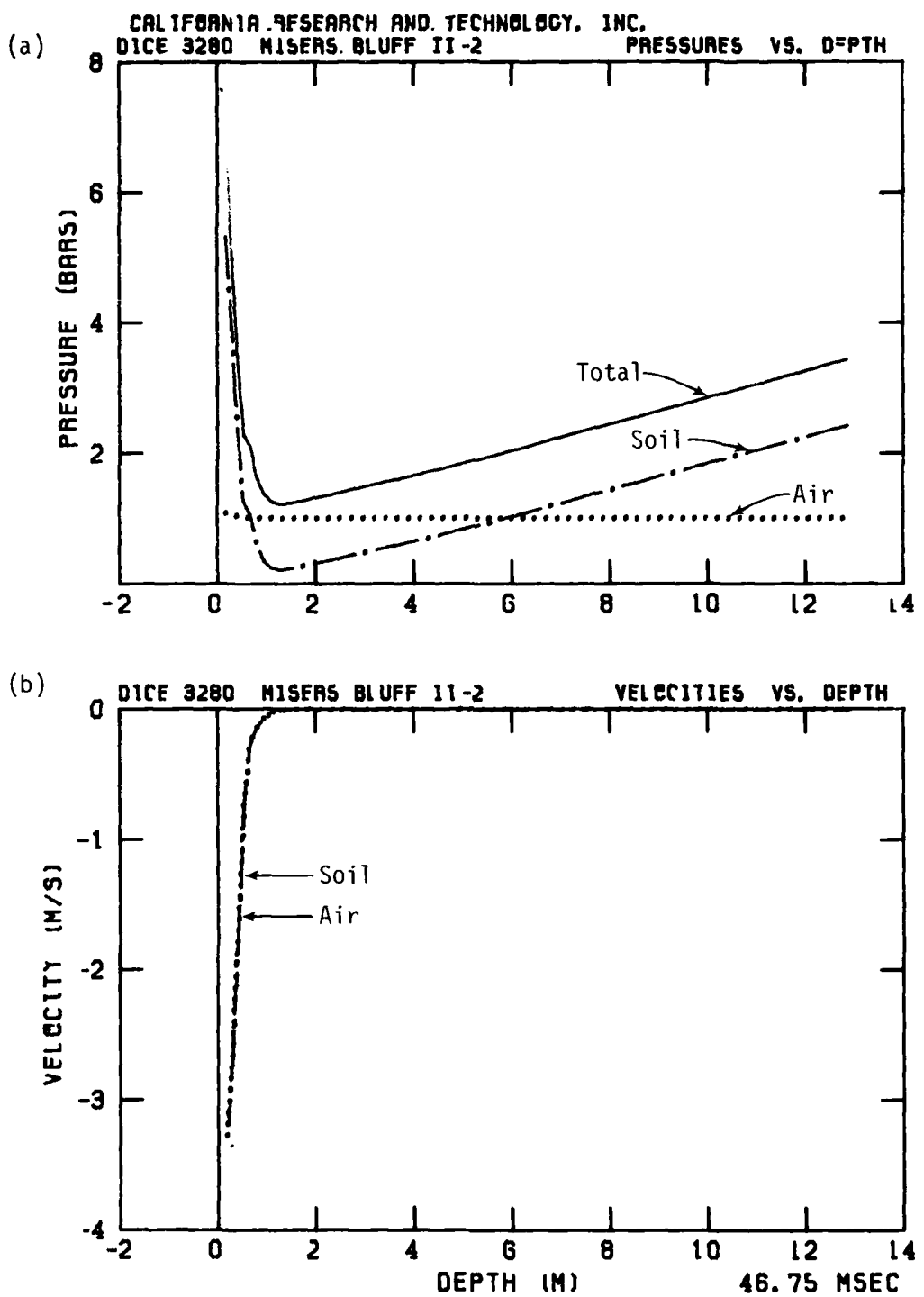


Figure 4.9. (a) Soil, Air and Total Stress Versus Depth, and
(b) Soil and Air Velocity Versus Depth at
 $t = .047$ Seconds for Case 5 (MBII-2).

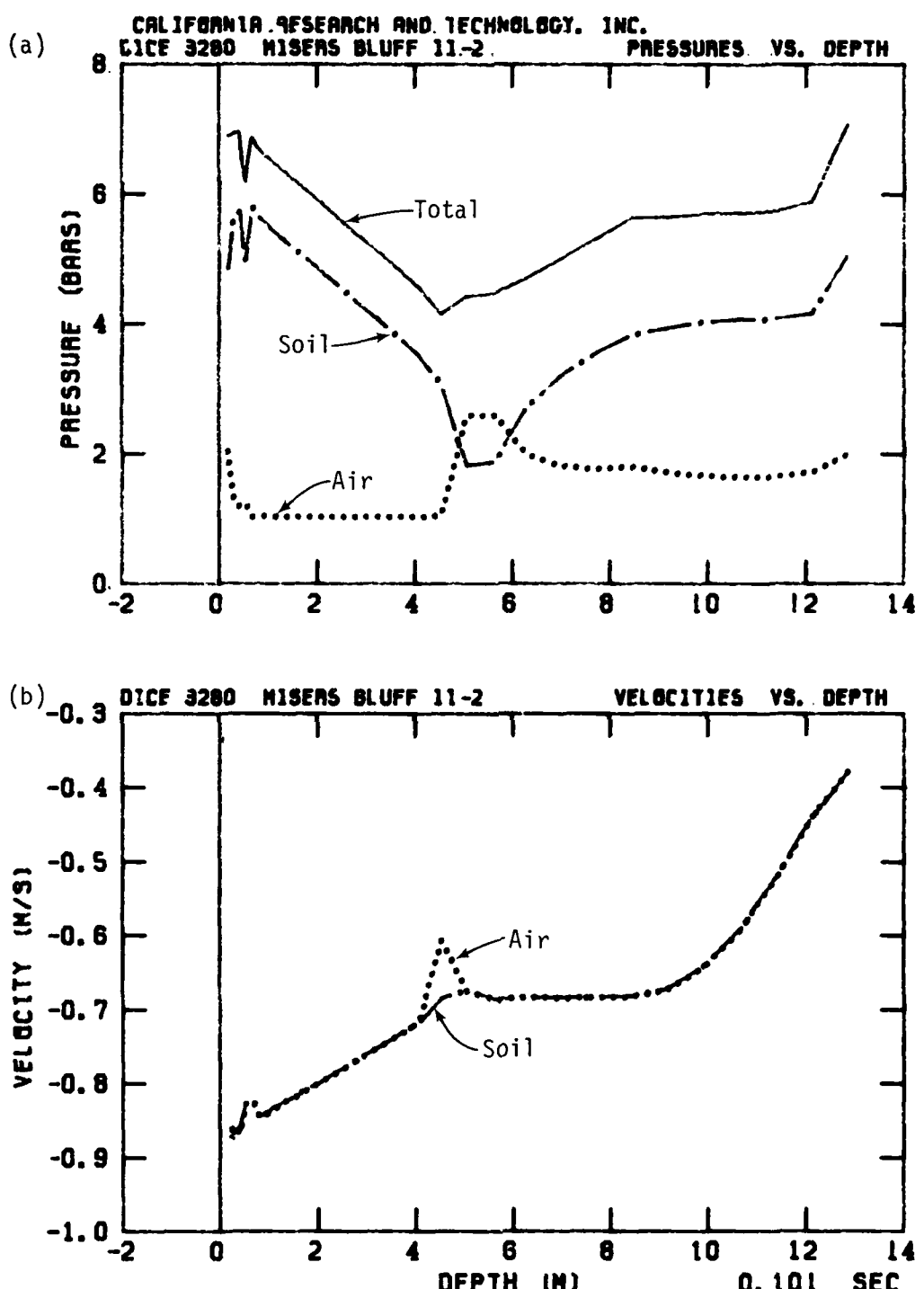


Figure 4.10. (a) Soil, Air and Total Stress Versus Depth, and
 (b) Soil and Air Velocity Versus Depth at
 $t = .101$ Seconds for Case 5 (MBII-2).

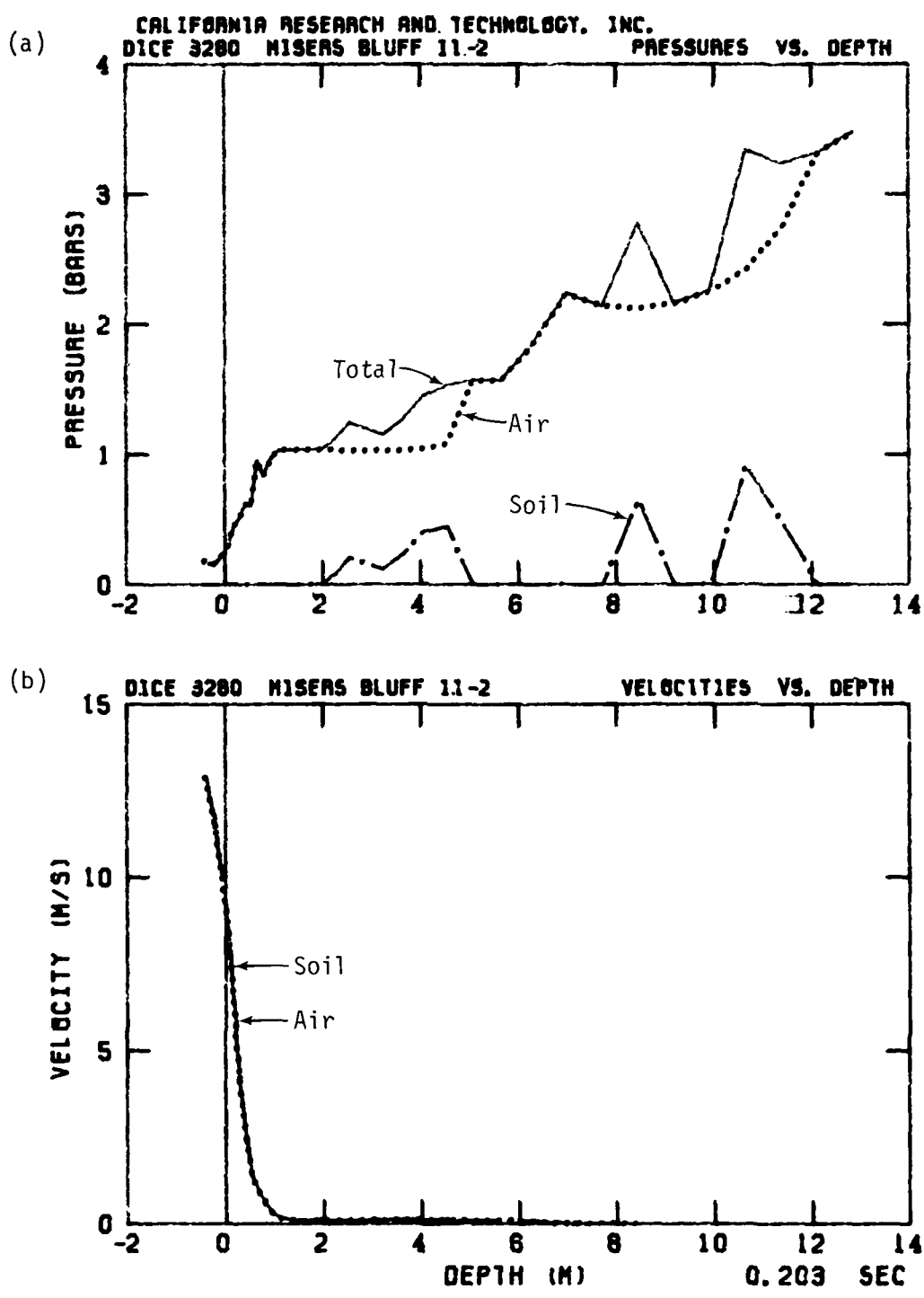


Figure 4.11. (a) Soil, Air and Total Stress Versus Depth, and
 (b) Soil and Air Velocity Versus Depth at
 $t = .203$ Seconds for Case 5 (MBII-2).

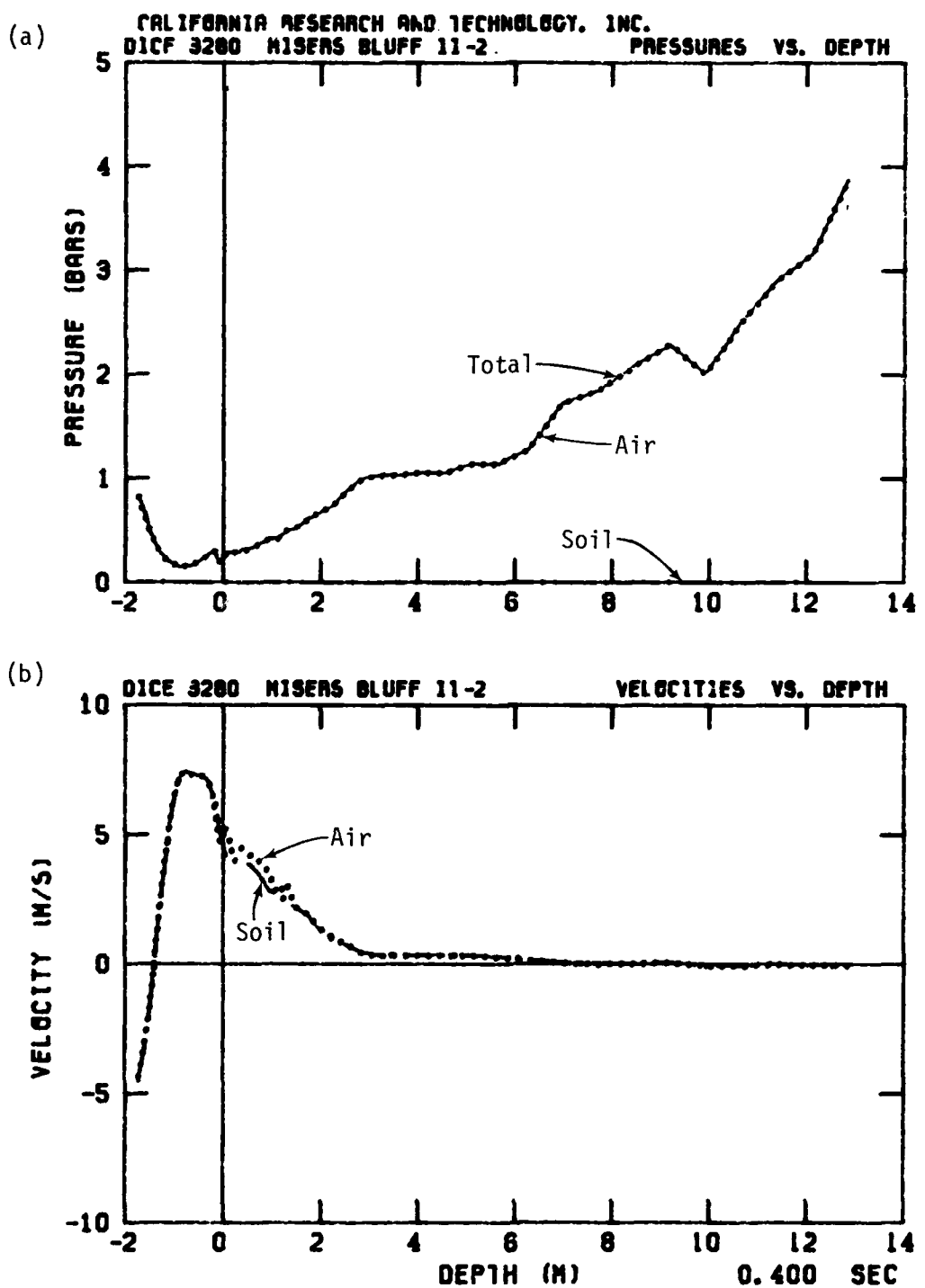


Figure 4.12. (a) Soil, Air and Total Stress Versus Depth, and
 (b) Soil and Air Velocity Versus Depth at
 $t = .400$ Seconds for Case 5 (MBII-2).

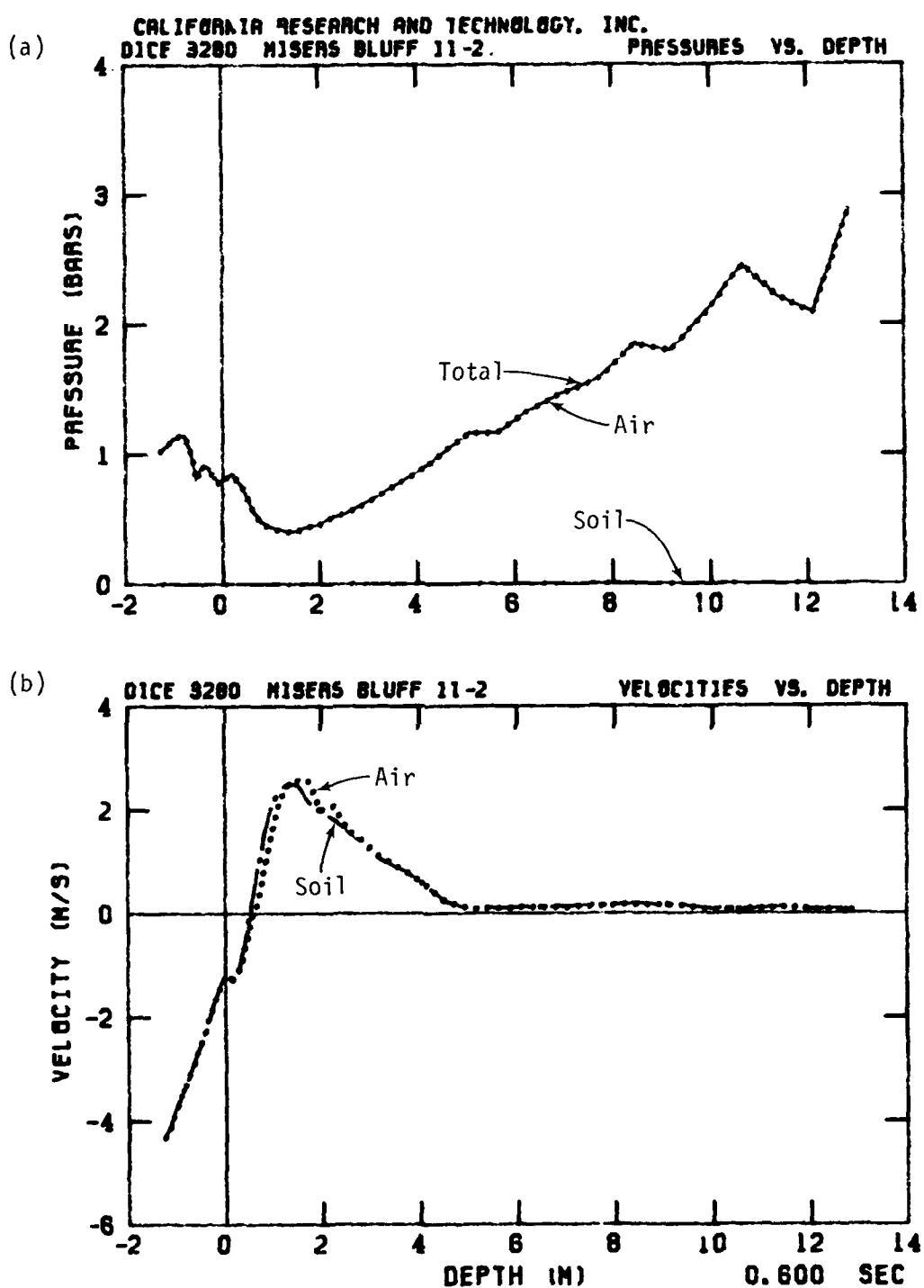


Figure 4.13. (a) Soil, Air and Total Stress Versus Depth, and
 (b) Soil and Air Velocity Versus Depth at
 $t = .600$ Seconds for Case 5 (MBII-2).

By $t = .203$ s the airblast is in its negative phase (-0.8 bar overpressure). Figure 4.11 shows that all of the soil in Layer 1 and part of Layer 2 (to ~2.0 m depth) is fluidized. The soil and air are moving upward above ~1 m depth in the soil with a peak velocity of over 12 m/s at the surface; the surface has risen ~0.5 m by this time.

For DICE Cases 1 to 4, fluidization at depth occurred as a result of enough air permeating the soil for the pore-air to support the positive (decaying) overpressure load applied at the surface. The same effect is achieved when a negative overpressure load is applied, even in the absence of a positive phase. The negative overpressure permits the pore-air to support the reduced pressure load. And, the pore-air expands to reach pressure equilibrium with the applied surface "underpressure".

By $t = .400$ s the surface overpressure loading has returned to zero. Figure 4.12 shows an air pressure minimum at ~1 m above the original ground surface. The resulting pressure gradient causes downward acceleration for the near-surface material. Peak downward velocities of almost 5 m/s exist at the surface, which has been raised almost 2 m above the original surface. Peak upward velocities of ~7 m/s are present at ~1.0 m above the original ground surface. The difference in velocities, although still small, between the soil and air in the 0 to 2 m depth region occurs in soil Layer 2, where the permeability is 10^3 times larger than in Layer 1.

The surface overpressure load remains at zero after $t = .400$ s. Figure 4.13 shows that by $t = .600$ s the pressure minimum has moved down to ~1.5 m depth, where the peak upward velocities are ~2 m/s for the soil and air. A peak downward

velocity of over 4 m/s is seen at the surface. All of soil Layer 2 is moving upward at this time; below the interface between Layer 2 and 3 the velocities are relatively small.

The use of an approximate airblast function based on data measured in MISERS BLUFF II-2 permits direct comparison with measured ground motion data. In Figures 4.14 and 4.15 the velocity and displacement time histories of the tracer point originally at 0.5 m depth are compared with the ground motion data measured with the four gauges originally at 0.5 m depth. Phenomenologically the agreement appears good. Up to $t \sim .150$ s the calculation and data show downward motion, though the calculated motion is not as large as measured. This could be due to the smaller peak pressures assumed in the loading function (see Figures 4.2 and 4.5). Both curves show a sustained upward velocity (in the negative overpressure phase) from $t \sim .150$ s to $t \sim .400$ s, with the calculated velocities and displacements being somewhat larger than measured. After this time the motion is again downward for both. Results from the Case 5 calculation indicate the primary role of pore-air phenomena in causing the sustained upward ground motion data measured in MISERS BLUFF II-2.

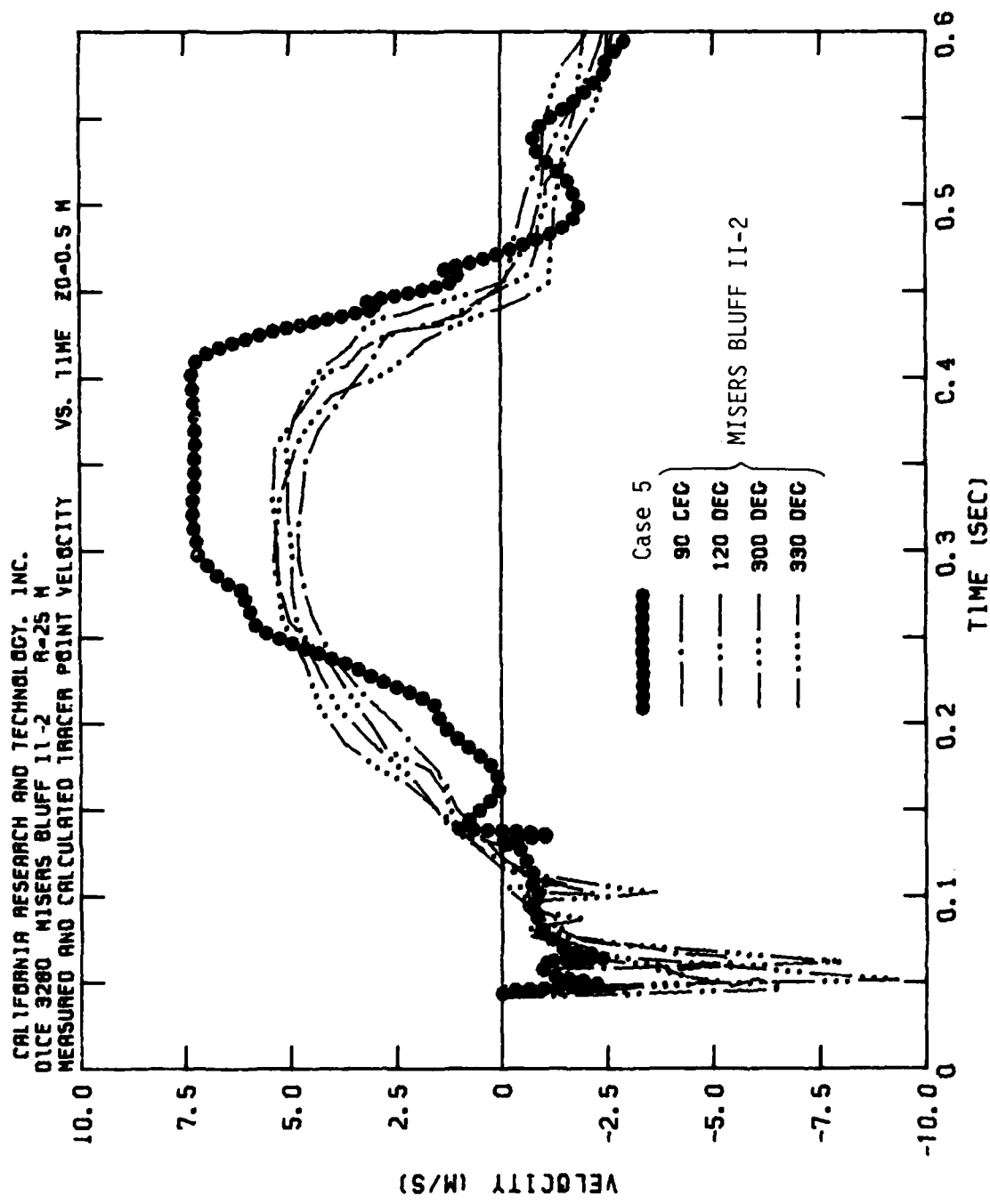


Figure 4.14. Vertical Velocity Time History Comparisons, Case 5 Versus MISERS BLUFF II-2 Experimental Data at 25 m Radius and 0.5 m Initial Depth.

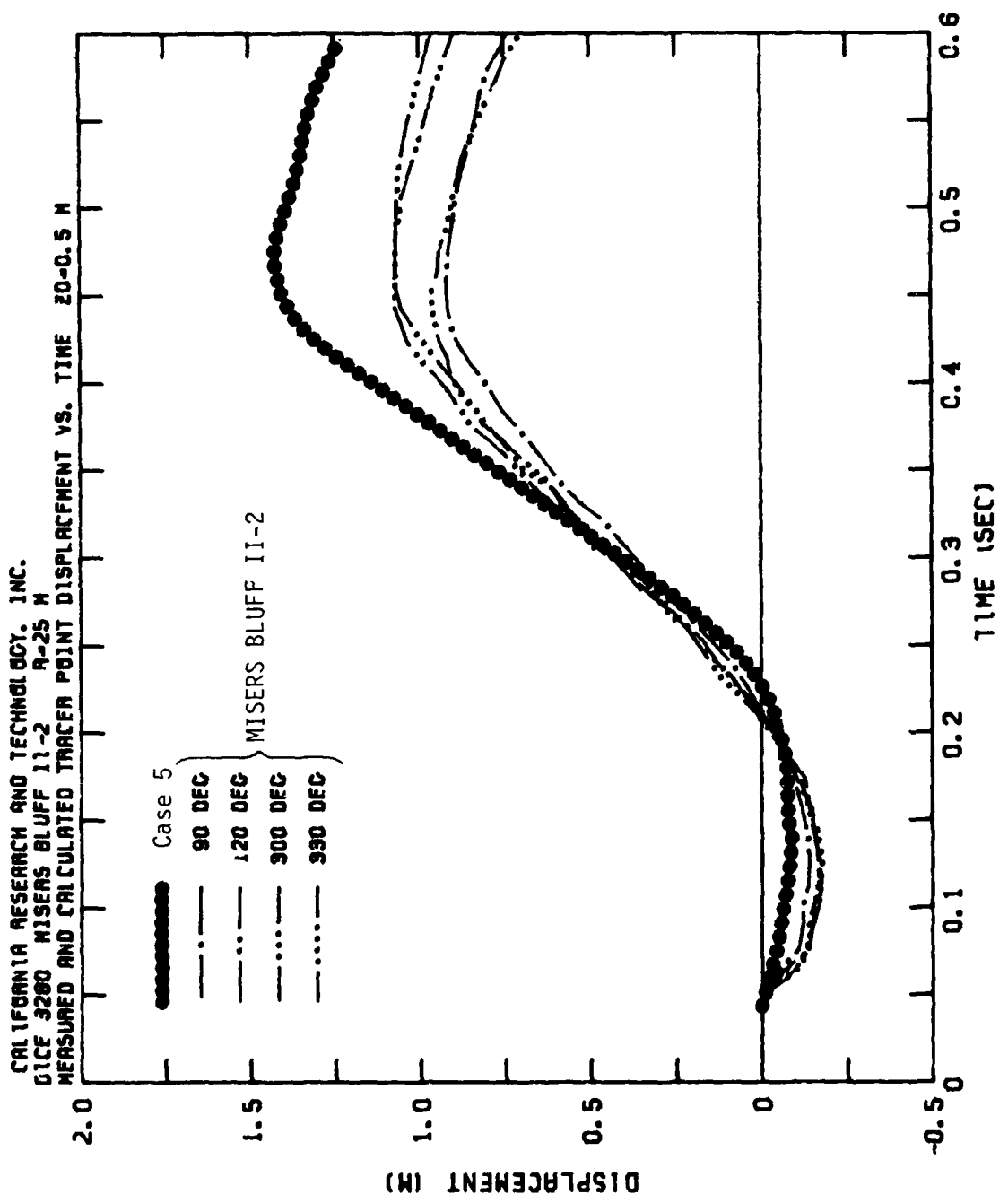


Figure 4.15. Vertical Displacement Time History Comparisons, Case 5 Versus MISERS BLUFF II-2 Experimental Data at 25 m Radius and 0.5 m Initial Depth.

REFERENCES

1. Murrell, D.W. and Stout, J.H., "MISERS BLUFF Series, Phase II, Ground Shock and Airblast Measurements, Data Report," POR 7011, U.S. Army Engineer Waterways Experiment Station, April 1980.
2. Stubbs, T., Kockly, J. and Sauer, F., "MIDDLE NORTH SERIES, PRE-MINE THROW IV, Air Blast and Ground Motion Project No. MT-301," POR 6833-1, Physics International Company, October 1976.
3. Zernow, L., Louie, N., Andersen, W.H. and Blatz, P.J., "An Experimental Study of the 'Reverse Percolation' Lofting Process in a Sand Medium," DNA 3210F, Shock Hydrodynamics, November 1973.
4. Rosenblatt, M., Eggum, G.E., Hassig, P.J. and Schlamp, R.J., "DICE - A Two-Dimensional Implicit Code for Treating Compressible Flow in a Fluid-Particle Mixture," Unpublished Work, California Research & Technology, Inc.
5. Speicher, S.J. and Brode, H.L., "Airblast Overpressure Analytic Expression for Burst Height, Range and Time - Over an Ideal Surface," PSR Note 385, Pacific-Sierra Research Corp., November 1981.
6. Truesdell, C. and Toupin, R.A., "The Classical Field Theories," Handbuch der Physik, 3, Part 1, Springer-Verlag, 1960.
7. Carman, P.C., "Flow of Gases Through Porous Media," Butterworths Scientific Publications, 1956.
8. Brinkman, H.C., "Problems of Fluid Flow through Swarms of Particles and through Macromolecules in Solutions," Research, 2, p. 190, 1949.
9. Wallis, G.B., "One-dimensional Two-phase Flow," McGraw-Hill Book Co., 1969.
10. Courant, R. and Friedrichs, K.O., "Supersonic Flow and Shock Waves," John Wiley & Sons, 1948.

11. Jackson, A.E., "Calculational Profile and Material Property Recommendations for MISERS BLUFF II," U.S. Army Engineer Waterways Experiment Station, September 1979.
12. Jackson, A.E., Ballard, R.F. and Phillips, B.R., "Geotechnical Investigation for MISERS BLUFF II: Results from the Subsurface Exploration Programs," U.S. Army Engineer Waterways Experiment Station, April 1979.

DISTRIBUTION LIST

DEPARTMENT OF DEFENSE

Asst to the Secy of Def, Atomic Energy
ATTN: Executive Asst
ATTN: J. Rubell

Commander-in-Chief, Atlantic
ATTN: J7

Defense Intell Agency
ATTN: RTS-2A

Defense Nuclear Agency
ATTN: SPSS, G. Ullrich
4 cy ATTN: STTI-CA

Defense Tech Info Ctr
12 cy ATTN: DD

Field Command
DNA Det 1
Lawrence Livermore National Lab
ATTN: FC-1

Field Command
Defense Nuclear Agency
ATTN: FCPN
ATTN: FCTT, J. Lee
ATTN: FCTT
ATTN: FCTXE
ATTN: FCTT, W. Summa

Joint Chiefs of Staff
ATTN: GD10, J-5 Nuc & Chem Div

Joint Strat Tgt Planning Staff
ATTN: JPFFM
ATTN: JPSS
ATTN: JPTM
ATTN: JLKC
ATTN: JKLS
ATTN: JK, DNA Rep

Under Secy of Def for Rsch & Engrg
ATTN: Strat & Thtr Nuc Force, B. Stephan
2 cy ATTN: Strat & Space Sys (OS)

DEPARTMENT OF THE ARMY

BMD Advanced Technology Ctr
ATTN: ATC-T

BMD Systems Command
ATTN: BMDS-C-HLE, R. Webb

Chief of Engineers
ATTN: DAEN-MPE-T

Harry Diamond Labs
ATTN: DELHD-NW-P
ATTN: DELHD-TA-L

US Army Ballistic Rsch Labs
ATTN: DRDAR-BLT, J. Keefer
ATTN: DRDAR-BLA-S

US Army Cold Region Res Engrg Lab
ATTN: Library

DEPARTMENT OF THE ARMY (Continued)

US Army Engineer Ctr & Ft Belvoir
ATTN: Tech Library

US Army Engrg Div, Huntsville
ATTN: HNDEN-FO

US Army Engrg Waterways Exper Station
ATTN: WESSD, J. Jackson
ATTN: J. Zelasko
ATTN: Library
ATTN: WESSA, W. Flathau
ATTN: WESSS, J. Ballard
ATTN: WESSE, D. Day

US Army Material & Mechanics Rsch Ctr
ATTN: Tech Library

US Army Materiel Dev & Readiness Cmd
ATTN: DRXAM-TL

US Army Nuc & Chem Agency
ATTN: Library
ATTN: MONA-WE
ATTN: MONA-WE, J. Uecke

DEPARTMENT OF THE NAVY

Naval Civil Engrg Lab
ATTN: Code L53, J. Forrest

Naval Postgraduate School
ATTN: Code 1424 Library
ATTN: G. Lindsay

Naval Rsch Lab
ATTN: Code 2627, Tech Lib
ATTN: Code 4040, J. Boris
ATTN: Code 4040, D. Book

Naval Surface Weapons Ctr
ATTN: Code F31
ATTN: Code X211, Tech Lib
ATTN: Code R44, H. Glaz

Naval Surface Weapons Center
ATTN: Tech Library & Info Svcs Br

DEPARTMENT OF THE AIR FORCE

Air Force Institute of Technology
ATTN: Library
ATTN: ENA

Air Force Systems Command
ATTN: DLWM

Air Force Weapons Lab
ATTN: NTE, M. Plamondon
ATTN: NTES-A
ATTN: SUL
ATTN: NTED
ATTN: NTES-C
ATTN: NTED-S
ATTN: NTES-R
ATTN: NTEO
ATTN: DEY

DEPARTMENT OF THE AIR FORCE (Continued)

Air University Library
ATTN: AUL-LSE

Assistant Chief of Staff, Intel
ATTN: IN

Assistant Chief of Staff
Studies & Analysis
2 cy ATTN: AF/SAMI, Tech Info Div

Asst Secy of the AF
Rsch, Dev & Logistics
ATTN: SAFALR/Dep for Strat & Space Sys

Ballistic Missile Office/DAA
ATTN: EN
ATTN: ENSN
ATTN: EN, C. Case
ATTN: ENSN, A. Schenker
ATTN: ENSN, E. Furbee

Deputy Chief of Staff
Rsch, Dev & Acq
ATTN: AFRD-M, Spec Asst for MX
ATTN: AFRDQI

Strategic Air Command
ATTN: DEPM
ATTN: NRI/STINFO Library
ATTN: XPF5
ATTN: XPQ

OTHER GOVERNMENT AGENCY

Central Intelligence Agency
ATTN: OSWR/NED

DEPARTMENT OF ENERGY CONTRACTORS

University of California
Lawrence Livermore National Lab
ATTN: D. Glenn

Los Alamos National Laboratory
ATTN: M. Sandfor
ATTN: C. Keller

Sandia National Laboratories
ATTN: Org 7112, A. Chabai
ATTN: Div 1111, J. Reed
ATTN: J. Bannister

DEPARTMENT OF DEFENSE CONTRACTORS

Acurex Corp
ATTN: C. Wolf

Aerospace Corp
ATTN: H. Mirels
ATTN: Library Acq M1/199

Agbabian Associates
ATTN: M. Agbabian

Applied Rsch Associates, Inc
ATTN: N. Higgins
ATTN: J. Bratton

DEPARTMENT OF DEFENSE CONTRACTORS (Continued)

Applied Rsch Associates, Inc
ATTN: R. Frank

Applied Rsch Associates, Inc
ATTN: D. Piepenburg

Applied Rsch Associates, Inc
ATTN: J. Shinn

Applied Theory, Inc
2 cy ATTN: J. Trulio

ARTEC Associates, Inc
ATTN: S. Gill

Astron Rsch & Engrg
ATTN: J. Huntington

Boeing Co
ATTN: Aerospace Library
ATTN: S. Strack

California Rsch & Technology, Inc
ATTN: Library
ATTN: K. Kreyenhagen
2 cy ATTN: M. Rosenblatt
2 cy ATTN: P. Hassig
2 cy ATTN: D. Orphal

California Rsch & Tech, Inc
ATTN: F. Sauer

Carpenter Rsch Corp
ATTN: H. Carpenter

University of Denver
ATTN: Sec Officer for J. Wisotski

Dynamics Technology, Inc
ATTN: D. Hove

Electro-Mech Systems, Inc
ATTN: R. Shunk

H&H Consultants, Inc
ATTN: W. Hall
ATTN: J. Haltiwanger

H-Tech Labs, Inc
ATTN: B. Hartenbaum

IIT Research Institute
ATTN: Document Library

Kaman AviDyne
ATTN: R. Ruetenik

Kaman Sciences Corp
ATTN: E. Conrad

Kaman Tempo
ATTN: DASIAC

Kaman Tempo
ATTN: DASIAC

Martin Marietta Denver Aerospace
ATTN: D-6074, G. Freyer

DEPARTMENT OF DEFENSE CONTRACTORS (Continued)

Kendan Associates
ATTN: R. Dannenberg
ATTN: J. Owren

Maxwell Laboratories, Inc
ATTN: J. Murphy

McDonnell Douglas Corp
ATTN: H. Herdman
ATTN: D. Dean
ATTN: R. Halprin

Merritt CASES, Inc
ATTN: Library

Mission Rsch Corp
ATTN: C. Longmire

University of New Mexico
ATTN: G. Leigh
ATTN: J. Kovarna
ATTN: P. Lodde
2 cy ATTN: D. Calhoun

Pacific-Sierra Rsch Corp
ATTN: D. Gormley

Pacific-Sierra Rsch Corp
ATTN: H. Brode, Chairman SAGE

Pacifica Technology
ATTN: Tech Library
ATTN: R. Allen

Patel Enterprises, Inc
ATTN: M. Patel

Physical Rsch, Inc
ATTN: R. Deliberis

Physics International Co
ATTN: Tech Library
ATTN: R. Collins

R&D Associates
ATTN: C. Knowles
ATTN: J. Lewis
ATTN: Tech Info Ctr
ATTN: A. Kuhl
ATTN: D. Simons
ATTN: P. Haas

S-CUBED
ATTN: C. Dismukes
ATTN: K. Pyatt
ATTN: Library
ATTN: J. Barthel

DEPARTMENT OF DEFENSE CONTRACTORS (Continued)

Rand Corp
ATTN: B. Bennett

Rand Corp
ATTN: P. Davis

S-CUBED
ATTN: C. Needham

Science & Engng Associates, Inc
ATTN: H. Linnerud

Science & Engng Associates, Inc
ATTN: B. Chambers III

Science Applications, Inc
ATTN: W. Layson
ATTN: J. Cockayne
ATTN: G. Binninger

Science Applications, Inc
ATTN: H. Wilson
ATTN: Tech Library
ATTN: R. Schlaug

SRI International
ATTN: J. Colton
ATTN: G. Abrahamson
ATTN: Library

Teledyne Brown Engineering
ATTN: F. Leopard
ATTN: B. Hartway
ATTN: D. Ormond

Terra Tek, Inc
ATTN: Library
ATTN: J. Schatz

TRW Electronics & Defense Sector
ATTN: N. Lipner
ATTN: Tech Info Ctr

TRW Electronics & Defense Sector
ATTN: G. Hulcher
ATTN: E. Wong
ATTN: P. Dai

Weidlinger Associates, Consulting Engrg
ATTN: T. Deevy

Weidlinger Associates, Consulting Engrg
ATTN: I. Sandler

Weidlinger Associates, Consulting Engrg
ATTN: J. Isenberg

R&D Associates
ATTN: G. Ganong

END

FILMED

8-85

DTIC